MAGNETIC IMAGING OF PYROLYSIS FEEDSTOCKS TO MODEL OLEFIN PRODUCT YIELDS

P.S. Virk

Department of Chemical Engineering
M.I.T., Cambridge, MA 02139

Abstract

A system for the <u>M</u>agnetic <u>I</u>maging of <u>P</u>yrolysis <u>F</u>eedstocks, acronym MIPF (pronounced with P silent) has been devised comprising three facets. First, sample preparation incorporates internal standards into the feedstock oils, to enable precise analysis of the NMR experiments. Second, NMR experiments are performed to provide quantitative C13 and H1 spectra, with spectral features elaborated by 1-D and 2-D procedures such as DEPT, COSY and HETCOR. Third, data analysis employs (1) an Integral Regions train, which provides coarse but complete information about all the carbon and hydrogen atoms in a feedstock, particularly the aromatic C and H atoms, and (2) a Canonical Groups train, which provides high-level information about chemical moieties, but detects only ~1/3 of all the atoms in the feedstock, particularly those in n- and methyl-alkane chains. An example illustrates how the MIPF parameters of an AGO feedstock might presage its performance in an ethylene plant.

Introduction

The present work derives from the need to engineer and predict the performance of modern pyrolysis coils that must crack diverse feedstocks at ever increasing temperatures, reaction severities and product selectivities. NMR imaging adds a unique dimension to olefin feedstock characterization because of its intimate relation to molecular topology and carbon atom hybridization. The most valuable olefins, ethylene, propylene, and butadiene, arise from operation of the free radical pathways prevalent during pyrolysis upon specific chemical moieties contained within the feedstock, respectively, normal-alkane chains, n-alkyl chain termini and methyl-alkyl units, and interior methylene chains. Individual sp3-hybridized carbon atoms within each of these moieties can be detected by NMR, to anticipate the corresponding olefin yields available from pyrolysis.

Of the voluminous literature on NMR applied to hydrocarbon mixtures, the present work has most been influenced by the classic papers of Knight (1967), Shoolery and Budde (1976) and Deutsche, Jancke and Zeigan (1976), specific articles by Ladner and Snape ((1978), Gillet et al (1981), Netzel et al (1981), and especially Cookson and Smith (1985, 1987), and the texts by Stothers (1972), Breitmaier and Voelter (1987) and Croasmun and Carlson (1994). In an earlier work (Virk 1999), akin to the present, NMR was applied to enhance conventional and mass spectrometric characterizations of FCC feedstocks.

MIPF System

Samples are prepared with gravimetric incorporation of internal standards into the feedstock oils, here AGOs and HCRs, to enable precise analysis and interpretation of the NMR experiments. Three internal standards are used, namely, deuterochloroform CDCl3, as oil solvent and spectrometer lock; dioxane, C4H8O2, abbr DIOX, to assist in spectral integrations; and tetramethylsilane, Si(CH3)4, abbr TMS, as a spectral frequency reference. The primary NMR experiments performed provide quantitative C13 and H1 spectra, the spectral regions and individual resonances observed therein being identified and interpreted by additional 1-D and 2-D procedures that include DEPT, COSY, and HETCOR. Spectral data are analysed in two trains, according to either their integral regions, abbr IR, or their

canonical groups, abbr CG. In the IR train, the observed spectra are parsed into more or less coarse regions, each comprizing chemically similar sorts of atoms. The IR train accounts for 100% of feedstock atoms and provides useful overall parameters, such as the percent of feedstock atoms, either carbon or hydrogen, that are aromatic, as well as more detailed regional data, and thence hydrogen atom counts, and thermochemical information. In the CG train, certain groups of spectral peaks that arise from atoms belonging to particular molecular moieties are recognized, particularly those in linear n-alkane chains and in 2-, 3-, 4-, 5-, and interior-methyl alkane branched chains. The CG train thus provides high-level quantitative information about n-alkane content and chain length, as well as the contents of a variety of methyl-alkane moieties; however the sum of identified species is but a fraction of the total, typically amounting to ~ 40% of feedstock atoms. Both IR and CG trains are combined to form a set of NMR groups that characterize the feedstock.

NMR Experiments

13-C. Figure 1 shows the 13-C NMR spectrum of an AGO feedstock called A1 in Table 1 (infra). The position of a peak on the x-axis, its resonance frequency or chemical shift, c, in units of ppm relative to TMS, is indicative of C atom type, while peak height on the y-axis, its absorption intensity, i, with arbitrary units, is roughly proportional to the abundance of such C atoms in the sample. Precise carbon atom amounts are obtained from peak integration, these integrals being the five continuously increasing stepped segments in the figure, their c-domains and magnitudes being noted below the abscissa.
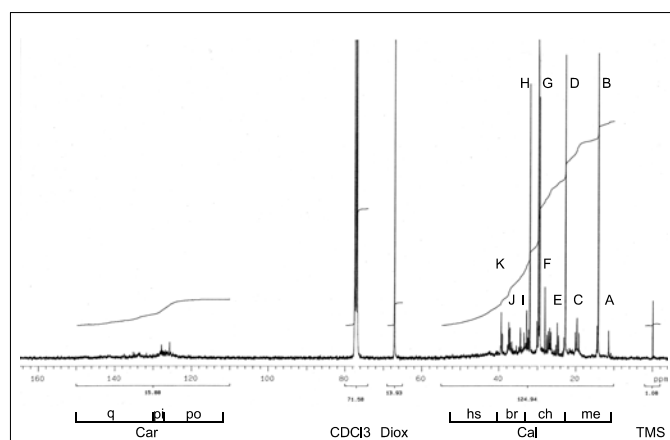

Figure 1. Annotated 13-C spectrum of an AGO feedstock.

The major spectral regions observed are:

Region	c (range)	C-atom type
TMS	0.0	methyl carbons in TMS
Cal	10 - 52	aliphatic carbons, sp3 hybridized
DIOX	~67	methylene carbons in DIOX
CDCl3	~78 triad	C in CDCl3 solvent
Car	112 - 150	aromatic carbons, sp2 hybridized

The wide separation between the regions of aliphatic and of aromatic carbons is noteworthy, allowing unambiguous delineation of these two broad categories; the integrals corresponding to these regions provide the carbon aromaticity Car = 11.5%. Further demarcations shown below the spectrum, called Cumulative Integral Regions, sort carbon atoms into categories with the following approximate chemical interpretations: Carqt is aromatic quaternary, which are inherently of two kinds, either fused ring junction or substituted, not distinguished here; Carpi and Carpo are both

aromatic protonated, with subtle distinctions between them; the sum Car(qt+pi+po) = Car.

Among aliphatic carbons, Calhs is aliphatic highly substituted, Calbr is aliphatic branched (single substitution, such as methyl), Calch is aliphatic chains, mainly CH2, and Calme is aliphatic methyls, all CH3. Many additional individual spectral regions can be distinguished in Figure 1, and these have been labelled beside their principal peaks as follows: Regions B, D, H, and G (two tall peaks at c ~30) respectively contain the carbon atoms C1, C2, C3, and (C4, C ≥5) in linear n-alkane chains. Region C contains mainly methyl groups, pendant on a variety of alkane, cyclo-alkane and aromatic structures. Regions E and F contain carbon atoms in C5- and C6-cyclo-alkane rings, as well as C2 in 2-methyl-alkanes. Regions A, I, J and K contain carbon atoms from branched (iso-) alkanes. Peaks of the n-alkane moiety in regions B, D, H, and G, called a Canonical Group, reveal the present AGO to possess an n-alkane chain content of 24.9 C atoms per 100 C atoms of feedstock, with an average chain length L = 6.9, that is, for every pair of terminal n-alkane atoms (C1, C2), there are 4.9 interior n-alkane atoms (C3, C4, C≥5).

1-H. Figure 2 shows the 1-H NMR spectrum of AGO feedstock A1. The x-axis is resonance frequency, or chemical shift, h, in units of ppm relative to TMS, indicative of hydrogen type, while the y-axis is absorption intensity, i, with arbitrary units, approximately proportional to the abundance of such hydrogen atoms in the sample. Accurate hydrogen amounts are obtained from integrals of peak intensities, seen as four continuous stepped lines in the figure, their h-domains and numerical magnitudes noted below the abscissa.
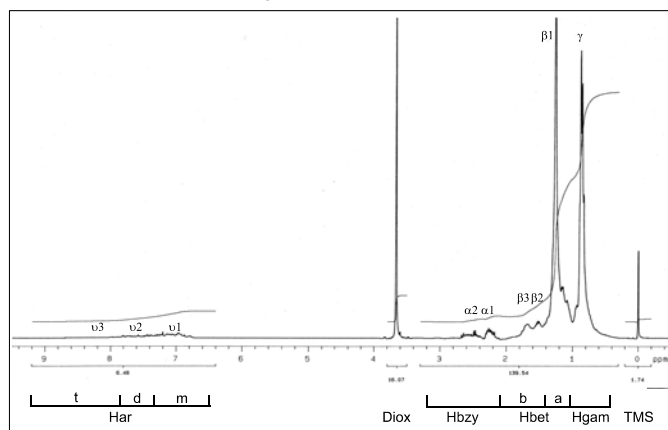

Figure 2. Annotated 1-H spectrum of an AGO feedstock.

The 1-H spectrum has the following regions:

Region	h (range)	H-atom type
TMS	0.0	H in methyls of TMS
Hgam, Hbet, Hbzy	0.4 - 3.2	Aliphatic H, attached to sp3 hybridized C atoms
DIOX	~3.65	H in methylenes of DIOX
Har	6.5 - 9.2	aromatic H, attached to sp2 hybridized ring C atoms

The wide separation between the regions of aliphatic and of aromatic hydrogens is noteworthy, permitting their unambiguous delineation, and providing the hydrogen aromaticity Har = 4.4%. The Cumulative Integral Regions, shown below the spectrum, have the following approximate chemical interpretations. The aromatic H region is subdivided into Hart, Hard, and Harm, with sum Har(t+d+m) = Har; of these, Harm contains H atoms from all aromatic rings; Hard contains H atoms from ≥ 2- but not from 1-ring aromatics; and Hart contains H atoms from ≥ 3- but not from ≤ 2-ring

aromatics. Next, Hbzy are benzylic H atoms, attached to aliphatic C atoms bonded to aromatic rings; Hbzy thus reflects the degree of aromatic ring substitution. Of the two broad benzylic peaks in the spectrum, α1 is mainly H atoms on methyls pendant on mono-aromatic rings, while α2 contains a host of other benzylic hydrogens. Hbet are H atoms attached to aliphatic C atoms bonded to other aliphatic C atoms; region Hbeta, with huge peak β1, is primarily H atoms in the methylene CH2 units of alkyl chains, while Hbetb includes H atoms on CH (methine) and CH2 (methylene), the peaks β2, β3 including H atoms on alicyclic rings. Hgam, with large twin peaks γ, are H atoms in aliphatic methyls CH3.

2-D HETCOR. Figure 3 is a 2-dimensional contour plot showing the islands in an H-C atom correlation spectrum of AGO feedstock A1.
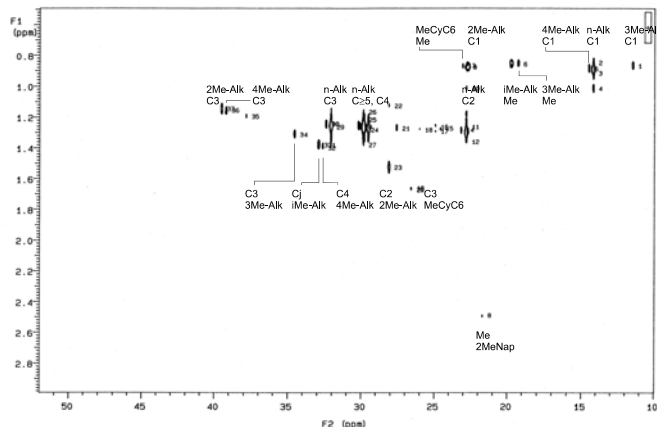

Figure 3. Annotated HETCOR spectrum of an AGO feedstock.

The HETCOR experiment, described by Gray (1994), is the equivalent of recording full 1-H spectra, such as shown in Figure 2, at each of a myriad slices of a 13-C spectrum, such as shown in Figure 1. A correlation island at chemical shift coordinates [c, h] represents a carbon of shift c connected to a hydrogen of shift h, with island cross-section (actually, its peak height and volume) crudely related to the abundance of the correlated atoms in the feedstock. In Figure 3, with abscissa (F2 axis) c and ordinate (F1 axis) h, the large lens-shaped island #3 at coordinates [c, h] = [14.2, 0.89] arises from the H and C atoms in the terminal methyl group of an n-alkane chain and is labeled n-Alk C1. This particular island has peak height p = 232 units on a scale where the spectral noise level is p ~ 1; the 37 islands visible on the figure have peak heights 283 > p > 4, with all signals well above noise. Islands that have been chemically identified are labelled in four rows, top to bottom, representing methyl CH3, methylene CH2, methine CH, and benzylic methyl CH3 carbons. Identified islands belong to the following Canonical Groups: n-alkane (C1, C2, C3, C4, C≥5), 2-methyl alkane (C1, C2, C3), 3-methyl alkane (C1, Me, C3), 4-methyl alkane (C1, C3, C4), interior-methyl alkane (Me, Cj(unction)), methyl-cycloalkane (Me, C3(ring)), and 2-methyl naphthalene (Me).

Results

Both conventional and MIPF characterizations were acquired for six pyrolysis feedstocks, three AGOs and three HCRs, with results for two AGOs A1 and A2 and an HCR R1 shown in Table 1.

Table 1. Conventional and MIPF Characterizations.

Entry		A1	A2			R1
CONVENTIONAL DATA						
SG	15.6C	0.838	0.843			0.835
H	Wt%	13.55	13.27			14.82
C	Wt%	86.34	86.51			85.18
S	Wt%	0.12	0.20			0.00
Helem	H/100 C	187	183			207
MIPF DATA						
IR Train C13						
diox/oil	Gravim	0.102	0.096	±	0.001	0.096
diox/oil	Spectral	0.099	0.106	±	0.005	0.094
Car	C/100 C	11.5	15.2	±	0.3	0.0
CIRs						
Calme		17.1	18.9	±	0.6	12.8
Calch		44.3	44.6	±	0.6	67.0
Calbr		18.5	16.5	±	0.3	16.8
Calhs		8.7	4.8	±	0.7	3.4
Carpo		4.6	4.4	±	0.7	0.0
Carpi		2.0	3.0	±	0.0	0.0
Carqt		4.9	7.8	±	0.5	0.0
Sum		100.0	100.0			100.0
IR Train H1						
diox/oil	gravimetric	0.109	0.105	±	0.001	0.093
diox/oil	Spectral	0.112	0.106	±	0.006	0.090
Har	H/100 H	4.4	5.6	±	0.3	0.1
CIRs						
Hgam		35.4	33.7	±	1.2	21.9
Hbeta		50.7	47.5	±	0.4	70.8
Hbetb		7.0	8.6	±	1.3	6.7
Hbzy		2.5	4.7	±	0.6	0.5
Harm		2.5	3.2	±	0.0	0.1
Hard		1.4	1.7	±	0.1	0.0
Hart		0.5	0.7	±	0.1	0.0
Sum		100.0	100.0			100.0
CG Train C13						
Lna	Atoms	6.9	5.9	±	0.0	9.7
Groups	C/100 C					
Can	n-Alkane	24.9	21.8	±	1.5	50.3
Cma	Me-Alkane	12.3	13.6	±	0.7	14.6
Ccs	Cyc+Sub	51.3	49.5	±	2.5	35.1
Car	Aromatic	11.5	15.2	±	0.3	0.0
Sum		100.0	100.0			100.0

Conventional properties included specific gravity and elemental assays of H, C, and S, from which H elem, H atoms/100 C atoms, has been calculated.

MIPF data include results from the IR and CG trains; for samples run in duplicate, average values and an estimate of their experimental uncertainty are quoted. Among IR train C13 data, the two rows labelled diox/oil are the ratios of carbon atoms in the dioxane internal standard to those in the oil; the gravimetric row was calculated from sample preparation and elemental assays while the spectral row was independently derived from the regional integrals of the experimental spectra. Agreement between these internal standard ratios is a stringent test of C13 NMR data fidelity. The next row, Car, and then the next seven rows, called CIRs for Cumulative Integral Regions, provide a breakdown of feedstock carbon atom types, as percentages. CIRs are so named because each is the accumulation of Detailed Integral Regions, DIRs, which represent the finest parsing of spectral integrals; CIRs were earlier delineated in Figure 1 and their chemical significance pointed out. Data from the IR train H1 are analogous to those from the IR train C13, with two diox/oil rows, gravimetric and spectral, followed by Har and then seven CIRs, that were earlier considered in the 1-H NMR spectrum in Figure 2. Finally, the first row of the CG Train C13 data provides the average chain length of n-alkane moieties in the feedstock, Lna in C atoms. The second and third rows respectively provide the percentages of C atoms in n-alkane moieties Cna, and in methyl-alkane moieties Cma, the latter comprizing 2-, 3-, 4-, 5-, and interior-methyl substituted alkane moieties. These are used, along with Car from the IR train, shown again in the fifth row, to form a set of 4 NMR-derived Canonical Groups for each feedstock. In the fourth row, the group Ccs, comprising cyclic and highly substituted aliphatic C atoms, is a remnant (often large) obtained from Ccs = 100 - Cna - Cma - Car.

Dioxane/Oil Ratios. Ratios of dioxane to oil D/O,g from the gravimetric sample preparation procedure to those derived from spectral integration D/O,s for each of the C13 and H1 spectra recorded provided the average relation:

(E1) $D/O,s = (1.00 \pm 0.06)\, D/O,g.$

The present NMR integrals are thus accurate to within 6% absolute. Such noteworthy quantitative fidelity shows that modern NMR spectrometers can excite and detect diverse kinds of C and H atoms in the feedstock over wide frequency ranges on both sides of the C and H atoms in the dioxane internal standard.

MIPF Maps and Carbon Atom Groups. The NMR data in Table 1 provide three types of maps and two sets of carbon atom groups to characterize feedstocks in regard to their pyrolysis performance. These are, respectively, an aromaticity map, Car vs Har, a chain map, Cna vs Lna, and a branch map, Cna vs. Cma, as well as the sets of CIR and CG groups. For the present examples, the aromaticity map shows that while AGOs A1 and A2 differ appreciably in absolute terms, they possess similar ratios of Har/Car ≈ 0.37, implying similarity in their respective fractions of protonated, substituted, and ring junction aromatic carbons. The chain map reveals n-alkane chain contents and lengths to vary such that R1 >> A1 > A2 while the branch map provides ratios of methyl-alkanes/n-alkane in the order R1 << A1 < A2; both maps suggest that in producing ethylene, R1 should prove superior to both A1 and A2, and among the latter, A1 might be a bit better than A2.

MIPF-derived carbon atom groups for feedstocks A1 and R1 are depicted as pie charts in Figure 4. For each feedstock, the IR train pie has six slices [Calme, Calch, Calbr, Calhs, Carpr, Carqt], respectively denoting percentages of aliphatic methyl, chain, branch, highly-substituted carbons and aromatic protonated and quaternary carbons, while the CG train pie has four slices [Cna, Cma, Ccs, Car], respectively the percentages of n-alkane, methyl-alkane, alicyclic + highly substituted, and aromatic carbon atoms in the feedstock. The IR pie offers a complete but coarse sorting of the types of carbon atoms in a feedstock whereas the CG train offers refined information about carbons contained in n-and methyl alkane moieties but leaves a significant fraction of them, from 1/3 to 1/2, unassigned, in the remnant Ccs. A comparison between feedstocks A1 and R1 shows their respective IR and CG group pies to differ significantly, with R1

containing far more n-alkanes and virtually no aromaticity; on this basis, R1 should prove superior to A1 in producing more olefins and less pyrolysis fuel oil.
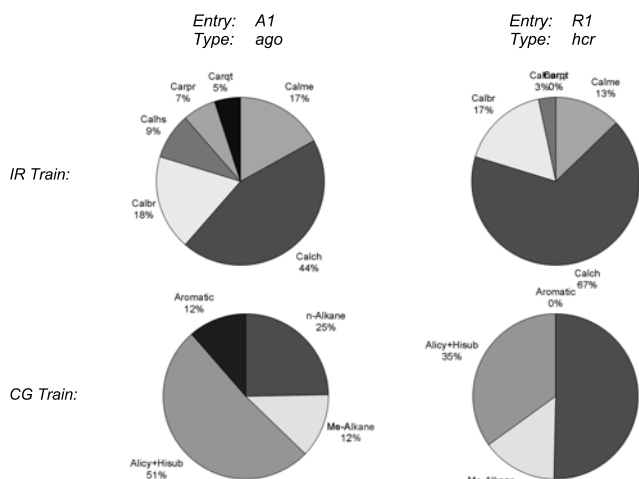

Figure 4. MIPF-derived carbon atom groups in two feedstocks.

Relation of MIPF to Pyrolysis Performance

Some examples are presented to illustrate how MIPF parameters might relate to pyrolysis product yields. Our slate of feedstocks, as well as three pure n-alkanes, namely decane, dodecane and hexadecane, were cracked using steam/hydrocarbon ratios ~ 1 and "kinetic severities" $K^* \sim 2$, as defined by Zdonik, Green and Hallee (1969). Reaction conditions and experimental apparatus were akin to those in an earlier work concerning pyrolysis of virgin and hydrogenated gas oils (Virk, Korosi and Woebcke 1979b).

Three fractions define overall pyrolysis yields, namely, in descending order of desirability, GAS, C4 and lighter; raw pyrolysis gasoline RPG, C5 to 400 F; and pyrolysis fuel oil PFO, >400 F. Figure 5, called a "yield fingerprint", is a Cartesian plot of GAS yield, wt%, versus IR Region 1, comprizing the sum of the first two CIRs (Calme + Calch), in C/100 C.
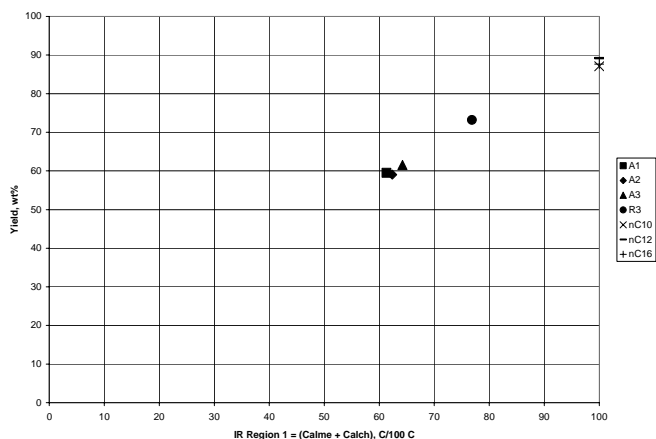

Figure 5. Yield fingerprint of GAS vs IR Region 1.

The GAS yields obtained from each feedstock are essentially equal to, perhaps a bit less than, the corresponding magnitudes of IR Region 1. Next, Figure 6 is a fingerprint of PFO yield, wt%, versus IR Region 3, which comprises the sum of CIRs 4 to 7, namely (Calhs + Car), in C/100 C.
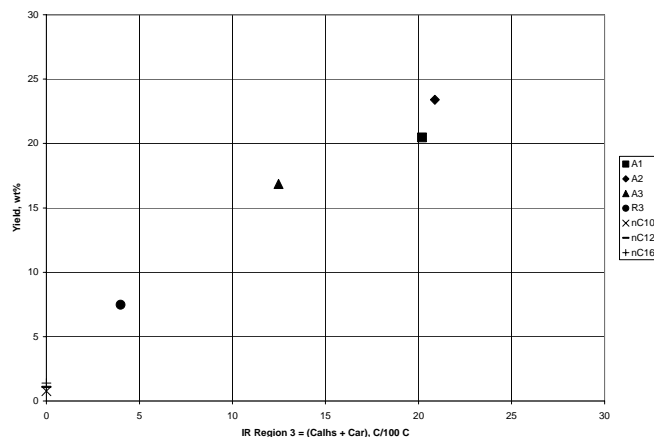

Figure 6. Yield fingerprint of PFO vs IR Region 3.

The PFO yields obtained from each feedstock are essentially equal to, perhaps a tad higher than, the corresponding magnitudes of IR Region 3. With GAS ≈ CIR(1+2) and PFO ≈ CIR(4+5+6+7), it follows from the requisite conservations that RPG ≈ CIR(3) = Calbr, called IR Region 2. It is mildly astonishing that the NMR-derived IR regions, that are simply sums of adjacent CIRs, should relate so directly to the respective amounts of the three overall pyrolysis products. This connection, which has not hitherto been reported, should be fun to explore and exploit.

Turning to individual products, Figure 7 presents a fingerprint for the major olefin, ethylene, using CG Cna, n-alkane chain content.
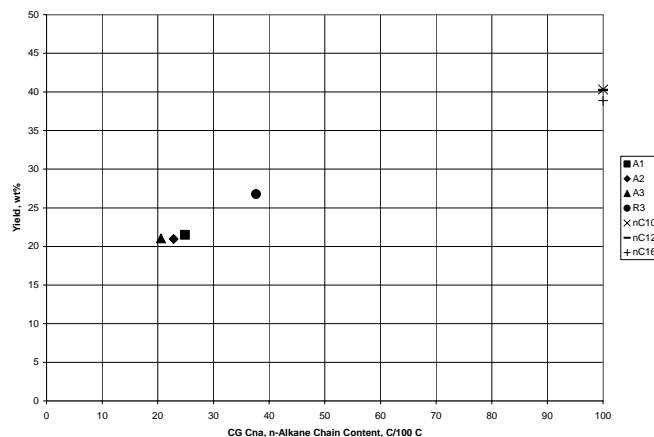

Figure 7. Yield fingerprint of Ethylene vs CG Cna, n-alkane chains.

Results from the pure n-alkanes, with Cna = 100, suggest that under the present pyrolysis conditions, n-alkane chains provide ethylene yield ≈ 0.4*Cna. Ethylene yields observed from the feedstocks range from (0.7 to 1.0)*Cna, and must therefore additionally arise from moieties other than n-alkanes. Finally, Figure 8 shows the fingerprint for a minor product, buta-1,3-diene, using CG Cna>2, n-alkane interior carbons, based on the notion of butadiene being a secondary product. The pure n-alkanes provide butadiene yield ≈ 0.1*Cna>2 while the AGO and HCR feedstocks have butadiene yields ≈ (0.2 to 0.3)*Cna>2, showing, as for ethylene, that butadiene must additionally arise from moieties other than n-alkane chain interiors.
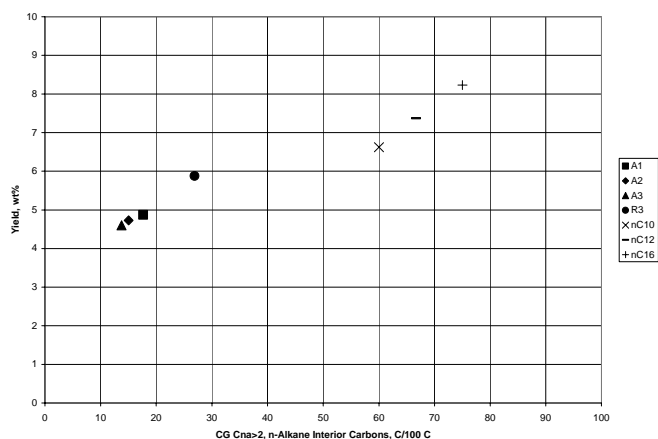
Figure 8. Yield fingerprint of Butadiene vs CG Cna>2, n-alkane interior carbons.

It is interesting that both ethylene and butadiene are abundant products of cyclohexane pyrolysis (Virk, Korosi and Woebcke 1979a), so that alicyclic moieties in the feedstocks might well provide additional sources for the ethylene and butadiene yields observed in excess of those expected from n-alkane chains.

Conclusions.
1. A MIPF system has been devised for quantitative NMR-assays of AGOs and HCRs according to a coarse but quantitative IR Train and a fine but fractional CG Train.

2. Annotated 13-C, 1-H, and 2-D HETCOR spectra of an AGO feedstock were presented to illustrate the system.

3. MIPF results for three each AGO and HCR feedstocks included:
Gravimetric vs spectral dioxane/oil ratios.
Carbon and Hydrogen aromaticities.
n-Alkane chain contents and chain lengths.
Characterization by IR and CG train carbon atom groups.

4. Overall and individual pyrolysis product yields at fixed cracking severity $K^* \sim 2$ were related to NMR-derived carbon atom groups as follows:
GAS (C4 and lighter) yields approximately equalled the unbranched, unsubstituted aliphatic carbons found from the IR train.
PFO (> 400F) yields roughly equalled the sum of (substituted + aromatic) carbons found from the IR train.
Ethylene yields varied with n-alkane chain content found from the CG train and butadiene yields varied with n-alkane internal carbons, also found from the CG train, but for both these products the observed yields exceeded those expected from n-alkane moieties alone.

References
(1) Knight, S.A.: Chem. Ind., 1920-1923 (1967).
(2) Shoolery, J.N.; Budde, W.L.: Anal. Chem., 48, 1458-1461 (1976).
(3) Deutsch, K.; Jancke, H.; Zeigan, D.: J. Prakt. Chem. Ind., 318, 177-184 (1976).
(4) Ladner, W.R.; Snape, C.E.: Fuel, 57, 658-662 (1978).
(5) Gillet, S.; Rubini, P.; Delpeuch, J.J; Escalier, J.C.; Valentin, P.: Fuel, 60, 221-225 (1981).
(6) Gillet, S.; Rubini, P.; Delpeuch, J.J; Escalier, J.C.; Valentin, P.: Fuel, 60, 226-230 (1981).
(7) Netzel, D.A.; McKay, D.R.; Heppner, R.A; Guffey, F.D.; Cooke, S.D.; Varie, D.L.; Linn, D.E.: Fuel, 60, 307-320 (1981).
(8) Cookson, D.J.; Smith, B.E.: Anal. Chem., 57, 864-871 (1985).
(9) Cookson, D.J.; Smith, B.E.: Energy & Fuels, 1, 111-120 (1987).
(10) Stothers, J.B.: "Carbon-13 NMR Spectroscopy", Academic Press, New York, NY 1972.
(11) Breitmaier, E.; Voelter W.: "Carbon-13 NMR Spectroscopy: High-Resolution Methods and Applications", 3rd Ed., VCH Publishers, Weinheim, Germany, 1987, pp73-105.
(12) Croasmun, W.R.; Carlson, R.M.K.: "Two-Dimensional NMR Spectroscopy: Applications for Chemists and Biochemists", 2nd Ed., VCH Publishers, Weinheim, Germany, 1994.
(13) Virk, P.S.: Prepr. Pap. - Am. Chem. Soc., Div. Fuel Chem., 44, (3), 546 (1999).
(14) Gray, G.A., Ch 1, pp 46-49 in Croasmun, W.R.; Carlson, R.M.K.: "Two-Dimensional NMR Spectroscopy: Applications for Chemists and Biochemists", 2nd Ed., VCH Publishers, Weinheim, Germany (1994).
(15) Zdonik, S.B.; Green, E.J.; Hallee, L.P: Oil Gas J., 66, (7) 192 (1969).
(16) Virk, P.S.; Korosi, A.; Woebcke, H.N: ACS Advances in Chemistry Series 183, 67-76 (1979a).
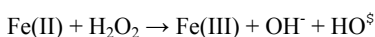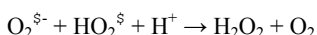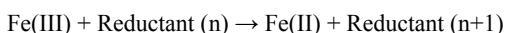(17) Virk, P.S.; Korosi, A.; Woebcke, H.N: ACS Advances in Chemistry Series 183, 77-89 (1979b).

BIOAVAILABILITY OF IRON FROM COAL FLY ASH

_Ann E. Aust_*, Kevin R. Smith*, John M. Veranth[§], Autumn A. Hu[§],
JoAnn S. Lighty[§]

*Department of Chemistry and Biochemistry, Utah State University,
Logan, UT; [§]Department of Chemical and Fuels Engineering,
University of Utah, Salt Lake City, UT

Introduction

Particulate air pollution is a complex mixture of organic and inorganic compounds, which contain transition metals, such as iron (usually most abundant), copper, nickel, vanadium, and cobalt. These metals can react with molecular oxygen in a series of one-electron reductions to produce the highly reactive hydroxyl radical HO$^\$$, as shown in the following reactions for iron:

$$Fe(III) + Reductant\ (n) \rightarrow Fe(II) + Reductant\ (n+1)$$

$$Fe(II) + O_2\ \Omega\ Fe(III) + O_2^{\$-}$$

$$O_2^{\$-} + HO_2^{\$} + H^+ \rightarrow H_2O_2 + O_2$$

$$Fe(II) + H_2O_2 \rightarrow Fe(III) + OH^- + HO^\$$$

The HO$^\$$ is by far the most damaging species in these reactions and is capable of reacting with all biological molecules. The reactivity of iron bound to proteins is controlled so that little if any generation of ROS will occur. However, iron bound in biological systems to low-molecular-weight chelators, such as citrate, is redox active. The above reactions will continue to cycle until all of the reductant or oxygen are consumed. Thus, a small amount of iron (or other transition metal) can produce a significant effect when not controlled by an appropriate protein.

Iron can exist in 16 different oxide forms, depending upon the conditions during the formation of the oxide. It is critical in studying particles containing iron to elucidate the form that is responsible for the effects observed. Some oxides of iron, such as hematite (Fe_2O_3) and magnetite (Fe_3O_4), are relatively inert [1] because the iron is unreactive in the solid and not easily mobilized from these particles. However, certain other forms, such as some ferric oxy/hydroxides (ferrihydrite), or iron in ionic interactions with silicates, e.g. asbestos [2], erionite [3] or other zeolites [4], are very reactive and the iron in these is capable of being easily mobilized. Therefore, the speciation of the iron in the solid absolutely determines the level of mobilization and reactivity of the iron.

The mobilization of iron from particulates into solution is highly dependent upon the pH. The rate increases as the pH decreases. However, at physiological pH (7.5), mobilization of iron from a particulate requires the presence of a chelator [2,6,7].

Particle Generation

Three commercially important coals were combusted in a pilot scale laboratory furnace under controlled conditions. The Illinois coal is a bituminous c coal with high iron levels as both included and excluded pyrite [9]. The North Dakota coal is a low iron-containing lignite, and the Utah coal is a bituminous b with low sulfur content. Smith _et al._ [10] reviewed the chemistry and combustion properties of these and other research coals.

The CFA samples to be studied were generated in a 30 kW furnace that simulates the time and gas temperature history of a full size coal-fired boiler. The furnace is described in detail by Spinti [11,12]. The fractions with mean aerodynamic diameter >10 μm, 2.5-10 μm, and <2.5 μm were collected 1 m from the exit, where the temperature was approximately 1000 K [9]. Less than 5% of the exhaust was extracted and cooled by nitrogen dilution before being directed into a 1 acfm Andersen cascade impactor. The >10 μm enriched CFA was collected by a preseparator that removes particles >10 μm before directing the flow to the Andersen impactor. The 2.5-10 μm and <2.5 μm fractions were collected on stages 1-3 and 5-7 of the impactor, respectively.

A second set of particles was generated after the original production. The second set included a <1 μm size that was not collected with the original set, but this necessitated changing the collection point and method [9].

Mobilization Of Iron

Because different sizes of CFA from different source coals contain differing amounts of iron, which may or may not be available to the cell upon endocytosis, a method was needed to determine the amount of bioavailable iron. Work done with crocidolite asbestos provided a method for determining bioavailable iron. Crocidolite contains 27% iron by weight and has been shown to catalyze many of the same reactions as iron _in vitro_, including HO$\$$ formation [13,14], DNA single-strand breaks [15], and lipid peroxidation [16,17]. Mobilization of iron from crocidolite was possible, but only in the presence of a chelator, such as EDTA or citrate [18]. Chao _et al._ [8] showed that iron mobilization by citrate in a cell free system correlates with the amount of iron mobilized from crocidolite in A549 cells.

Coal Fly Ash. Further studies of iron in particles were performed using the size fractioned CFA particles, as described previously [7]. The amount of iron mobilized from CFA was a function of particle size and of the parent coal [7], with the <2.5 μm fraction having more iron mobilized at 24 h than the 2.5-10 μm size fraction, which also had more mobilized iron than the >10 μm size fraction. The Utah <2.5 μm and 2.5-10 μm fractions had significantly higher iron mobilization levels than the same size fraction of either the Illinois or North Dakota CFA samples.

Ferritin levels were inversely related to size [7,19]. The Utah CFA samples induced 0.23 to 1.29 ng ferritin/μg total protein, while Illinois CFA samples yielded 0.36 to 0.98 ng ferritin/μg total protein, and North Dakota induced 0.14 to 0.51 ng ferritin/μg total protein. The control levels in all experiments were 0.08 ng ferritin/μg total protein. The increase in ferritin levels from one size to the next was shown to be statistically significant with $P < 0.05$ (Student=s t test). In addition to the inverse correlation to size, the induced level of ferritin also depended upon the source coal, Utah>Illinois>North Dakota. The ferritin levels induced by any given size fraction were found to be significantly different from the ferritin levels induced by the same size fraction of the other coals. The only exception being the Utah and Illinois 2.5-10 μm fractions, which were not statistically different.

Induction of Interleukin-8

Interleukin-8 is an important cytokine involved in inflammatory processes. Reactive oxygen species have been shown to be capable of inducing expression of IL-8 _in vitro_ [20-22]. Because iron mobilized away from endocytized particles can be involved in generating ROS, the hypothesis that iron present in CFA could induce IL-8 was investigated [19]. A549 cells were treated with three types of CFA at 10, 20 or 40 μg/cm^2 CFA and the medium was assayed for the presence of IL-8. The amount of IL-8 induced was directly proportional to the particle dose. As with the induction of ferritin, IL-8 synthesis was inversely related to particle size. The 20 μg/cm^2 dose of Utah <1 μm CFA increased IL-8 levels 5.6-fold over control. This same treatment also induced IL-8 synthesis at levels 1.2- and

3.6-fold higher than the same size fraction of Illinois and North Dakota CFA, respectively.

To more directly address whether iron was responsible for IL-8 induction, a sample of the Utah <1 μm CFA was incubated with 1 mM desferrioxamine B (DF) for 2 weeks with the DF changed approximately every two days [19]. This sample was then used to treat cells and IL-8 levels were determined. The DF-treated CFA failed to induce IL-8 levels above control levels while CFA incubated for two weeks in 50 mM NaCl induced the same levels of IL-8 as freshly suspended CFA. The DF-treated CFA was also tested for iron mobilization by citrate. After 24 h the amount of iron mobilized was 15-fold lower than before DF-treatment. These results strongly suggest that iron that can be mobilized from particles by citrate is the same pool of iron that is responsible for some of the biological effects of CFA in cultured cells.

Iron in Aluminosilicate Glass Was the Source of Bioavailable Iron

Iron in CFA is usually found in magnetite-based spinels, hematite, or glassy aluminosilicates [23-25]. Mössbauer spectroscopy was used to determine the speciation of iron in several samples. Analysis of CFA showed that the particles >10 μm (n=2) contained 43-47% iron in an aluminosilicate glass phase while samples <2.5 μm (n=2) contained 62-75% . The crustal dust sample contained no iron associated with aluminosilicate glass. DF treatment of the < 1 μm CFA for two weeks resulted in a substantial decrease in iron associated with glassy aluminosilicate from 62% to 44% of total iron. Comparison of the amount of iron removed by DF with the decrease in total iron associated with glassy aluminosilicate showed these values are consistent. This data suggests that the involvement of iron bound to glassy aluminosilicates in other sources of particulates should be investigated, since this iron was so easily mobilized from CFA.

Conclusions

The amount of bioavailable iron released from CFA is dependent upon the source of the parent coal and on the particle size, showing an increase in the amount of iron that can be mobilized with decreasing particle size [7,19]. This may be highly significant in view of the epidemiological observations that the smaller particles appear to be more responsible for the pathological health effects in humans. The induction of the iron storage protein ferritin was a reliable, indirect indicator of the amount of iron released in the cells and correlated strongly with the amount of iron mobilized by citrate in cell-free solution. Thus, one or both of these measurements for particles of unknown origin may prove very useful in determining whether the particles have the potential to release iron and generate ROS in the lung.

References
(1)   Fang, R. Ph.D. Dissertation, Utah State University, 1999.
(2)   Hardy, J. A.; Aust, A. E. *Chem. Rev.* **1995**, *95*, 97.
(3)   Eborn, S. K.; Aust, A. E. *Arch. Biochem. Biophys.* **1995**, *316*, 507.
(4)   Fubini, B.; Giamello, E.; Mollo, L.; Zanetti, G.; Eborn, S. K.; Aust, A. E. *Research of Chemical Intermediates* **1999**, *25*, 95.
(5)   Schneider, W. *Comments Inorg. Chem.* **1984**, *3*, 205.
(6)   Smith, K. R.; Aust, A. E. *Chem. Res. Toxicol.* **1997**, *10*, 828.
(7)   Smith, K. R.; Veranth, J. M.; Lighty, J. S.; Aust, A. E. *Chem. Res. Tox.* **1998**, *11*, 1494.
(8)   Chao, C.-C.; Lund, L. G.; Zinn, K. R.; Aust, A. E. *Arch. Biochem. Biophys.* **1994**, *314*, 384.
(9)   Veranth, J. M.; Smith, K. R.; Aust, A. E.; Dansie, S. L.; Griffith, J. B.; Hu, A. A.; Huggins, M. L.; Lighty, J. S. *Aerosol Science and Technology* **2000**, *32*, 127.
(10)   *The structure and reaction processes of coal*; Smith, K. L.; Smoot, L. D.; Fletcher, T. H.; Pugmire, R. J., Eds.; Plenum Press: New York, 1994.
(11)   Spinti, J. C. P. Ph.D. Thesis, University of Utah, 1997.
(12)   Spinti, J. C. P.; Pershing, D. W.; Brouwer, J.; Heap, M. P. *Combustion Science and Tech.* **1997**, *126*, 1.
(13)   Weitzman, S. A.; Graceffa, P. *Archives of Biochemistry and Biophysics* **1984**, *228*, 373.
(14)   Aust, A. E.; Lund, L. G. In *Mechanisms in Fibre Carcinogenesis*; Brown, R. C., Hoskins, J. A., Johnson, N. F., Eds.; Plenum Press: New York, 1991; Vol. 223.
(15)   Lund, L. G.; Aust, A. E. *Carcinogenesis* **1992**, *13*, 637.
(16)   Weitzman, S. A.; Weitberg, A. B. *Biochem. J.* **1985**, *225*, 259.
(17)   Gulumian, M.; Kilroe-Smith, T. A. *Environmental Research* **1987**, *44*, 254.
(18)   Lund, L. G.; Aust, A. E. *Arch. Biochem. Biophys.* **1990**, *278*, 60.
(19)   Smith, K. R.; Veranth, J. M.; Hu, A. A.; Lighty, J. S.; Aust, A. A. *Chem. Res. Toxicol.* **2000**, *13*, 118.
(20)   Simeonova, P. P.; Leonard, S.; Flood, L.; Shi, X.; Luster, M. I. *Lab Invest* **1999**, *79*, 1027.
(21)   Vlahopoulos, S.; Boldogh, I.; Casola, A.; Brasier, A. R. *Blood* **1999**, *94*, 1878.
(22)   DeForge, L. E.; Preston, A. M.; Takeuchi, E.; Kenney, J.; Boxer, L. A.; Remick, D. G. *The Journal of Biological Chemistry* **1993**, *268*, 25568.
(23)   Bancroft, G. M. *Mössbauer spectroscopy: an introduction for inorganic chemists and geochemists*; Wiley: New York,, 1973.
(24)   Huffman, G. P.; Huggins, F. E.; Dunmyre, G. R. *Fuel* **1981**, *60*, 585.
(25)   Hansen, L. D.; Silberman, D.; Fisher, G. L. *Environmental Science and Technology* **1981**, *15*, 1057.

COMPARISON OF MICRON-SIZED AND ULTRAFINE PARTICULATE MATTER FROM PULVERIZED COAL COMBUSTION

Yuanzhi Chen, Naresh Shah, Frank E. Huggins, and Gerald P. Huffman

CFFS/CME, University of Kentucky, 533 South Limestone Street, Lexington, KY 40508-4005

Introduction

Coal combustion generates large quantities of fly ash every day. Although control devices, such as electrostatic precipitators, fabric filters and particle scrubbers have been applied at most large coal-fired electric utility boilers in the United States, there is still a small portion of fly ash particles, especially ultrafine (<100 nm) particles, that can escape from these devices and contribute primarily to the fine particle component of ambient particulate matter (PM) that is less than 2.5 µm in mean diameter ($PM_{2.5}$). Epidemiological studies have demonstrated correlations between atmospheric concentrations of ambient $PM_{2.5}$ particles and adverse health effects, such as an increased risk of pulmonary and cardiovascular diseases and mortality (1, 2). However, there are many uncertainties regarding the actual toxicological mechanisms, which may be closely related with the physicochemical characteristics of individual PM particles, such as size, morphology, crystallinity, chemical composition, and so on.

Microanalysis of individual particles is a necessary complement to conventional bulk analysis. The morphology, size, and composition of micron and even submicron coal fly ash particles have been well characterized by a variety of electron microscopy techniques; however, scant information is available on ultrafine particles. A recent study showed that ultrafine coal fly ash particles have more *in vivo* toxicity than do fine and coarse particles taken from the same combustion aerosol (3). It is therefore interesting to conduct comparative studies on individual particulate characteristics, which may eventually be used for the establishment of the involved toxicological mechanisms of coal fly ash particles.

In this study, micron-sized and ultrafine fractions of coal fly-ash PM samples generated from combustion of three U. S. coals have been studied by computer controlled scanning electron microscopy (CCSEM) and analytic transmission electron microscopy (TEM). Data on the microcharacteristics of individual particles should be useful for epidemiological, toxicological, and source apportionment studies of coal fly ash particles.

Experimental

Coal fly ash PM samples were generated from combustion experiments conducted at the U.S. Environmental Protection Agency (EPA) National Risk Management Research Laboratory (NRMRL) at Research Triangle Park, NC. Coal fly ash generated by combustion of one high-volatile bituminous coal from Western Kentucky and two subbituminous coals from Wyoming (Powder River Basin) and Montana was separated into fractions with mean diameter >2.5 µm ($PM_{2.5+}$) and <2.5 µm ($PM_{2.5}$) with a cyclone. For CCSEM analysis, the coal fly ash powders (both $PM_{2.5+}$ and $PM_{2.5}$ fractions) were dispersed onto a polycarbonate filter by sonication in and filtration from high-purity methanol, while for TEM analysis, the powders (just the $PM_{2.5}$ fractions) were dispersed in acetone and then transferred to TEM grids coated with lacey carbon or holey carbon films. A Hitachi S-3200 scanning electron microscope and a 200 kV field emission analytical transmission electron microscope (JEOL JEM-2010F) were used for the CCSEM analysis and for the TEM analysis, respectively.

Results and Discussion

Carbonaceous particles. The observed carbonaceous particles could be subdivided into two major categories, i.e. char and soot aggregate. Char particles are typically distributed in the micron-sized fraction. Most char particles have porous structures with spherical or irregular shapes (Figure 1, top left), while some of char particles have a more solid structure and less porosity (Figure 1, top right). Soot aggregates typically have branching morphologies and dominate the ultrafine and submicron (0.1-1 µm) fractions. Typical ultrafine soot aggregates (Figure 1, bottom right) have spherical primary particles with typical sizes of 30~50 nm and aggregate sizes varying from less than 0.1 µm to microns. Small amounts of submicron soot aggregates (Figure 1, bottom left) that also have spherical primary particles but with larger sizes (typically 0.1- 0.4 µm) have also been observed in the Western Kentucky coal fly ash PM sample. The morphological differences between soot and char particles are mainly related to their formation mechanisms. Soot particles are mostly newly formed from the establishment of nuclei from precursory chemical reactions among fuel molecules followed by surface growth and collisions leading to the aggregate morphology, whereas char particles are largely remnants derived from pyrolysis and oxidation of fuel particles. The fuel nature, fuel/air ratio, temperature and duration of combustion determine more specifically the morphologies of these carbonaceous particles.
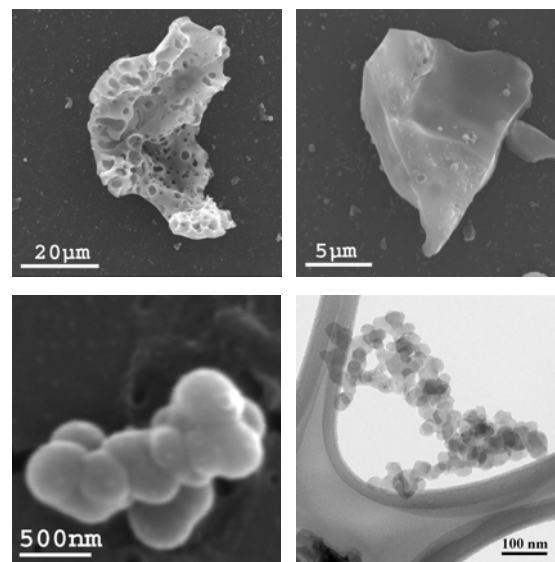

Figure 1. Top left: SEM image of a porous char particle. Top right: SEM image of a solid char particle. Bottom left: SEM image of a submicron soot aggregate. Bottom right: TEM image of an ultrafine soot aggregate.

The microstructural differences between char and soot particles are reflected in their HRTEM images. Typical HRTEM images (Figure 2, left) of an ultrafine soot primary particle show an onion-like microtexture that consists of concentrically arranged graphitic layers. This type of microstructure is similar to those reported in studies of carbon blacks (4) and diesel soot (5). Submicron soot primary particles also exhibit similar microstructures. Char particles normally do not show concentric microtextures like those observed in soot particles. They typically demonstrate anisotropic arrangements

of roughly parallel or highly curved graphitic layers with varying lengths and thicknesses (Figure 2, right). A turbostratic microstructure where graphitic layers in the basic structure units are shifted against each other has also been indicated in electron diffraction patterns of char and soot aggregates.
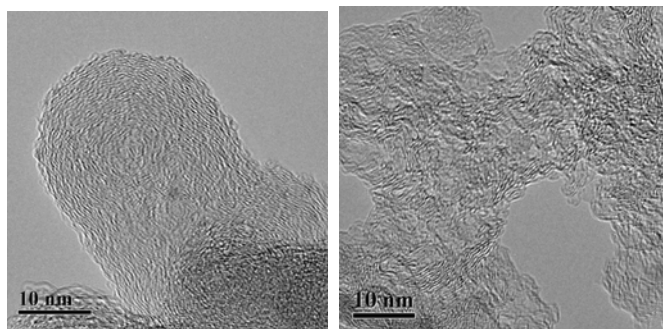

Figure 2. HRTEM images of an ultrafine soot primary particle (left) and a char particle (right).
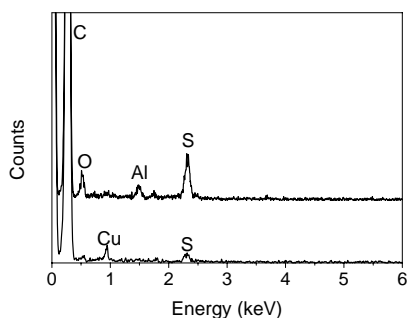

Figure 3. Comparison of EDS spectra of a char particle (top) and an ultrafine soot aggregate (bottom). Cu peak is due to TEM grids

Energy dispersive x-ray spectroscopy (EDS) can be used to reveal elemental compositions of carbonaceous particles. Typical EDS spectra of carbonaceous particles show a strong carbon peak and much weaker, but discernable, O and S peaks. One of the compositional differences between soot and char particles is that some char particles contain more discernable sulfur and metallic elements than soot particles. Figure 3 compares the EDS spectra of a char particle and an ultrafine soot primary particle from the Western Kentucky coal fly ash PM sample. The spectra are normalized to the height of carbon peak for convenience of comparison. The char particle contains relatively more sulfur and aluminum than does the soot particle. XAFS analysis of the same samples (6) indicated that thiophenic sulfur was the major chemical form of organic sulfur in coal fly ash. The chemical form of metallic elements in char particles needs further investigation. The soot aggregates in the western low-rank coal fly ash PM samples are frequently mixed or coated with inorganic species rich in alkali and alkaline earth elements, which may be useful as a fingerprint for source apportionment studies.

Inorganic particles. Typical micron-sized coal fly ash particles have spherical or rounded morphologies as shown in Figure 4. Particle-size distributions obtained by CCSEM show that particles with mean diameter less than 2.5 μm constitute 80-95% of the total number of particles, whereas particles with mean diameter larger than 2.5 μm constitute 80-95% of the total particle volume and mass.
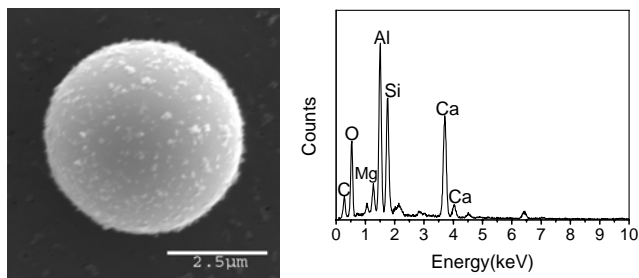

Figure 4. Left: Typical SEM image of a spherical micron-sized aluminosilicate particle. Right: EDS spectrum of the same particle.

Chemical classifications of individual micron-sized particles show marked compositional differences among the three coal fly ash PM samples. The Western Kentucky coal fly ash PM sample contains abundant aluminosilicate and Fe-aluminosilicate particles, while the Wyoming PRB coal fly ash PM sample is rich in Ca-aluminosilicate and Na-aluminosilicate particles, and the Montana coal fly ash PM sample is dominated by Ca-aluminosilicate particles. Since eastern bituminous coals contain abundant pyrite, the iron oxides derived from pyrite can react with illite, kaolinite, and quartz and lead to the formation of Fe-aluminosilicates. Fe-aluminosilicates also can form from the melting of illite, which is generally much more abundant in eastern coals than in western coals. Glassy particles in western low-rank coal fly ash PM samples are formed by the reaction of Ca and Na, which are present in low-rank western coals as carboxyl-bound molecular species, with kaolinite and, to a lesser extent, with quartz. The compositional ranges of these aluminosilicate particles can be better represented using the ternary diagrams. Detailed results about the ternary diagrams of these aluminosilicate particles are available elsewhere (7). The ternary diagrams derived from CCSEM data for coal fly ash PM samples are characteristic of the mineralogy of the coals that were combusted to produce them. For example, K is usually the major alkali in eastern bituminous coals and is dominantly contained in the mineral illite, which becomes partially molten at temperatures above approximately 900 °C (8). Little change in composition occurs unless there are reactions with Fe oxides. Consequently, the K-Si-Al ternary diagrams for eastern coal fly ash PM samples exhibit high volume percentages in the region appropriate for the composition of the mineral illite. Therefore, the ternary diagrams using CCSEM data should be useful for source attribution.

The inorganic ultrafine particles exhibit quite different morphologies, compositions and microstructures compared with the micron-sized particles. The Western Kentucky coal fly ash PM sample exhibits abundant discrete crystals that are rich in Fe, Ti and Al in its ultrafine fraction. Nanocrystals encapsulated in or associate with char particles are common in the sample. The inorganic ultrafine particles typically have angular or subrounded shapes instead of spherical shapes, and can be grouped into one-element chemical category (e.g. Fe-rich and Ti-rich) or two or multi-element chemical categories (e.g. Al-Ti and Ti-Al-Fe). Many chemical categories in the ultrafine fraction, such as Ti-rich, Ti-Al-Fe and Ti-Si-Al, are not present in the micron-sized fraction, while some categories, such as K-Si-Al that are present in the micron-sized fraction, are not found in the ultrafine fraction. Crystalline phases, such as magnetite, rutile, lime, and Fe-Al spinel have been identified. Figure 5 gives a typical example of an ultrafine iron oxide particle observed in the Western Kentucky coal fly ash PM sample. The selected area electron

diffraction (SAED) pattern recorded from this particle reveals characteristics typical of a single crystal, which can be indexed to magnetite. Ultrafine Fe-aluminosilicate particles tend to be Fe-rich and thereby differ from micron-size Fe-aluminosilicate particles that usually have abundant Si and Al. Composite Fe-aluminosilicate particles have been found to consist of Fe oxide or Fe-Al spinel spherules distributed in the aluminosilicate or silicon oxide matrix.
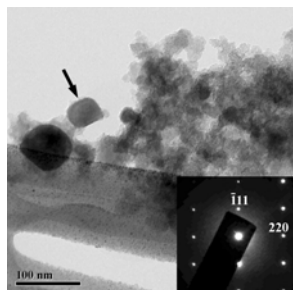

Figure 5. TEM image of an ultrafine iron oxide particle (arrowed) in Western Kentucky coal fly ash $PM_{2.5}$ sample. Inset is its SAED pattern, indexed to magnetite.

The ultrafine fraction of Wyoming PRB coal fly ash PM sample contains abundant Ca and Mg phosphates, phosphate-silicates and phosphate-sulfates. Inorganic single-element particles are of very limited occurrence. Figure 6 shows a typical morphology of an inorganic aggregate with primary particles having sizes of 30-50 nm. The chemical composition of this aggregate given by EDS consists mainly of Ca, P and O, indicating a likely presence of a calcium phosphate. These branching inorganic aggregates are frequently found in the sample, indicating that vaporization-condensation mechanisms dominate the formation process. Separate spherical Ca phosphates can also be found in larger sizes, which could be due to the coalescence of the primary particles or to decomposition of original phosphate minerals, such as apatite. Lesser amounts of carbonaceous particles are found in the Wyoming PRB sample, indicating a more complete combustion, which should have led to increased vaporization of inorganic minerals via a series of fume reactions, producing multi-element categories, such as Ca-P-S and Ca-P-Si.

A typical morphology of inorganic ultrafine particles in the Montana coal fly ash PM sample consists of fused aggregates with sizes extending into the submicron range. Ca-aluminosilicates, which are dominant in the micron-sized fraction, are barely found in the ultrafine fraction. Ca-S, Ca-S-Si and some multi-element chemical categories are observed. The multi-element chemical categories typically reflect reactions taking place among these elements, possibly in the vapor phase. The ultrafine particles are often captured by big particles and form a heterogeneous layer on their surfaces. Such a typical example is shown in Figure 7, in which ultrafine Ca and Mg sulfates are captured by a larger spherical Ca aluminosilicate particle. Since alkaline earth and alkali compounds are easily vaporized or form fumes under combustion condition, they may condense on the surface of larger inorganic particles or soot aggregates, forming ultrafine particles or inorganic layers. HRTEM images taken from many Ca sulfate-silicate particles show that both amorphous and microcrystalline structures coexist in these particles. Anhydrite was identified as one of the major crystalline components.
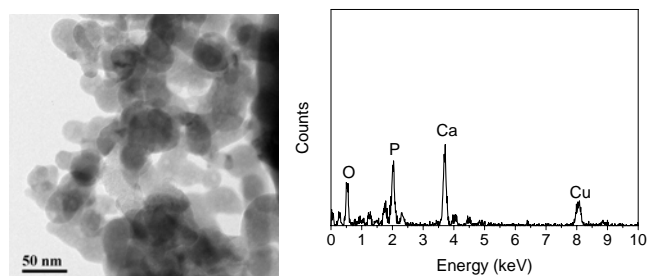

Figure 6. TEM image (left) and EDS spectrum (right) of ultrafine Ca phosphates in Wyoming PRB coal fly ash $PM_{2.5}$ samples.
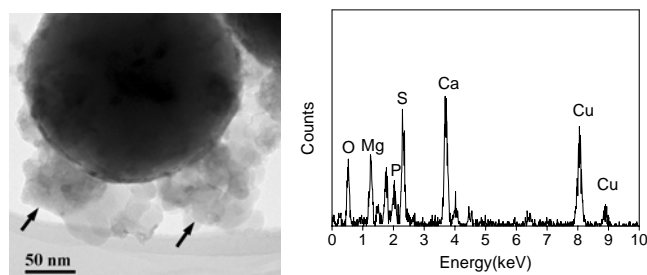

Figure 7. TEM image (left) and EDS spectrum (right) of ultrafine Ca and Mg sulfates (arrowed) attached on a spherical Ca aluminosilicate particle. (Montana coal fly ash $PM_{2.5}$ samples)

Conclusions

The carbonaceous PM in the three coal fly ash PM samples examined in this study consist of micron-sized char particles and ultrafine soot aggregates that typically have branching morphologies with spherical primary particles having a size of 30-50 nm. The HRTEM observation shows that soot primary particles consist of concentrically stacked graphitic layers with interlayer spacings larger than that of graphite. Such concentric microtextures have not been observed in the char particles, which typically exhibit heterogeneous microtextures. Compositional analysis by EDS indicates that, besides the dominant carbon, discernable S and O may also be present in these carbonaceous particles. Small amounts of metallic elements (e.g. Al and Ti) can be observed in some char particles in the Western Kentucky coal fly ash PM sample. In the western low-rank coal fly ash PM samples, the ultrafine soot aggregates are typically mixed or coated with inorganic species rich in alkaline earth and alkali elements.

Morphological, compositional and microstructural differences have been observed between the inorganic micron-sized and ultrafine coal fly ash particles. The inorganic micron-sized coal fly ash particles are dominated by aluminosilicates that typically have spherical morphologies. Fe-aluminosilicates are typical for the eastern bituminous (Western Kentucky) coal fly ash PM sample, while Ca-aluminosilicates are typical for the western low-rank (Wyoming PRB and Montana) coal fly ash PM samples. The inorganic ultrafine particles in the Western Kentucky coal fly ash PM sample typically exist in discrete crystalline particles that are rich in Fe, Ti and Al, whereas those in the Wyoming PRB and Montana coal fly ash PM samples consist of alkaline-earth element aggregates in the form of phosphates, silicates, and sulfates and mixed species.

References
(1) Dockery, D. W.; Pope, C. A. *Ann. Rev. of Publ. Health*, **1994**, *15*, 107-132.
(2) Schwartz, J.; Dockery D. W.; Neas, L. M. *J. Air Waste Manage. Assoc.* **1996**, *46*, 927-939.
(3) Gilmour, M. I.; O'Connor, S.; Dick, C. A. J.; Miller, C. A.; Linak, W. P. *J. Air Waste Manage. Assoc.*, **2003**, *54*, 286-295.
(4) Donnet, J. B. *Carbon*, **1982**, *20*, 267-282.
(5) Ishiguro, T.; Takatori, Y.; Akihama, K. *Combust. Flame*, **1997**, *108*, 231-234.
(6) Huffman, G. P.; Huggins, F. E.; Shah, N.; Huggins, R.; Linak, W. P.; Miller, C. A.; Pugmire, R. J.; Meuzelaar, H. L. C.; Seehra, M. S.; Mannivannan, A. *J. Air Waste Manage. Assoc.* **2000**, *50*, 1106-1114.
(7) Chen, Y.; Shah, N.; Huggins, F. E.; Huffman, G. P.; Linak, W. P.; Miller, C. A. *Fuel Process. Technol.* **2004**, *85*, 743-761.
(8) Huffman, G. P.; Shah, A.; Shah N.; Zhao, J.; Huggins, F.; Helble, J.; Srinivasachar, S.; Peterson, T.; Wendt, J.; Gallagher, N.; Bool, L.; Sarofim, A. *Proceedings of the 1993 Engr. Fd. Conf., The Impact of Ash Deposition on Coal Fired Plants*, Eds., J. Williamson and F. Wigley, **1994**, pp 409-423, Taylor & Francis, London.

EFFECTS OF BURNING BLENDED COALS ON ELECTROSTATIC PRECIPITATOR PERFORMANCE

Manyin Hu[1], Hezhong Tian[2], Zhong Liu[1], Lifeng Li[1]

1. School of Environmental Science and Engineering, North China Electric Power University, Baoding 071003, China
2. Department of Environmental Science and Engineering, Tsinghua University, Beijing 100084, China

Introduction

Energy is one of the important factors restricting the sustainable development of China. China is one of a few countries in the world whose energy mix is dominated by coal, with a share of nearly 70% of the total energy consumption. Further, the majority of coals are burned directly by utility boilers, industry boilers, and furnace kilns. Combustion efficiency and energy consumption level are directly influenced by the variety and characteristics of burned coal. The so called "blended coals" means some different types coals with different characteristics are mixed together and processed into a new kind of coal, which can meet various demand by altering the proportional ratio of mixing coal source. Rational proportioning of blended coals can exert advantages of each mixing coal and offset the weakness, thus bring favorable effects for security and economic operation of burning facilities. However, inappropriate proportioning ratio can cause some problems and even serious accidents sometimes, such as burning difficulty, unstable burning, combustion efficiency drop, slag formation and soot deposit intensifying, pollutants discharge increasing, and even boiler blowout, etc. According to investigation, the thermal efficiency of boiler can increase 4%~5% and the rate of saving coal use can reach up to 5% by firing blended coals of rational proportioning compared with firing one single original coal. Thus, firing blended coals is not only in favor of coal resource utilizing with high efficiency, also will bring much benefit on environment protection. So, there is huge potential and great practice significance of developing blended coals in China.

Chinese scientists have made a lot of studies on the burning characteristics of blended coals [1,2]. Firing blended coals in utility boilers in foreign countries has been recognized and phased in. By integrated calculation of some key parameters of the received coals, such as heat value, sulfur content, ash content, ash melting temperature, the homogeneous and optimal of feed coal burning for utility boilers can be achieved, and thus obtain good benefits [2]. In general, burning blended coals can bring the following benefits: increasing coal utilization efficiency, especially for some inferior coals, thus saving coal resources; improving coal firing and achieving stable combustion; advancing burning efficiency; decreasing formation of slag, preventing accidents of blowout the boiler; and lowering pollutants formation and discharge.

Boiler burning and operation conditions have much impact on ESP performance [3]. So, burning blended coal may bring great effects to the safe and economical operation of ESP. In this paper, effects of the proportioning of different original coals on the performance of ESP is analyzed and investigated by programming simulation, and some laws of practical significance are obtained. This will provide for some theoretical basis for blended coals firing and the security and high efficiency running of ESP.

Methodology and Materials

Mixing original component coals selection. In this paper, not only considering the difference of coal's characteristics, but also giving attention to the coal source location when selecting the original coal types for mixing. The original mixing coals are selected in the same area as far as possible when considering the proportioning of different coals. Thus, this not only accounts for the difference of coal's characteristics in the same area, but also gives much attention to the transportation and the possibility of establishing the regional blended coal base. Therefore, totally 7 types of coals were selected for example in eastern China in this paper. The elemental analysis results of the selected original coal were shown in **Table 1**.

Table 1. Elemental Analysis Results of the Selected Raw Coal

Coal type	C^y /%	H^y /%	O^y /%	N^y /%	S^y /%	W^y /%	A^y /%	Q_d^y /kJ·kg^{-1}
Zibo soft coal	65.64	2.84	2.34	0.10	3.37	4.91	20.90	25636
Huaibei soft coal	48.47	3.42	5.53	2.87	0.30	6.34	33.25	18422
Zaozhuang soft coal	56.90	3.64	2.25	0.88	3.21	7.71	25.41	22362
Huainan soft coal	57.03	3.63	6.28	1.03	0.54	7.06	24.43	22148
Xuzhou soft coal	54.43	3.12	2.00	0.80	0.39	6.60	32.66	17823
Xinwen soft coal	61.00	4.10	6.80	1.40	1.90	6.00	18.80	25140
Yima soft coal	62.57	3.22	1.69	0.93	1.23	6.40	27.17	23865

Results and Discussion

The investigated blended coals were prepared with 3 types of component coals in this paper. Then, effects of firing blended coals with different proportioning on flue gas volume (Q), boiler efficiency (N_g), dust removal efficiency of ESP (N_e), flue gas moist content (X_{H2O}), dust driving velocity of ESP (We), dust concentration of flue gas (C), were analyzed and studied in detail.

There were totally 17 series of blended coals were investigated in this paper, which were confected by different confection fashion and proportion with 7 different types of original component coal. **Table 2** and gives out the simulated results, and the simulating results of blended coals, which was prepared by 3 types of component coals (Xuzhou soft coal, Huainan soft coal, and Xinwen soft coal) with different mixing proportion ratio, was shown in **Figure 1~Figure 4**, respectively.

Table 2. The Proportioning of Coal Types and Simulating Results

No.	Coal sample	Q m^3·s^{-1}	N_g %	N_e %	X_{H2O} %	C_{SO2} ×10^{-6}	W_e m·s^{-1}	C_A mg·m^{-3}
1	**Xu**zhou soft coal	639.16	89.67	98.24	3.03	185	4.11	19.82
2	**Hu**ainan soft coal	530.25	91.02	99.23	4.15	243	5.03	19.17
3	**Xi**nwen soft coal	505.03	91.34	99.39	4.13	790	11.05	10.04
4	Xu30H20Xi50	541.87	90.88	99.14	4.29	515	8.19	13.57
5	Xu30H30Xi40	544.81	90.84	99.12	4.29	459	7.58	14.51
6	Xu30H40Xi30	548.00	90.80	99.10	4.07	403	6.94	14.44
7	Xu30H45Xi25	549.58	90.80	99.09	4.07	373	6.61	14.67
8	Xu20H30Xi50	533.24	90.98	99.21	4.09	519	8.25	13.05
9	Xu20H35Xi45	534.65	90.96	99.20	4.09	492	7.95	13.26
10	Xu20H40Xi40	536.08	90.95	99.19	4.09	464	7.65	13.48
11	Xu20H45Xi35	537.53	90.93	99.18	4.09	435	7.34	13.69
12	Xu20H50Xi30	539.00	90.91	99.17	4.09	408	7.02	13.91
13	Xu25H20Xi55	536.08	90.95	99.19	4.08	445	8.51	13.10
14	Xu25H30Xi45	538.97	90.91	99.17	4.08	490	8.25	13.52
15	Xu25H40Xi35	541.94	90.87	99.14	4.08	434	7.30	13.96
16	Xu35H40Xi25	554.28	90.72	99.05	4.06	372	6.57	14.94
17	Xu40H30Xi30	557.39	90.68	99.02	4.04	398	6.87	14.98

Burning mode and calculation. The combustion process of blended coals was completely different from separate burning of every single original coal. It will show the interaction results of every component coals when several coals burn with proportioning. In this paper, each series of blended coals will be considered as a completely

new type of coal, and the key parameters such as elemental analysis will be obtained according to the proportioning ratio of each component coal and their elemental analysis results. All of the simulating calculations are based on a reference type of utility boiler, name by DG-1025/177-2.

Effects on low heat value of feed coal (Q_d^y). Coal heat value Q_d^y will mainly affected the flue gas volume produced when burning. As can be seen from **Figure 1** to **Figure 3,** if Q_d^y increasing, flue gas volume decreased, the velocity of flue gas fell, the specific dust collecting area increased, it is favorable for the running of ESP. The flue gas volume decreased but boiler efficiency and dust removal efficiency increased following the increasing of proportion of the coal with higher value of Q_d^y in blended coals. So, the proportion of the medium (about 20000kJ/kg) or rather higher in coals increased properly, not only will be favorable for boiler efficiency improvement, but also will benefit the running efficiency of ESP.
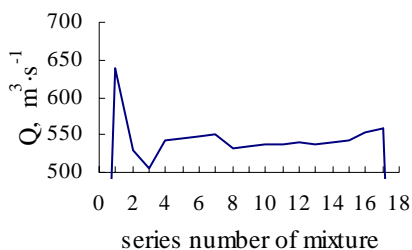
Figure 1. Relationship between flue gas volume and different component coal proportioning
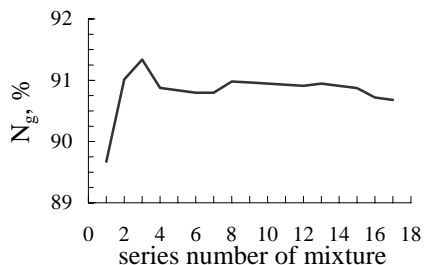

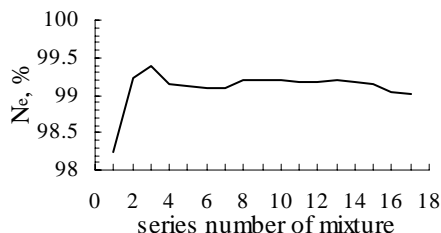**Figure 2.** Relationship between boiler efficiency and proportioning

Figure 3. Relationship between ESP efficiency and proportioning

Effects on coal ash content (A_y). The ash content (A_y) mainly affected the fly ash volume and dust concentration in flue gas. As seen from **Figure 4**, flue gas dust concentration gradually grows with the increase of coal proportion with higher A_y value in the blended coals. Due to increasing of flue gas dust concentration, the removal dust efficiency of ESP increased in a certain range, the proportion of component coal with higher A_y value in the blended coals was as big as possible under the conditions of satisfying in the secure and stable ESP operation. It is favorable for efficient utilization of inferior coal.

However, for some inferior coal with very high A_y value, the caused high flue gas dust concentration could lead to corona close down phenomenon in ESP, which will influence the normal operation of ESP, and even cause the unstable operation of boiler. These could be avoided by blending some suitable proportioning coals with lower A_y value.
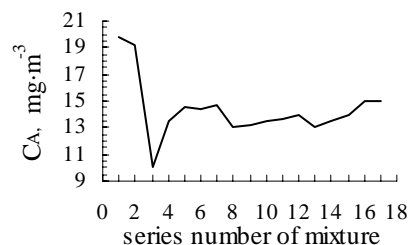

Figure 4. Relationship between dust concentration and proportioning

Effects of coal water content (W_y). The water content (W_y) of burning coal mainly affected the moisture content of flue gas. When burning coal with the lower W_y value, flue gas moisture content will decrease, and the specific resistance of dust will increase, which is unfavorable for the dust collection of ESP. However, It is favorable for dust coagulation, decreasing of specific resistance of dust, and thus enhancing dust collection efficiency by increasing W_y properly. If coal W_y value is too high, some problems such as dewfall eroding and soot deposit will occurred by higher flue gas moisture content, and will influence the normal running of ESP. Therefore, mixing a component coal with higher Q_d^y, lower W_y value and another component coal with lower Q_d^y, higher W_y value, the resulted blended coals could keep each component's advantage and remedy disadvantage, thus improve the running conditions of boiler and ESP.

Effects of sulfur content of feed coal (S_y) on ESP. Coal S_y value affects driving velocity of dust for ESP operation, and then affected dust removal efficiency of ESP. Also, coal S_y value decided flue gas SO_2 concentration. Some disadvantage of single type of coal could be improved by proportioning burning of three types of coals. For example, the dust driving velocity burning Huaibei soft coal was very low, but it could be enhanced from 3.487cm/s to 9.00cm/s when burning blended coals by mixing Yima soft coal and Zaozhuang soft coal with proportioning ratio. Thus, ESP performance improved. In addition, the much higher SO_2 emission burning Zaozhuang soft coal can be avoided, which is favorable for environmental protection.

Conclusions

Coal's characteristics differs much from different regions in China, and it has much impacts on boiler and ESP performance. In this paper, based on 7 types of selected component coals in east China, the effects of burning blend coals with different proportioning ratio on boiler and ESP performance were simulated and discussed in detail. It implies that appropriate proportioning coals with different characteristics will not only benefit for inferior coal use and ESP performance, also the caused air pollution will be lessened. Therefore, it is very important to establish regional blended coals manufacturing field in China for energy conservation and environmental protection.

References
(1) Yao Q., Cen K.F., Shi Z.R., et al. *Power Engineering*. **1997**, 17(2), 16.
(2) Dai H.W., Ma S.Y., Li L.Z., et al. *Machining and Synthesis Utilization of Coals*. **1997**, 5, 50.
(3) Hu M.Y., Gao X.L., Hu Z.G., et al. *Proceedings of the CSEE*. **1997**.17(4), 278.

NITROGEN OXIDES EMISSION AND CONTROL FROM COAL-FIRED POWER PLANTS IN CHINA

Hezhong Tian, Jiming Hao, Yongfeng Nie

Department of Environmental Science and Engineering
Tsinghua University, Beijing 100084, China
E-mail: tianhezhong@tsinghua.org.cn

Introduction

Anthropogenic nitrogen oxides (NO$_X$) emissions are relevant with various negative effects on ecosystems and human health, such as acidification, eutrophication, ground-level ozone, secondary fine particulate matters formation and loss of biodiversity [1]. With the rapid economic growth and coal-dominated energy consumption increase, emissions of NO$_X$ and the caused local air pollution and regional acid deposition are becoming worsened. According to SEPA, ambient air NO$_X$ concentration in some large cities such as Beijing, Guangzhou is quite high, acid rain (pH<5.6) occurred in 95 cities, a share of 89.6% of the total 106 cities monitored in the Acid Rain Control Zone in China, areas with acid precipitation have accounted for about 40% of the whole territory, and the situation in some badly polluted areas is worsening, such as Pingxiang in Jiangxi province, Jishou in Hunan province, et al [2]. Further, the ratio of [SO$_4^{2-}$]/[NO$_3^-$] of precipitation in some cities of the southeastern areas has declined from about 6:1 to about 2:1, it implies that the contribution of NO$_X$ emissions to acid rain pollution in China is increasing, and NO$_X$ emission control should be emphasized.

NO$_X$ discharged from the elevated stack of coal-fired utility boilers have much impact on regional acid rain and fine particulate matters through complex atmospheric chemical processes. By now, coal-fired thermal power plants have become the largest energy use sectors, consuming over 1/2 of the total coal consumption in China. Therefore, it is of great significance to know about the status of NO$_X$ emissions and feasible control ways for coal-fired power plants.

Methodology and materials

Domain. In this paper, the regions studied cover 31 provinces / autonomous regions / municipalities on the Chinese mainland; Hong Kong Special Administrative Region (HKSAR), Macau Special Administrative Region (MSAR) and Taiwan province are not included. The historical time period considered is from the year of 1990 to the year of 2003. Further, the regional distribution will be investigated.

Methodology for NO$_X$ Emissions Estimation. Combined with the average NO$_X$ emission coefficient, the corresponding coal use rate, as well as the removal efficiency, the emissions of NO$_X$ from coal-fired power plants in China can be calculated, which can be expressed as the following hierarchical formula [3,4]

$$Q_T^N(t) = \sum_i Q_i^N(t) \tag{1}$$

$$Q_i^N(t) = (1 - P^N(t))K^N(t)F_i(t) \times 10^{-3} \tag{2}$$

Where: Q^N= Emissions of NO$_X$ pollutants calculated as NO$_2$, t; K^N=Emission factor of NO$_X$ weighted as NO$_2$, kg/t-coal; F=Coal consumption, t; P^N=Efficiency of NO$_X$ removed by pollution control measures; T=China; t=Year; i=Province (autonomous region or municipality).

Emission Factor of NO$_X$. The NO$_X$ emission level of coal fired utility boilers was influenced by many conditions, such as coal characteristics (heat value, N content, ratio of volatile and fixed carbon (V/F), ash content, etc.), boiler capacity and load, burner

patterns and its configuration, dry-bottom or wet-bottom, with or without low NO$_X$ burners, etc.

Now, coal-fired power plants accounted for about 80% of total thermal power installed generating in China, and over 90% of coal-fired utility boilers were dry-bottom. Among the total 4092 coal-fired pulverized boilers in China in 2000, there were only about 400 boilers equipped with different types of low NO$_X$ burners (LNBs), less than 10% of the totals. By 2003, the installed capacities with SCR system were only 6×600MW, which were all installed at Houshi power plant in Fujian province. Therefore, the NO$_X$ emission level of utility boilers is still relatively high.

In order to know about the real NO$_X$ emission level of coal-fired power plants, some utility boilers were investigated, which were different scale of installed capacity, located at 6 different provinces, burned with coal with different characteristics, different burner pattern and configuration, and with or without LNBs, et al. **Figure 1** gives out the investigated emission level of coal-fired power plants.
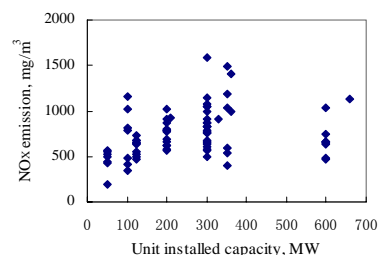

Figure 1. NO$_X$ emission level of utility boilers in China (O$_2$=6%)

As can be seen, the NO$_X$ emission concentration of utility boilers differs from different installed capacity, different boiler pattern and burner configuration, as well as coal with different characteristics. The overall average concentration ranged about 750~1100mg/m^3. Based on integrated calculation and analysis, the average NO$_X$ emission coefficient of utility boilers was about 8.85kg/t-coal [4].

Coal Use. The necessary coal consumption data during the period from 1990 to 2003 were derived from energy balance tables of the whole nation and/or each province [5].

Results and Discussion

Status of coal-fired power plants. Since 1990, the newly commissioned thermal power installed capacities have kept at a rate of over 10000MW per year. By the end of 2000, the total installed capacity and generating electricity have reached 319.3GW and 1368.5TWh, respectively. Coal-fired generating electricity reached at 1081.0TWh, accounting for 80% of the total electricity generated. The total coal consumption has increased from 1055.23Mt in 1990 to 1637.32Mt in 2003, while the he share of coal used for thermal power generation has increased from to 25% in 1990 to 53.5% in 2003. The structure of electricity generation in 2000 was shown in **Figure 2**, and the change of coal consumption was shown in **Figure 3** [5].
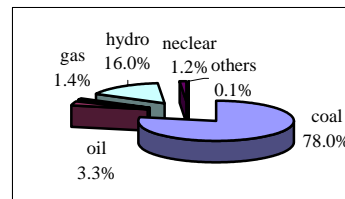

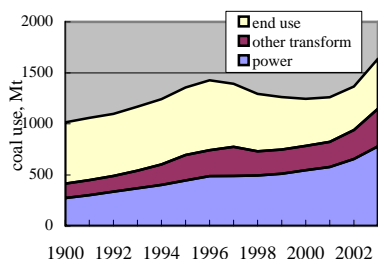**Figure 2**. Structure of electricity generation in China, 2000

Figure 3. Structure of coal consumption in China, 1990-2003

Trends of NO$_X$ emissions from coal-fired power plants. According to the statistical data of coal use in the recent years, and the confirmed NO$_X$ emission factor, the NO$_X$ emissions from coal-fired power plants were evaluated. **Figure 4** gives out the change of total NO$_X$ emissions from coal-fired power plants in China. As can be seen, with the rapid economy growth and increasing demand for clean electricity, as well as the domestic resource restrict, burning coal consumption and the produced NO$_X$ emissions from coal-fired power plants have been kept increasing, from 2.41Mt in 1990 to 6.90Mt in 2003, with an annual growth rate of 8.4%. Therein, more than 95% of the total emissions were emitted from the units with generating capacity of 6MW and above. Especially, the emissions increased very quickly in the last 3 years since 2000, with a growth rate of as high as 12.6%. According to the medium and long-term planning in China, most of the increased coal production in the future will used by coal-fired utility boilers. It implies that NO$_X$ emissions from coal-fired power plants will still increase steadily if none effective measures taken, thus make great contributions on acid rain.
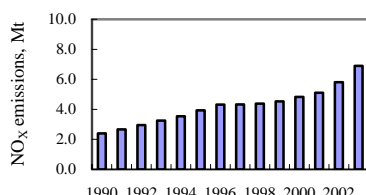

Figure 4. NO$_X$ emissions from coal-fired power plants, 1999~2003

NO$_X$ Emissions by Province. The calculated NO$_X$ emissions by province in the year of 2000 and 2002 were shown in **Table 1**. As can be seen, most of the emissions come from the eastern and central areas of China, which were densely populated, relatively industry intensive, and/or energy resource abundant. The provinces with higher emissions included Hebei, Liaoning, Shandong, Guandong, Jiangsu, Henan, Shanxi, et al. This could be mainly attributed to the situation of coal-fired power plants location distribution in China. However, with the establishment of large–scale thermal power base in the Western areas and the implementation of transferring electricity from the West to the East, it is anticipated that NO$_X$ emissions from some western provinces such as Guizhou and Ningxia, will be increased substantially, if there were none effective control measures adopted.

NO$_X$ Emission Control for Coal-Fired Power Plants in China. Compared with some western developed countries such as Japan, Germany, and U.S.A., NO$_X$ emission control from coal-fired power plants in China is still very backward, though much stricter NO$_X$ concentration limits have been regulated in the newly revised Emission standard of air pollutants for thermal power plants, and have been put into effect since Jan. 1, 2004. However, even for the

newly commissioned boiler, the emission ceiling (450mg/m^3) was regulated based on the present performance of low NO$_X$ combustion technology.

Table 1. Coal-fired power plants NO$_X$ emission by province, Mt

Province	2000	2002	Province	2000	2002
Beijing	6.34	6.51	Hubei	11.93	15.17
Tianjin	8.29	9.36	Hunan	8.06	9.88
Hebei	36.69	44.66	Guangdong	31.08	44.15
Shanxi	27.57	36.93	Guangxi	5.06	6.30
Inner Mongolia	26.44	28.64	Hainan	1.03	1.10
Liaoning	29.66	32.37	Chongqing	6.02	17.47
Jilin	14.50	17.22	Sichuan	11.33	12.97
Heilongjiang	22.35	22.87	Guizhou	10.43	10.24
Shanghai	19.05	22.60	Yunnan	6.89	14.24
Jiangsu	41.30	50.33	Xizang	0.00	0.00
Zhejiang	21.80	27.02	Shaanxi	11.84	14.24
Anhui	14.63	17.92	Gansu	6.93	10.27
Fujian	8.16	11.95	Qinghai	1.48	2.47
Jiangxi	8.42	9.44	Ningxia	5.53	4.26
Shandong	41.50	47.74	Xinjiang	7.19	13.01
Henan	31.81	41.66	**Sum**	**483.30**	**603.00**

At present, there were only about 10% of utility boilers adopted different types of low NO$_X$ combustion system, and some of them could not achieved the anticipated reduction effects for different reasons.

By now, SCR process is only demonstrated technology that can achieve over 90% NO$_X$ reduction efficiency in reality. However, there were only one company with 6×600MW new built coal-fired generating units installed advanced SCR system to control NO$_X$ emissions. There were still no domestic enterprises having grasped all the key techniques of SCR installations. Therefore, SCR demonstration projects for several typical utility boilers firing coal with different characteristics should be initiated firstly in some large cities such as Beijing, Shanghai, etc. Not only it will benefit for local air quality improvement, also it will accelerate the commercialized step of domestic SCR technology for the spread application in the future.

Conclusions

By now, large amounts of NO$_X$ have been discharged from coal-fired power plants owing to the coal-dominated energy and power mix, as well as the relatively far rigorous emission regulations and policies in China. Further, if none effective comprehensive measures were adopted, NO$_X$ emissions and the related pollution will be worsened with the rapid growth of coal use for utility boilers burning in the future. Therefore, it is time for China to initiate several SCR and/or SNCR demonstration projects in coal-fired power plants for the widespread applications in the future.

References
(1) Kurvits, T.; Marta, T. *Environ. Pollut.* **1998**, 102 (S1), 187.
(2) State Environmental Protection Administration (SEPA). Report on the State of the Environment in China 2003. *http://www.sepa.gov.cn/eic/ 6493683031893606040/index.shtml*, **2004**. 6
(3) Hao J.M., Tian H.Z. *Enviorn. Sci. & Tehnol.* **2002**, 36(4): 552
(4) Tian H.Z. Present and future emissions of NOX and its comprehensive control policies in Chin *Ph.D. thesis*. Tsinghua University, **2003**.7
(5) NBS, and NDRC. China Energy Statistical Yearbook (2000~2002). *China Statistics Press*. **2004**.

COMBUSTION BEHAVIOR OF CHICKEN-LITTER COAL BLENDS

Nathan R. Whitely, Riko Ozao, Chi-Hui Wu, Daniel Chen, and Wei-Ping Pan

Thermal Analysis Laboratory
Institute for Combustion Science and Environmental Technology
Department of Chemistry
Western Kentucky University
2355 Nashville Road
Bowling Green, KY 42103

Introduction

Over eight billion broiler chickens are produced every year within the United States generating copious amounts of litter that must be disposed of properly[1]. Typically chicken litter is primarily used as a fertilizer on agricultural land due to its relatively high nitrogen and phosphorous content; however, poor spreading practices and over usage has been shown to have adverse effects on the ecology of the environment[2]. In the process of eutrophication, excess phosphorous can leach into the surrounding water system causing large algal blooms, which ultimately leads to depletions of the oxygen content in the water[3,4].

With outbreaks of *Pfiesteria piscicida* in Mid-Atlantic U. S. waterways and reports on the Dead Zone in the Gulf of Mexico becoming more prominent, the EPA have begun to limit and monitor the spreading of chicken litter on agricultural land based on the soil types, climate, and proximity to bodies of water[5,6]. The limitation placed on chicken litter usage and the large amount of chicken litter produced annually will necessitate alternate modes of disposal.

One such candidate is the cofiring of chicken litter with coal[7-9]. Chicken litter's calorific value (on the order of 5,000 BTU/lb) is equivalent to low rank coals. However, as with all blends much research must be completed to ensure the cofiring agents do not pose harmful environmental effects. The goal of this research is evaluate the evolved gas emissions from the combustion and pyrolysis of chicken litter and chicken litter-coal blends using thermogravimetric-mass spectrometry (TG-MS), thermogravimetric-Fourier transform infrared (TG-FTIR), and pyrolysis gas chromatography/mass spectroscopy (GC/MS).

Experimental

Chicken Litter Collection and Preparation. Approximately 9.5 kg of chicken litter were collected from a local commercial farm. The sample was divided into metal trays and air-dried at 30ºC for twenty-four hours. After air-drying, the sample was milled using a Retsch SM1 rotary cutting mill. The complete chicken waste sample was passed through a 12.5 mm screen to break down large aggregates of manure, followed by another pass through the mill using a 4.0 mm screen. The milling process served to homogenize the sample such that repeatability within subsequent testing would be of high confidence. To further homogenize the sample, the milled chicken waste sample was divided in half using a hand riffle. When the entire sample was divided in half using the riffle until the remaining sample filled a 64 oz. Bottle. Although the milling and riffling processes decreased the gross heterogeneous nature of the sample, some minor heterogeneity remained with regards to particle size. The sample was then divided according to particular size using –140 and –325 mesh sieves.

TG-MS. Approximately 10 mg litter samples were analyzed by a TA Instruments 2960 SDT interfaced to a Fisions VG Thermolab Mass Spectrometer by means of a heated capillary transfer line. The capillary transfer line was heated to 120ºC, and the inlet port on the mass spectrometer was heated to 150ºC. The Fisions unit is based on quadrupole design with a 1-150 amu mass range operating at a pressure of 1 X10^{-6} torr. The sample gas from the interface was ionized at 70 eV. Ultra high purity nitrogen and air at flow rates of 50 mL/min provided the respective pyrolysis and combustion atmospheres. Thirty-minute purges preceded the heating programs at which the samples were heated from room temperature to 1000ºC at a rate of 20ºC/min. The MS continually samples the purge gas generating temperature (or time) resolved MS spectrum for each of the individual m/z of 1-150.

TG-FTIR. The litter samples were analyzed by a Dupont 951 TGA interfaced to a Perkin Elmer 1600 series FTIR with a permanent one-inch silicon transfer line. Approximately 25 mg litter samples in ceramic boats were heated from room temperature to 1000ºC at heating rate of 20ºC/min the TGA. Ultra high purity nitrogen and air at flow rates of 100 mL/min provided the respective pyrolysis and combustion atmospheres. The purge gas carries the decomposition products from the TGA through an 80 mL-sample cell with KBr crystal windows. The cell was placed in the FTIR scanning path for detection of the decomposition products. Wrapping the IR cell in heat tape held at 150ºC and the increased flow rate are required to prevent condensation of evolved products. The FTIR scans the frequency range of 4500-450 cm^{-1} every 25 seconds providing temperature (or time) resolved FTIR spectrum.

Pyrolysis GC/MS. The samples were analyzed on a Pegasus II GC/MS system, which has a Time-of-Flight Mass Spectrometer and High Speed Gas Chromatography. The carrier gas flows through the sample holder of the Thermex system and through a cryogenic trap before entering the inlet port of the GC. The Thermex system heated the sample to 200°C at a rate of 50°C/min and held isothermally for one minute. During the heating segment the evolved gases are captured by the cryogenic focusing system at -100°C, while the GC is held idle. At the end of the thermal method the cryogen trap is heated rapidly to 300°C flashing the gases into the GC/MS system for analysis.

Results and Discussion

The primary chicken litter samples that were investigated were the sample possessing greater than –140 mesh particles and the sample possessing less than –325 mesh. From visual inspection, the large particles appear to be primarily composed of wood materials whereas the small particles appear to be primarily composed of mineral matter. Elemental analysis performed on the litter samples according to ASTM methods D4326 and D6349 are shown in Table 1.

Table 1. Elemental Analysis

Sample	Percent in Chicken Waste					
	SiO$_2$	Al$_2$O$_3$	Fe$_2$O$_3$	CaO	Na$_2$O	TiO$_2$
A	7.23	1.02	0.44	4.29	1.73	0.03
C	31.29	3.64	1.26	3.49	1.22	0.33

The increased SiO$_2$, Al$_2$O$_3$, Fe$_2$O$_3$, and TiO$_2$ contents for smaller particle size indicates that that the small particles within the chicken litter is indeed primarily composed of soil matter. Conversely, the Na$_2$O and CaO are lower in the small particle sample suggesting that the Na and Ca originate from minerals excreted from the chickens or from nutrients taken up by plants from the wood material. Table 2 shows the calorific value for the chicken litter samples.

Table 2. Calorific Value

Sample	BTU/lb
Mill	5166
LARGE	5299
SMALL	2915

The calorific value for the chicken litters is shown in Table 2. The mill sample represents the chicken litter that went through the sample preparation process, but was not divided by particle size (i.e. containing all particle sizes). The large particles have the highest calorific value because it contains the less mineral matter than the other samples; thus, the sieving process acts a physical means to decrease the mineral content of the chicken litter making the process analogous to the chemical washing of coal. Figure 1 shows the TGA curves of the samples for combustion.
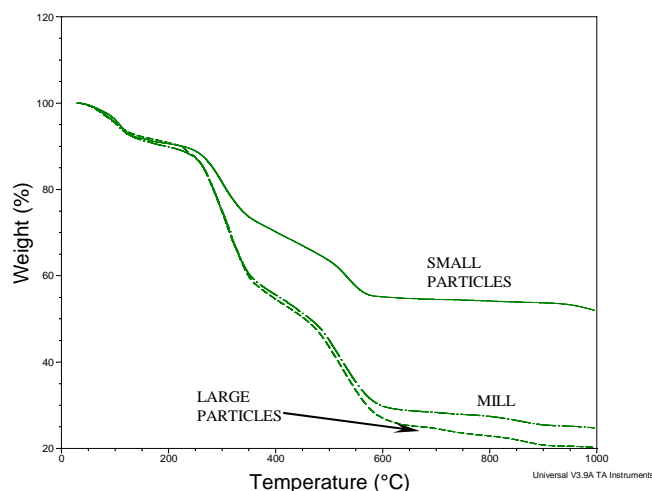
Figure 1. The TGA curve for combustion for the chicken litter samples.

The chicken litter decomposes in a four-step process. Most likely the initial weight loss is a factor of absorbed water and other low boiling compounds. The second and third are related to devolatilization and combustion, respectively. The fourth weight loss occurring at temperatures in excess of 700°C were initially attributed to decomposition of mineral matter. Figure 1 shows that the particle sizes behave similarly with respect to decomposition undergoing similar reactions; however, the amount of each component varies from particle size to particle size. Figure 2 shows data collected from the TG-FTIR experiment on the large particle samples. In Figure 2, specific frequencies of 965, 2359, and 3016 cm^{-1} were monitored as a functions of temperature to relate to ammonia, carbon dioxide, and methane emissions, respectively, for the large particle sample.
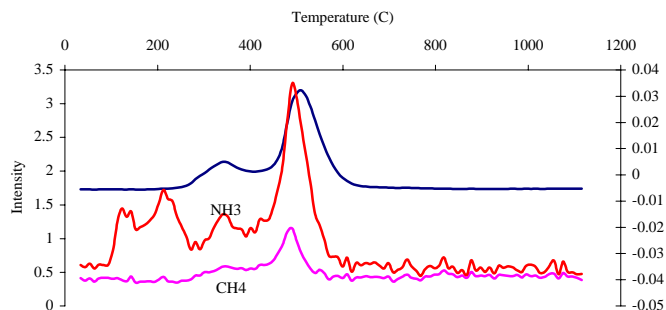
Figure 2. Carbon dioxide, ammonia, and methane emissions for large particles monitored by TG-FTIR.

The FTIR results support the earlier inferences about the mechanisms by which the chicken litter decomposes. The carbon dioxide emissions occur simultaneous to the second and third weight losses. The larger intensity of carbon dioxide emission relates to the third weight loss step in which the combustion of the organic matrix of the litter occurs. Co-evolving with the carbon dioxide is methane, but a much lower intensity. The ammonia evolution is much more complex having at least four different regions of evolution with the first two occurring below 200°C.

Figure 3 shows the TG-MS experiments of the large particle sample. The following m/z values of 18, 32, and 44 were used to monitor the relative concentrations of water, oxygen, and carbon dioxide respectively.
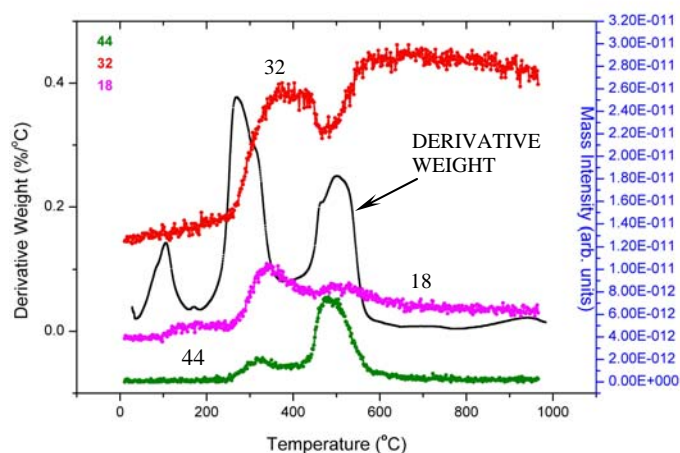
Figure 3. Deriv. weight loss curve and carbon dioxide, oxygen, and water emissions monitored by MS for large particles.

The MS provides better information relating to water evolution, because the complex FTIR signals make water difficult to monitor with good precisions. MS is useful at monitoring dominant combustion and oxidation reactions, because a decrease in the oxygen content can be noted as in Figure 3. Figure 4 shows the profile of the carbon dioxide evolution as measured by TG-MS for the small particle samples.
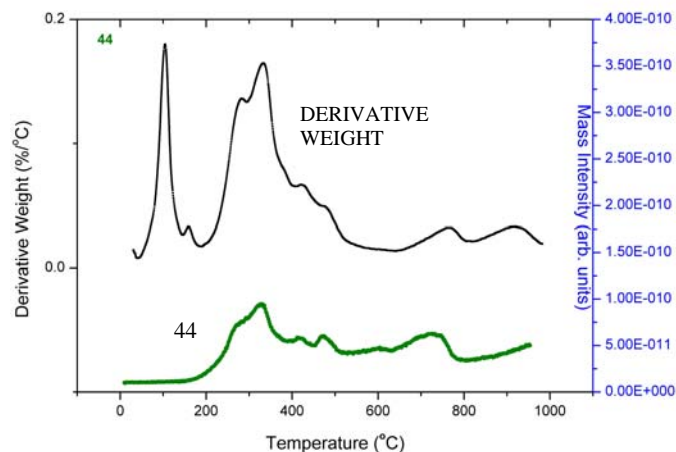
Figure 4. Carbon dioxide emissions monitored by MS for small particle sample.

Better conclusions about the proposed demineralization occurring above 700°C can be drawn from the small particle sample because of the much more significant mineral composition indicated from the elemental analysis. The subtle increase in the m/z 44 intensity indicates that indeed minerals decompose at elevated temperature; however, the lack of a single, predominant peak indicates the mineral composition of the chicken litter is very complex.

Because complete combustion does not solely exist in industrial power plants, studying pyrolysis is important. Initial TG-FTIR and TG-MS experiments under pyrolysis conditions proved to be too complex for a completely accurate description about pyrolysis mechanism to be formed. Therefore, pyrolysis GC/MS was chosen as a better analytical technique. The advantage of pyrolysis GC/MS is that complex decompositions involving multiple, simultaneous evolutions can be separated by the GC. Table 3 shows the compounds identified by a NIST library.

Table 3. Evolved Gases from Pyrolysis GC/MS identified by NIST Library for Large Particles

Carboxylic acids	Heterocyclic	Benzene derivatives	Amines	Phenols
acetic acid	furfural	methylated benzaldehyde	N-butyl tert butylamine	2-methyl phenol
3-methyl butanoic acid	2-furanmethanol	benzene acetic acid	--------------	dimethylated phenols
hexanoic acid	indole	dibutyl phthalate	--------------	2,4,6 trimethyl phenol
Carbamic acid	-----------------	--------------	--------------	2-methoxy-4-vinyl-phenol
Amides	**Organic acid**	**Sulfides**	**Fatty acids**	**Steroids**
acetamide	phosphonic acid	dimethyl sulfone	propanoic acid ester	cholesterol derivative

The phenol and benzene derivatives most likely are related to the decomposition of lignin the highly cross-linked phenolic structure that accounts for the stiffness in wood. Lignin can account for 25% of the mass in wood and is composed primarily is composed of monomers with ortho methoxy and para propene groups with respect

to the hydroxyl group of the phenol. As this matrix begins to decompose, similar fragments to the monomers would be expected to evolve. The cholesterol derivatives and other steroids are related to the steroids excreted by the chickens. The bedding material absorbs the fecal matter of the chickens, which contain a complex set of cholesterol derivatives and other related steroids that are generated from the metabolic actions of anaerobic bacteria present in the digestive tract of some animals. The carboxylic acids and heterocyclic compounds may stem from the decomposition from the complex network of polysaccharides present in wood material, especially cellulose and hemicellulose. The polymeric structure of polysaccharides consists of simple sugar molecules in cyclic conformations acting as monomers. Hydroxyl groups of the sugar molecules are highly substituted by acetal groups, which may be released as acetic acid upon decomposition. The highly complex network of cyclic heterocyclic compounds is most likely responsible for the evolution of the heterocyclic compounds.

Conclusions

From proximate and ultimate analysis chicken litter was shown to be a feasible material for cofiring with coal; however, the decomposition upon combustion is more complex for chicken litter occurring in four decomposition stages. From evolved gas analysis, the initial weight loss stage was related to the evolution of absorbed water and ammonia. The second and third steps are characteristic of pyrolysis and devolatilization followed by combustion as identified by the relative evolutions of carbon dioxide and decrease in oxygen content. The final decomposition occurring at temperatures above 700°C and losing less than 6% are related to decomposition of the mineral matter.

References
(1) North, M. O. *Commercial Chicken Production Manual, 4th Edition*. AVI Publishing Inc.: Westport, CT, 1990; pp. 692.
(2) Kofinas, P.; Kiousis, D. R. *Environ. Sci. Technol.* **2003**, 37(2), 423-427.
(3) Peak, D.; Sims, J. T.; Sparks, D. L. *Environ. Sci. Technol.* **2002**, 36(20), 4253-4261.
(4) Scanes, C. G.; Brant, G.; Ensminger, M. E. *Poultry Science, 4th Edition*. Pearson Education Inc.: Upper Sddle River, NJ, 2004.
(5) Burkholder, J.; Glasgow, H. B. *Limnol. Oceanogr.* **1997**, 42, 1052-1057.
(6) Boesch D. F. *Science*. **2004**, 306(5698), 977-978
(7) Kelleher, B. P.; Leahy, J. J.; Henihan, A. M.; O'Dwyer, T. F.; Sutton, D.; Leahy, M. J. *Bioresour. Technol.* **2002**, 83, 27-36.
(8) Abelha, P.; Gulyurtlu, I.; Boavida, D.; Seabra Barros, J.; Cabrita, I.; Leahy, J. Kelleher, B.; Leahy, M. *Fuel* **2003**, 82, 687-692.
(9) Davalos, J. Z.; Roux, M. V.; Jimenez, P. *Thermochim. Acta* **2002**, 394, 261-266.

EXPERIMENTAL STUDY ON EFFECT OF INHIBITORS ON OXIDATION KINETICS OF CALCIUM SULFITE UNDER HETEROGENEOUS CONDITION

Yi Zhao [1], Lidong Wang [1], Xiaoming Wang [2], Qiangwei Li [1], Peiyao Xu[1]*

[1]School of Environmental Science & Engineering, North China Electric Power University, Baoding, Hebei, P.R.China, 071003
[2]State Power Environmental Protection Research Institute, Nanjing, P.R.China, 210031

Introduction

Desulfurization of flue gas is required in order to minimize the impact of the combustion of fossil fuels on the environment. Wet limestone scrubbing is the flue gas desulfurization (FGD) process, which has reached the widest diffusion. Oxidation is an important chemical course in the process. Calcium sulfite in slurry of the scrubber loop is oxidized into sulfate. Calcium sulfate will deposit when the oxidation ratio is from 15 to 95 percent and the utilization of calcium is lower than 80 percent [1]. Controlled oxidation, which includes both inhibited oxidation and forced oxidation, is done to make the oxidation ratio lower than 15 percent or higher than 95. Inhibited oxidation is conducted by adding inhibitors into the slurry, so that the concentration of sulfate is much lower than saturation and the small quantity of calcium sulfate deposits with the sulfite. Forced oxidation is conducted by way of injecting air and adding catalyst into the slurry, so that the oxidation reaction is thoroughly completed and there is enough gypsum breed for the crystal to develop.

Oxidation of sodium sulfite in aqueous systems has been studied extensively since Bäckström proposed a generally accepted chain propagation mechanism. Various reaction orders have been reported with respect to oxygen, sulfite and catalyst metal. However, few inhibitors have been specially studied which could have great effect on the oxidation rate. As the main by-product is calcium sulfite in wet limestone scrubbing, review of mechanism about inhibitors during the course of oxidation under heterogeneous conditions could be very significant in practice.

In the oxidation systems about sodium sulfite, the surface-active Teepol and silicon oil were found to have no effect on the reaction rate [2]. The electrolytes KCl and KCNS in concentration up to 2M have no influence on the value of the reaction rate, which, however, decreases reproducibly with increasing concentration of KI. Disagreement in values for the reaction order with respect to copper catalyst found by various authors may be explained in terms of catalytic action of Cu^{2+} ions and simultaneous inhibition by Cu^+ ions. Alcohols, phenols and hydroquinone were found to have great effect on the reaction rate [3]. Moreover, Fe^{3+} and Cr^{3+} could act as inhibitors in the course of reaction [4].

Uncatalyzed oxidation kinetics of calcium sulfite, produced by the 4th Reagent Company in Shanghai, was studied under heterogeneous conditions in this paper. Alcohols, phenols and hydroquinone were also selected as inhibitors to review the kinetics under inhibited conditions. Thus, the theory was provided for design of the controlled oxidation techniques.

Experimental

Experiment measure

(a) Oxidation experiment: 150 mL of distilled water was added into the reactor after the temperature, rotate speed and velocity of airflow were adjusted. Air was injected into the reactor after some quantity of inhibitors and calcium sulfite were added into the water.

Hydrochloric acid and ammonia were used to adjust the pH. As the solution was alkaline, a little acid was added continuously at the beginning of the reaction. The pH would become steady and decrease slowly after 2 min. The temperature, velocity of airflow and pH should be observed and adjusted to the scheduled value during the course of reaction. The production was dissolved by hydrochloric acid at the fixed time. The concentration of sulfate was measured and the initialization involved in the sulfite was taken out. The experimental apparatus was shown in Fig. 1.
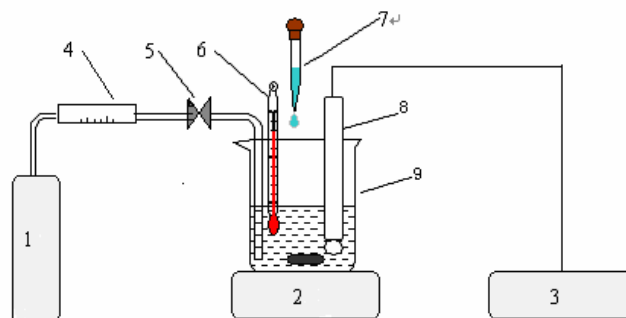

Figure 1. Experimental Apparatus: (1) YL90S-2 air compressor; (2) 79HW-1 magnetic constant temperature stirrer; (3) pHS-2C pH meter; (4) LZB glass rotameter; (5) gas valve; (6) thermometer; (7) HCl or NH_4OH; (8) combined pH electrode; (9) glass reactor.

(b) Analytical measure: The concentration of sulfate was measured by turbidimetric method [5]. Some quantitative liquor was diluted to 50 mL and stirred at a fixed speed and 2.5 mL of fixing reagent was added. Then 0.2 g of barium chloride griddled between 20 to 30 destination was added. The absorbency was measured at 420 nm wavelength by spectrophotometer (721 type) after the liquor was stirred for 1 min. Thus the concentration of sulfate would be achieved by the standard curve measured by the same method. The observed oxidation rate would be calculated by the formula [6]:

$$R = \frac{C_t - C_0}{t}$$
(1)

(c) Reagents: All used were analytical reagents, as follows:
Fixing reagent: the liquor, which involved 75 g of sodium chloride, 300 mL of distilled water, 30 mL of hydrochloride acid, 50 mL of glycerol and 100 millimeter of alcohols, was blended uniformly.
Standard sulfate solution: the liquor, which involved 1.4787 g of anhydrous sodium sulfate, was diluted to 1,000 mL by distilled water.
Other reagents: hydrochloride acid, ammonia, barium chloride, phenols (concentration of 6.07 %), alcohols, hydroquinone.

Results

(a) Influence of pH: After 1 gram of calcium sulfite was added into 150 millimeter of distil water, some quantity of inhibitors, such as 1 gram of alcohols, 5 millimeter of phenols solution and 1 gram of hydroquinone, was added respectively. The temperature was kept to 30℃ and the velocity of airflow was kept to 0.056 m³/h. Oxidation lasted 30 minutes under different pH conditions. Influence of pH on the observed oxidation rate was shown in Fig. 2.

(b) Effect of concentration of calcium sulfite: After different quantity of calcium sulfite was added into 150 millimeter of distil water, some quantity of inhibitors, such as 1 gram of alcohols, 5 millimeter of phenols solution and 1 gram of hydroquinone, was added respectively. The temperature was kept to 30℃ and the velocity of airflow was kept to 0.056 m³/h. PH was kept to 6.0 and

oxidation lasted 30 minutes. Influence of concentration of calcium sulfite on the observed oxidation rate was shown in Fig. 3.
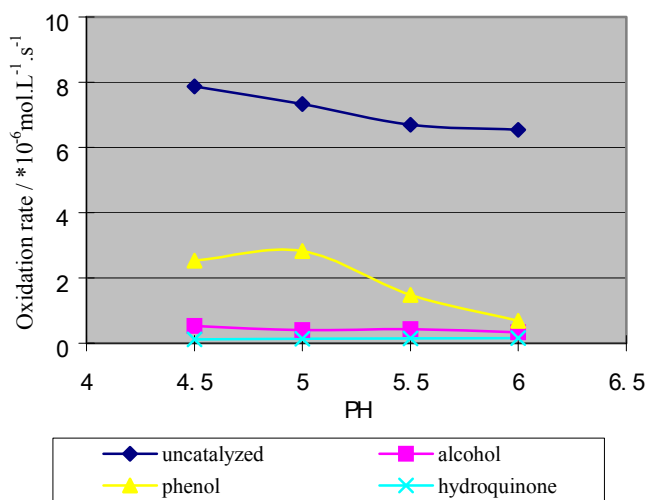

Figure 2. Effect of pH on the observed oxidation rate
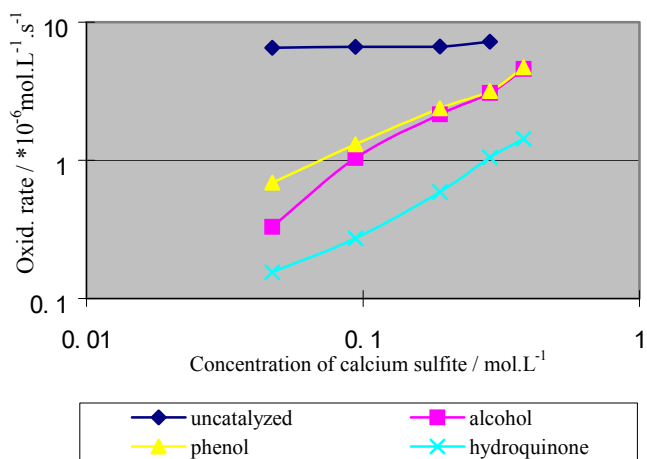

Figure 3. Effect of concentration of calcium sulfite on the observed oxidation rate

(c) Effect of oxygen partial pressure: After 1 g of calcium sulfite was added into 150 mL of distilled water, some quantities of inhibitors, such as 1 g of alcohols, 5 mL of phenols solution and 1 g of hydroquinone, were added, respectively. The temperature was kept to 30°C and pH was kept to 6.0. Oxidation lasted 30 min under different velocity of airflow conditions. As the concentration of oxygen was invariant in the air, velocity of airflow was in proportion to oxygen partial pressure in the definite time. Influence of oxygen partial pressure on the observed oxidation rate was shown equivalently in Fig. 4.

(d) Effect of concentration of inhibitors: After 1 g of calcium sulfite was added into 150 mL of distilled water, different quantities of inhibitors were added. The temperature was kept to 30°C and the velocity of airflow was kept to 0.056 m³/h. pH was kept to 6.0 and oxidation lasted 30 min. Influence of concentration of inhibitors on the observed oxidation rate was shown in Figs. 5-1, 5-2 and 5-3.

Discussion

(a) The uncatalyzed oxidation rate of calcium sulfite would decrease with the increase of pH. Although the influence of pH was not significant, the tendency would not change after adding the three kinds of inhibitors. The inhibitory influence of phenols would decrease evidently with the decrease of pH, while it was not evident with regard to alcohols and hydroquinone.
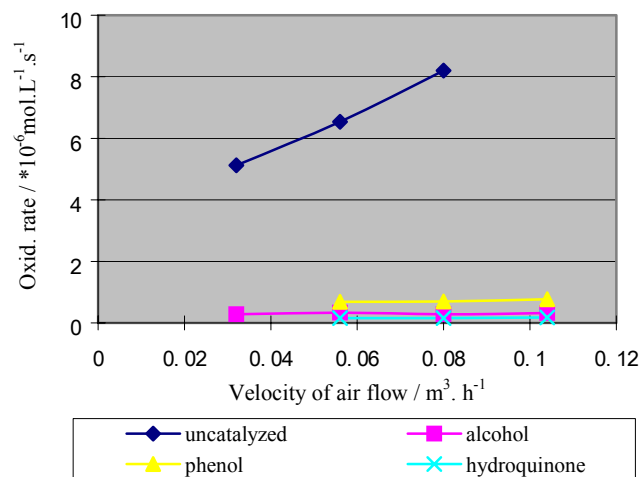

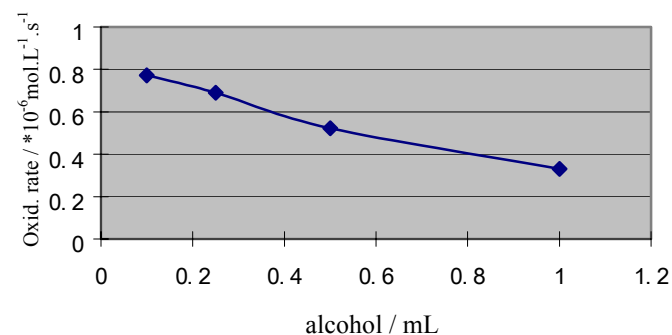**Figure 4.** Effect of oxygen partial pressure on the observed oxidation rate

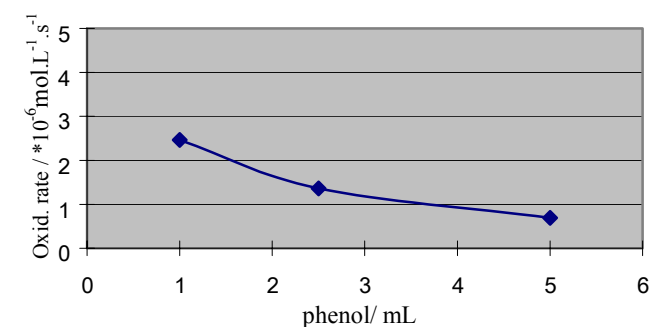**Figure 5-1.** Effect of concentration of alcohol

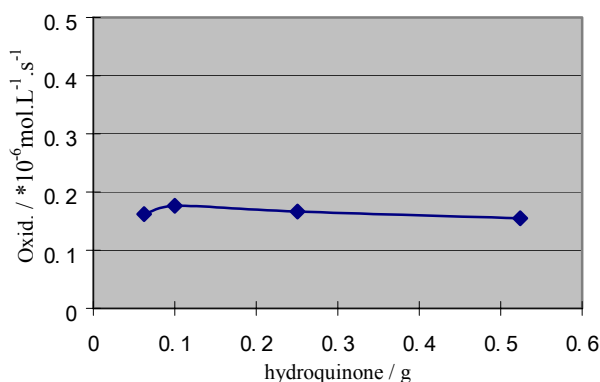**Figure 5-2**. Effect of concentration of phenol

Figure 5-3. Effect of concentration of hydroquinone

(b) The concentration of sulfite was relatively high which was close to the practical condition. Uncatalyzed oxidation rate was zero order in calcium sulfite, which was consistent with that from Klaus Hjuler and Kim Dam-Johansen [4]. Moreover, the oxidation rate would increase with the increase of concentration of calcium sulfite after added in the three kinds of inhibitors.

(c) Uncatalyzed oxidation rate was 0.5 order in the oxygen partial pressure. The oxidation rate would turn to zero order in oxygen partial pressure after added in the three kinds of inhibitors.

(d) The oxidation rate would decrease with the increase of concentration of alcohols and phenols during the experiments, in which the concentration of alcohols varying from 0.667 to 6.67 mL/L and phenols varying from 0.405 to 2.02 g/L. It was not significant for the decrease of oxidation rate with increasing of hydroquinone during the experiments, in which the concentration of hydroquinone varying from 0.416 to 3.49 g/L.

(e) The oxidation rate would increase with the increase of temperature in all the experiments, which was significant while uncatalyzed or inhibitoried by phenols and insignificant while inhibitoried by alcohols or hydroquinone.

(f) The influence of EDTA studied with the same measures as well. It was found to have no effect on the uncatalyzed oxidation rate of calcium sulfite.

Mechanism

The oxidation process of calcium sulfite could be divided into three steps under heterogeneous conditions, which included dissolution of calcium sulfite whose rate was R_B from the solid particles to the liquid, mass transfer of oxygen into the liquid whose rate was R_B and the chemical reaction whose rate was R_C in the liquid phase.

Dissolution rate R_A of calcium sulfite:

The reaction was as follows at low pH:

$$H^+ + CaSO_3 \Leftrightarrow Ca^{2+} + HSO_3^- \qquad (2)$$
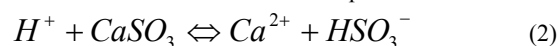
For the particles whose diameter was r_j, the dissolution rate was given by the equation assuming it to follow the shrinking-core model [7]:

$$N_A = -4\pi r^2 D \frac{dC}{dr} \qquad (3)$$

boundary conditions: $C = C_S$ while $r=r_j$

$C = C_B$ while $r=+\infty$

It was inferred from above

$$N_A = 4\pi r_j D(C_S - C_B) \qquad (4)$$

Because of the reaction of (2), D was increased and (4) was modified

$$N_A = 4\pi r_j \varepsilon D(C_S - C_B) \qquad (5)$$

The dissolution rate included dissolution of all different size of calcium sulfite

$$R_A = \sum M N_A$$

Mass transfer rate R_B of oxygen:

As the oxidation process was irreversible, the kinetic equation was given by:

$$R_c = k[O_2]^m [SO_3^{2-}]^n \qquad (7)$$

The diffusion and chemical reaction were simultaneous while oxygen was absorbed into the liquid. Thus the sub-coefficient was increased and the mass transfer coefficient was changed accordingly. The mass transfer rate of oxygen was given according to theory of double film

$$R_B = k_L^/(C_{Ai} - C_A) = k_L \alpha (C_{Ai} - C_A) \qquad (8)$$

$$\alpha = \frac{a}{tha} \qquad (9)$$

where a was fit by the relation

$$a = L\sqrt{(1 - \frac{\alpha - 1}{U})^n}$$

where L and U were decided [8] by

$$L = \frac{1}{k_L} \sqrt{\frac{2}{m+1} D_A k C_{Ai}^{m-1} C_B^n}$$

$$U = \frac{C_B}{2C_{Ai}} \cdot \frac{D_B}{D_A}$$

As the chemical reaction was rapid, it was simplified by considering $\alpha \approx L$

$$k_L^/ = \alpha \cdot k_L \approx L k_L = \sqrt{\frac{2}{m+1} D_A k C_{Ai}^{m-1} C_B^n} \qquad (10)$$

$$R_B = k_L^/(C_{Ai} - C_A) = \sqrt{\frac{2}{m+1} D_A k C_{Ai}^{m-1} C_B^n} \cdot (C_{Ai} - C_A) \qquad (11)$$

The concentration of oxygen measured in the reaction system was approximately zero

$$R_B = \sqrt{\frac{2}{m+1} D_A k C_{Ai}^{m-1} C_B^n} \cdot C_{Ai}$$

$$= \sqrt{\frac{2}{m+1} D_A k C_{Ai}^{m+1} C_B^n}$$

$$= \sqrt{\frac{2}{m+1} D_A k (\frac{P}{m_{pc}})^{m+1} C_B^n} \qquad (12)$$

It was inferred from equation (12) that the mass transfer rate was 0.5 order in oxygen partial pressure while the chemical reaction rate was zero order in dissolved oxygen.

Chemical reaction rate R_C:

It was inferred from the chain reaction mechanism proposed by Bāckstrōm [9]:

$$R_C = kC_M^{1/2}C_{S(IV)}^{3/2} \qquad (13)$$

It was shown that the chemical reaction rate was zero order in dissolved oxygen and 3/2 order in sulfite.
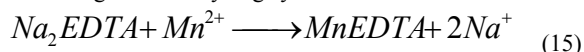
General reaction rate R:

As the three above steps proceed simultaneously, the general reaction rate depended on the slowest step:

$$R = \min(R_A, R_B, R_C)$$

The characteristics of uncatalyzed oxidation of calcium sulfite in the experimental system were as follows:

- Uncatalyzed oxidation rate was 0.5 order in oxygen partial pressure, which showed $R = R_B$. As calcium sulfite was saturated in the reaction solution and concentration of sulfite ion could be regarded as constant, the general reaction rate was 0 order in calcium sulfite. It was inferred that the general reaction be controlled by mass transfer of oxygen.
- The dissolution rate increased which would lead to the increase of sulfite ion with the decrease of pH. Thus the mass transfer rate would increase according to equation (12), which was in agreement with the increasing of general reaction rate while pH decreased.
- The chemical reaction rate R_C increased which would lead to the increase of k in equation (12) while the temperature increased. The general reaction would increase accordingly.
- Inhibitors could have effect on the oxidation of calcium sulfite by the following means:
  (1) Inhibitors could react with catalyst, such as cobalt and manganese, and restrained their catalysis by forming steady compound. For example, EDTA would restrain the oxidation of calcium sulfite by forming chelate complex in the manganese catalyzing system.

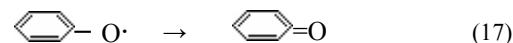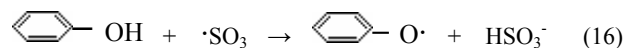$$Na_2EDTA + Mn^{2+} \longrightarrow MnEDTA + 2Na^+ \qquad (15)$$

  As calcium sulfite used in the experiments was analytical reagent in which there was no catalyst impurity such as transition metals, EDTA had no effect on reaction rate.
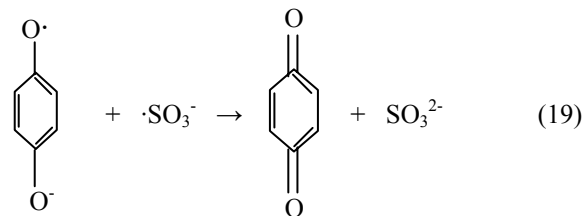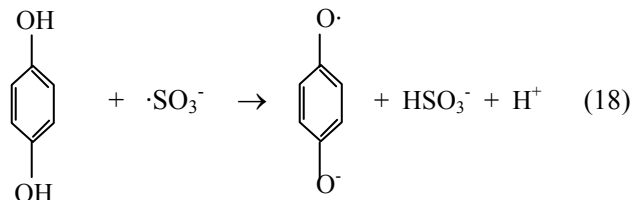 (2) Inhibitors could have effect on the oxidation rate by reducibility. For example, as a kind of effective reductant, hydroquinone competed for the dissolved oxygen with sulfite, which would inhibit the oxidation. It was shown in Fig.5-3 that there were about 1.74×10^{-3}mol of sulfite oxidated during the 30 minutes' uncatalyzed reaction. That was to say, there was at least 8.7×10^{-4}mol of oxygen dissolving and reacting as oxidant. While after about 0.06g of hydroquinone was added under the condition, there were 4.4×10^{-5}mol of sulfite oxidated. Supposing hydroquinone inhibited the oxidation by competing for dissolved oxygen, there should be 8.5×10^{-4}mol of oxygen reacting with hydroquinone which was much more than what could react. Therefore, reducibility of hydroquinone was not the primary factor that inhibited the oxidation in the experimental system. It was the same with alcohols, phenols.
  (3) As the chain terminator, inhibitors could inhibit the oxidation by eliminating the free radicals produced in the process of reaction. For example, alcohols reacted with

$\cdot SO_3^-$ which would terminate the chain reaction. There were many inhibitors such as hydroquinone, phenols, alcohols and glycerol, which had active hydroxide radicals and reducibility. The process was as follows.

(i) phenols:

$$(16)$$

$$(17)$$

(ii) hydroquinone:

$$(18)$$

$$(19)$$

(iii) alcohols:

$$CH_3CH_2OH + \cdot SO_3^- \rightarrow CH_3CH_2O\cdot + HSO_3^- \qquad (20)$$

$$CH_3CH_2O\cdot + \cdot SO_3^- \rightarrow CH_3CHO + HSO_3^- \qquad (21)$$

Uncatalyzed oxidation kinetics of calcium sulfite under heterogeneous condition was changed when the three above inhibitors added and the characteristics given.

- Free radicals $\cdot SO_3^-$ were mostly absorbed and chemical reaction rate R_C decreased greatly. Equation (13) was not applicable any longer and the general reaction was controlled by the chemical reaction.
- Mass transfer rate of oxygen R_B decreased and was much greater than chemical reaction rate. The chemical reaction had little effect on oxygen absorbing which was approximate physical absorbing process. As the rate of oxygen consumed by reaction was rather little, oxygen in the solution was saturated during the reaction. Thus the concentration of oxygen was regarded as constant and the general reaction was zero order in oxygen partial pressure.
- Besides absorbing free radicals, the definite inhibitors could compete for dissolved oxygen only with some quantitative calcium sulfite. Thus the influence of inhibitors would be weakened and the general reaction rate would increase while calcium sulfite in the solution increased, which explained the general reaction rate decreased along with the increase of inhibitors.
- The equilibrium would move to the right in equation (2) and the concentration of dissolved calcium sulfite would increase while pH decreased, which led to increase of the general reaction rate.

- The chemical reaction rate would increase when the temperature increased. However, the reaction was not free radical reaction and the general reaction rate increased indistinctively.

Conclusions

In the experimental system, uncatalyzed oxidation rate was zero order in concentration of calcium sulfite and 0.5 order in oxygen partial pressure. The kinetics would change after adding the inhibitors and the oxidation rate was 1 order in concentration of calcium sulfite and zero order in oxygen partial pressure. It was inferred by analyzing the mechanism that uncatalyzed oxidation was free chain reaction and the free radicals, which were only a little, could be produced without transition metals and UV in the experiments. Inhibitors, such as Alcohols, phenols and hydroquinone, could have effect on the reaction by eliminating the free radicals, which was different from the inhibitory mechanism of EDTA. These kinds of inhibitors, which had active hydroxide radicals and reducibility, might also include glycerol, tea polyphenols, ascorbic acid and other substances. Thus, the theory was provided for design of the controlling oxidation techniques.

Notation

α enhancing coefficient in liquid phase = $k^{/}_L/k_L$

C_A concentration of oxygen in the solution

C_{Ai} equilibrium concentration of oxygen at the interface

C_B concentration of calcium sulfite particles

C_M concentration of catalyst

C_S saturation concentration of calcium sulfite particles

$C_{S(IV)}$ concentration of sulfite ion

C_t concentration of calcium sulfate after reaction, mol·L^{-1}

C_0 initialization concentration of calcium sulfate, mol·L^{-1}

D mass transfer coefficient of calcium sulfite particles

D_A mass transfer coefficient of A in the liquid phase

D_B mass transfer coefficient of B in the liquid phase

L ratio of chemical reaction rate in the liquid film to diffusion rate through the liquid film about A in the double film model

M amount of calcium sulfite particles whose diameter was r_j in unit of solution

m chemical reaction order in dissolved oxygen

m_{PC} equilibrium constant at the interface

N_A dissolution rate of calcium sulfite for particles whose diameter was r_j

n chemical reaction order in sulfite

P oxygen partial pressure in gas phase

t reaction time, s

U ratio of diffusion rate about B (sulfite) to that about A through the liquid film

ε enhancing coefficient

References

[1] Yan Jian, "Controlling Oxidation in Wet Desulfurization", Electric Environment Protection, 13, pp 41-44, 1997 (in Chinese)

[2] V.Linek and V.Vacek, "Chemical Engineering Use of Catalyzed Sulfite Oxidation Kinetics for the Determination of Mass Transfer Characteristics of Gas-Liquid Contactors", Chem. Eng. Sci., 36, pp 1747-1768, 1981

[3] Amedeo Lancia, Dino Musmarra and Francesco Pepe, "Uncatalyzed Heterogeneous Oxidation of Calcium Bisulfite", Chem. Eng. Sci., 51, pp 3889-3896, 1996

[4] Klaus Hjuler and Kim Dam-Johansen, "Wet Oxidation of Residual Product from Spray Absorption of Sulphur Dioxide", Chem. Eng. Sci., 49, pp 4515-4521, 1994

[5] Method of Water Quality Analysis, ed. by Sanitary Institute of Chinese Medical Academy, Published in Demotic Sanitary Publishing Campany, pp 90-92, 1972 (in Chinese)

[6] Zhong Qin, "Study on Uncatalyzed Calcium Sulfite Oxidation Kinetics", Nanjing University of Science and Technology Transaction, 24, pp 172-176, 2000 (in Chinese)

[7] Hao Jiming, Wang Shuxiao and Lu Yongqi, Technical manual of controlling sulfur dioxide pollution on fuels, pp 213-214, 2001(in Chinese)

[8] Hao Jiming and Ma Guangda, Controlling engineering of air pollution, Published in Higher Education Publishing Campany, pp 303-305, 1990 (in Chinese)

[9] Charles H. Barron and Harold A. O'Hern, "Reaction Kinetics of Sodium Sulfite Oxidation by the Rapid-mixing Method. Chemical Engineering Science", Chem. Eng. Sci., 21, pp 397-404, 1966.

OVERALL PERFORMANCE AND ENERGY CONSUMPTION OF AMINE TREATING PLANT USING SPLIT-FLOW SCHEME FOR CO$_2$ CAPTURE FROM LOW-PRESSURE COMBUSTION FLUE GAS

Adisorn Aroonwilas

Faculty of Engineering, University of Regina
Regina, Saskatchewan, Canada S4S 0A2

Abstract

Capturing carbon dioxide (CO$_2$) from combustion flue gas streams has been identified as one of the key measures for the mitigations of greenhouse gases. At present, the chemical absorption using aqueous amines is the most reliable CO$_2$ capturing technology for the diluted low-pressure flue gas. However, this technology is associated with high capital and operating cost. One approach to reduce the cost is to modify the plant configuration so as to improve the efficiency of energy use. This work evaluates an overall performance and energy consumption of the amine treating plant using split-flow configuration. The evaluation was carried out using our mechanistic mass-transfer and hydrodynamic model. The model accounts for mechanism of liquid flow distribution, mass-transfer process with chemical reactions, and vapor-liquid equilibrium. The overall process performance is presented in terms of reboiler heat-duty for solvent regeneration, size of regenerator, and size of absorber.

Introduction

Capturing greenhouse gases (GHGs), particularly carbon dioxide (CO$_2$) from industrial gas streams is one of the key measures for the mitigation of GHG emissions. At present, capturing CO$_2$ from dilute low pressure gas streams by using chemical absorption is the most reliable mitigation technique that bears no technical risk. However, this technology is associated with high capital and operating cost (i.e. \$40 - \$80 per ton of CO$_2$ captured), despite the fact that it has been commonly used for decades in many industrial operations. The high cost of this process is primarily due to the excessive energy consumption for regenerating the absorption solvent. To make the CO$_2$ absorption process economically viable, the associated energy use must be substantially reduced.

Two approaches can be applied to reduce energy consumption in CO$_2$ absorption process. First is to use the absorption solvent that requires low energy to strip out CO$_2$, and second is to modify the conventional process configuration so as to improve the energy efficiency. The focus of this work is on the modification of process configuration.

Split Flow Configuration

A process configuration so called "Split flow of CO$_2$-riched solution" is of interest in this work since it has potential to reduce the associated latent and sensible heats required during solvent regeneration. The split flow configuration has been applied to several gas purification processes, including Shell tripotassium phosphate and hot potassium carbonate[1]. Its key feature (**Figure 1**) is a division of rich-solution from the absorber into two streams. The first stream enters the top of the regenerator, flows downward, leaves the regenerator from the midpoint and enters the absorber at the midpoint. The second stream enters the regenerator at the midpoint, flows downward, leaves the regenerator from the bottom, and eventually enters the absorber at the top.
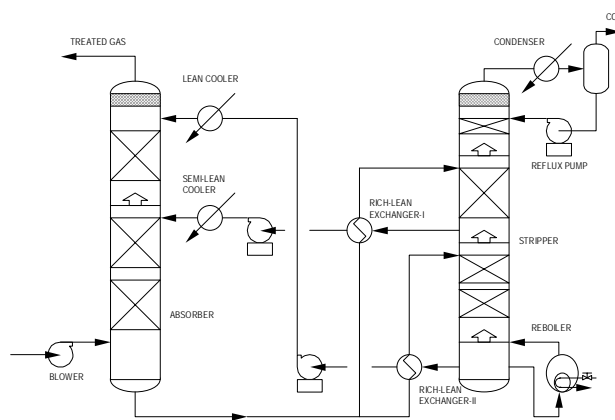

Figure 1. Split-flow process configuration.

Development of Rigorous Model

The split flow configuration was evaluated using the knowledge of mass-transfer and hydrodynamics obtained from our in-house mechanistic design model for gas absorption and regeneration. This model was developed and used for mass-transfer prediction in our previous work[2]. It was based on an integration of several sub-models including mechanism of liquid flow distribution, mass-transfer process with chemical reactions, and vapor-liquid equilibrium (VLE). The liquid distribution sub-model evaluated the distribution features of irrigating liquid, at different locations inside the packing element, during the operation of the absorption columns. The liquid distribution information was then used to calculate the interfacial area. The mass-transfer sub-model was associated with the use of two-film theory for evaluating the overall mass-transfer coefficient (K_G) across the gas/liquid boundary. To calculate the individual mass-transfer coefficient, the penetration theory was incorporated into this sub-model, together with the knowledge of absorption kinetics and the enhancement factor equation proposed by DeCoursey & Thring in 1989. The equilibrium behavior under absorption conditions was evaluated by using the electrolyte nonrandom two liquid (NRTL) model. The model simulation was based on the theoretical packed column design procedure for adiabatic gas absorption with chemical reaction, which accounted for heat of absorption, solvent evaporation and condensation, chemical reaction in liquid phase, and simultaneous heat- and mass-transfer processes. The simulation of the absorption column was achieved by dividing the packing height into a number of sections. Each of these sections was treated as a non-equilibrium (or rate-based) discrete stage, governed by material and energy equations. Details of the mathematical model and simulation can be found in Aroonwilas et al (2003)[2].

Process Simulation and Case Study

A case study was established to evaluate and compare the overall performance of CO$_2$ capture plant using both conventional and split flow configurations. The plant was designed for capturing 1,000 tonnes CO$_2$ per day with a capture efficiency of 95%. A 5 kmol/m^3 aqueous solution of monoethanolamine (MEA) was the absorption solvent. The CO$_2$ loadings of lean and rich solutions were 0.17-0.22 and 0.50 mol/mol, respectively. The reboiler temperature ranged from 110 to 120°C. The overall plant performance is presented in terms of 1) reboiler heat-duty for solvent regeneration, 2) size of regenerator, and 3) size of absorber.

The simulation results show that the split-flow scheme leads to a reduction in reboiler heat-duty. From **Table 1**, the MEA plant using

conventional configuration requires heat-duty ranging from 78,000 to 144,000 Btu/lb mol CO_2 depending upon operating conditions, while the plant using split-flow scheme can be operated at the heat-duty of as low as 55,000 Btu/lb mol CO_2. The reduction in heat-duty can be explained by the McCabe-Thiele diagram. As seen from **Figure 2**, the operating line of the conventional configuration is far apart from the equilibrium line, indicating an unnecessary excess of heat-duty or water vapor produced in reboiler. On the contrary, the operating line of the split flow scheme is located close to the equilibrium line, indicating a small excess of heat-duty for a given CO_2 stripping target.

Table 1. Simulation results.

Process	Relative absorber size	Relative NTU_{Regen}	Reboiler heat duty (Btu/lb-mole CO_2)
Typical process (Case I: $\alpha_{CO2, Lean}$ = 0.17 mol/mol, $Temp_{reboiler}$ = 110°C)	1.00	1.0	144,000
Split-flow process			
• (Operation I-CI)	1.05	4.2	55,000
• (Operation II-CI)	1.01	3.4	59,000
• (Operation III-CI)	0.99	2.0	67,000
Typical process (Case II: $\alpha_{CO2, Lean}$ = 0.22 mol/mol, $Temp_{reboiler}$ = 110°C)	1.00	1.0	83,000
Split-flow process			
• (Operation I-CII)	0.73	3.0	68,000
• (Operation II-CII)	1.09	2.0	69,000
Typical process (Case III: $\alpha_{CO2, Lean}$ = 0.17 mol/mol, $Temp_{reboiler}$ = 120°C)	1.00	1.0	78,000
Split-flow process (Operation I-CIII)	1.01	1.9	64,000
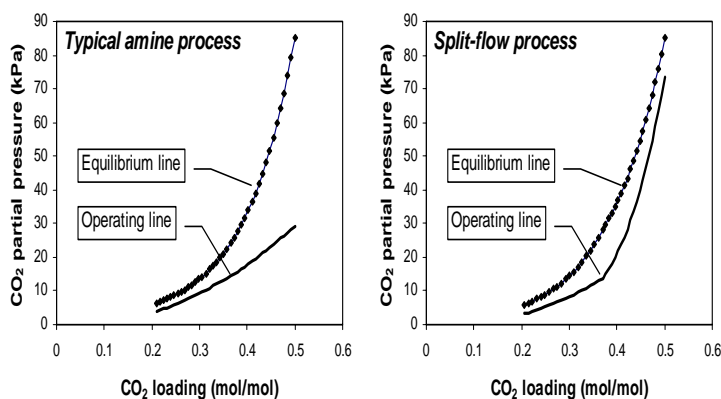
It is worthwhile to note that while reducing the reboiler heat-duty, the split-flow scheme requires a taller regenerator. This indicates a trade-off feature between the energy cost for solvent regeneration and the capital investment cost of regenerator. From the simulation, a specific number of transfer unit (NTU) representing the height of regenerator can be increased to as high as a factor of 4.

In addition to the regenerator height, the effect of the split-flow scheme on the absorber size was also investigated. The split-flow scheme in most cases does not have an apparent effect on the absorber size or the packing volume required for a capture target. From **Table 1**, a small change in absorber size (±5%) is found. It should also be noted that although the split-flow does not benefit the absorber size, it allows the absorption to achieve a relatively high CO_2 rich loading. This is because the split-flow acts as an intercooler within the absorber that prevents the solution temperature to exceed the mass-transfer limit. This intercooling behavior can be demonstrated by the temperature profile in **Figure 3**.
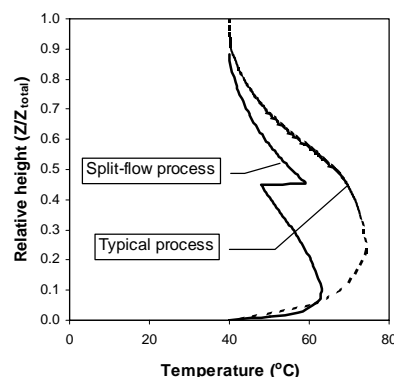

Figure 3. Absorber temperature profiles.

Conclusion

The amine treating plant using the split-flow configuration requires less reboiler heat-duty for solvent regeneration than the conventional plant, while still achieving high CO_2 capture efficiency. The reboiler heat-duty can be reduced to as low as 55,000 Btu/lbmol CO_2 with a 95% CO_2 capture efficiency and a large CO_2 cyclic capacity of solution. However, the regenerator height must be increased to accommodate the CO_2 stripping.

References
(1) Kohl, A., Nielsen, R., Gas Purification, 5th edition, Gulf Publishing Company: Texas, 1997.
(2) Aroonwilas, A., Chakma, A., Tontiwachwuthikul, P., Veawab, A. *Chemical Engineering Science*, 2003, 58: p. 4037-4053.

Figure 2. McCabe-Thiele diagram for CO_2 stripper.

TECHNICAL AND ECONOMIC ANALYSIS OF CO₂ CAPTURE PLANT USING BLENDED MEA-MDEA: A CASE STUDY FOR COAL-FIRED POWER PLANT FLUE GAS

Amornvadee Veawab and Adisorn Aroonwilas

Faculty of Engineering, University of Regina
Regina, Saskatchewan, Canada S4S 0A2

Abstract

This work provides a comprehensive study of using an aqueous blended monoethanolamine (MEA)-methyldiethanolamine (MDEA) for carbon dioxide (CO_2) capture from low-pressure coal-fired power plant flue gas. The study consists of technical evaluations of overall process performance and analysis of process cost. The technical evaluation involves experimental determinations of absorption performance, energy requirement for solvent regeneration, and corrosion. The cost analysis was performed using a cost model offering great capability and flexibility for process design, simulation, and optimization. The results show that using the MEA-MDEA with an appropriate mixing ratio instead of conventional MEA can significantly reduce energy consumption for solvent regeneration and corrosion rate, while compromising CO_2 capture performance.

Introduction

Chemical absorption using aqueous alkanolamines is considered to be an immediate technology for capturing carbon dioxide (CO_2) from low-pressure coal-fired power plant flue gas. Monoethanolamine (MEA) is a promising choice of solvents because of its high CO_2 reactivity and low chemical cost compared to other alkanolamines. However, the overall cost of MEA process is prohibitively high and uneconomical due to high energy consumption for solvent regeneration.

At present, use of blended-alkanolamines is of great interest in gas treating plants since it offers a number of advantages over use of single-alkanolamines. The most common blends are mixtures of MEA-methyldiethanolamine (MDEA), and diethanolamine (DEA)-MDEA. These blends combine the favorable features of MDEA (i.e. higher equilibrium CO_2 solubility and lower energy requirement for solvent regeneration) with the favorable feature of MEA or DEA (i.e. higher reaction rate with CO_2). As a result, a fair reduction in the process cost can be expected. This work therefore aims at evaluating the overall performance of MEA-MDEA process in aspects of absorption efficiency, energy consumption for solvent regeneration and corrosion rate, and ultimately translating the performance to an overall cost-saving in relation to the MEA process.

Experimental Evaluation

CO₂ Absorption Efficiency. **Figure 1**[1] shows CO_2 absorption performance of three solvents, MEA, MDEA and MEA-MDEA. The performance is presented as an overall mass-transfer coefficient (K_Ga_v) index representing a ratio of K_Ga_v value of MEA-MDEA to that of MEA. It is apparent that the MEA-MDEA process offers a lower CO_2 absorption performance than the MEA process, but a higher performance than MDEA under the test condition. While the K_Ga_v index for MEA is 1.0, the index for MEA-MDEA ranges from 0.22 to 0.45, which is less than half of the index for MEA. The lower performance of MEA-MDEA is primarily attributed to the lower kinetic rate of CO_2 absorption and the higher solution viscosity.
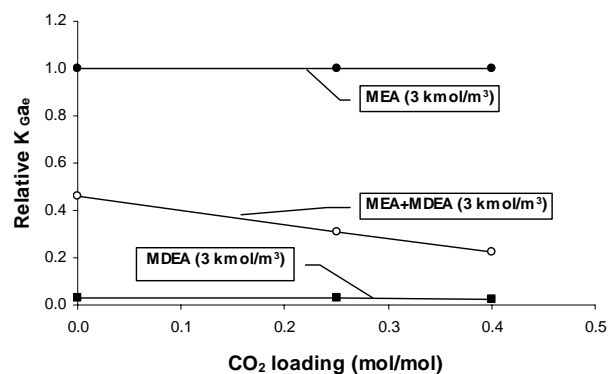

Figure 1. CO_2 absorption performance.

Energy Requirement for Solvent Regeneration. **Figure 2**[2] shows energy requirements for solvent regeneration of MEA, MDEA, and MEA-MDEA reported in terms of reboiler heat-duty index in relation to MEA (index of MEA = 1). The heat-duty index of MEA-MDEA is less than MEA but greater than MDEA. It ranges between 0.3 and 0.6 depending on operating condition. Hence, a reduction in energy requirement for solvent regeneration can be expected when blended MEA-MDEA is in service.
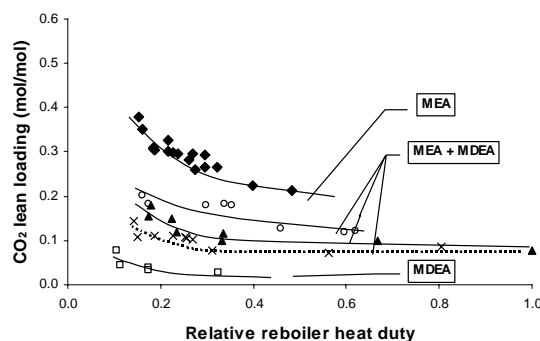

Figure 2. Energy requirement for regeneration.

Corrosion. Corrosion rate of process materials depends on many factors including type of absorption solvents. MEA is known to be the most corrosive, while MDEA is the least compared to other alkanolamines. Blending MEA with MDEA makes the MEA system less corrosive. Form **Figure 3**[3], the corrosion rate of carbon steel in MEA-MDEA system is in between that in MEA and MDEA, and varies with mixing ratio. At 80°C under CO_2 saturation and 3 kmol/m³ total amine concentration, the corrosion rate in MEA-MDEA with a mixing ratio of 1:1 is much less than the MEA's. Its corrosion index is 0.57, while the index for MEA is unity.
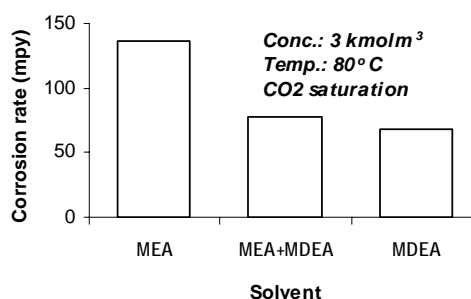

Figure 3. Solvent and corrosivity.

Economic Analysis

From the above experimental results, it is apparent that a trade-off feature of the MEA-MDEA process exists. This trade-off comprises gain and loss in process improvement, which can be translated into cost reduction and increment, respectively. The gain in process improvement refers to the decrease in energy consumption during solvent regeneration and corrosion rate, while the loss refers to the decrease in CO_2 absorption performance.

The trade-off was translated into a process cost to examine the actual impact of using MEA-MDEA instead of MEA for CO_2 capture. The cost analysis was carried out using our in-house cost model. The model offers great capability and flexibility for process design, modeling, simulation and optimization. It accounts for two key cost-elements, capital and operating costs. The capital cost was derived from process design information particularly capture performance, which has a direct impact on dimensions of absorption column and regeneration facilities, flue gas blower, intercooler, water-wash section, piping systems, heat-exchangers, storage tank and circulation pumps. The operating cost was derived from process utilities including steam for solvent regeneration, cooling water, and electricity, operating labors, maintenance/ repairs, operating supplies/ lab, fixed charge including depreciation, taxes, insurance, plant overhead cost, etc.

A case study of a coal-fired power plant capturing 6,000 tonne CO_2/day was established for the demonstration of cost comparison between MEA and MEA-MDEA processes. The amine plant is designed for 6 process trains with a capture efficiency of 95%, and operated at 0.22 lean and 0.50 rich CO_2 loadings (mol/mol). Two formulations of MEA-MDEA with two different mixing ratios are considered. As seen in Table 1, the total production cost index of MEA-MDEA Formula 1 is 0.87 in relation to MEA (MEA cost index = 1), which can be translated into 13 % cost reduction. This reduction is mainly attributed to a significant reduction in steam cost (i.e. 67%). It should be noted that the overall cost saving is not proportional to the reduction in steam cost because it accounts not only for utilities, but also other variable production cost including operating labour, maintenance and repairs, and others.

It should also be noted that a reduction in overall production cost of this MEA-MDEA process depends greatly on mixing ratio. For instance, the cost of MEA-MDEA Formula 2 is comparable to that of MEA, indicating no overall cost saving. This is a result of a non-optimal trade-off between CO_2 capture performance and energy consumption for solvent regeneration. Although achieving about 70% reduction in steam cost, the Formula 2 encounters with a low capture performance. This results in a larger capital investment as shown in Table 1.
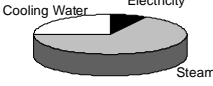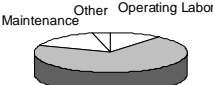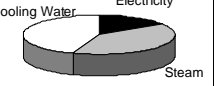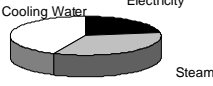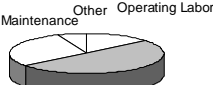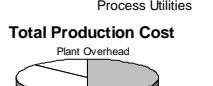
Conclusion
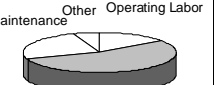
Blended MEA-MDEA is an attractive choice of solvent for CO_2 capture from low-pressure flue gas stream since it shows a promising cost-saving opportunity in relation to MEA. The cost saving is primarily a result of lower steam cost. A favourable saving can however be achieved only when an appropriate mixing ratio of MEA-MDEA as well as optimal operating conditions are applied.

References
(1) Aroonwilas, A., Veawab, A. *Industrial and Engineering Chemistry Research*, **2004**, 43(9): p. 2228-2237.
(2) Veawab, A., Tontiwachwuthikul, P., Chakma, A. *Industrial and Engineering Chemistry Research*, **1999**, 38(10): p. 3917-3924.
(3) Veawab, A., Tontiwachwuthikul, P., Aroonwilas, A., Chakma, A. 2003. *Proceedings of the Sixth International Conference on Greenhouse Gas Control Technologies (GHGT6)*, Kyoto, Japan, October 1-4, **2002**, edited by J. Gale, Y. Kaya, Pergamon.

Table 1. Results of cost analysis.

MEA (Base case)	MEA-MDEA (Formula 1)	MEA-MDEA (Formula 2)
Production cost index = 1.00	Production cost index = 0.87	Production cost index = 1.03

HOT PRESSURIZED WATER FRACTIONATION AND TOXICOLOGICAL CHARACTERIZATION OF CARBONACEOUS PARTICULATE MATTER

Alena Kubátová,[1] Artur Braun,[2] Laura C. Dronen,[1] Matthew J. Picklo Sr.,[3] and Steven B. Hawthorne[1]

[1]Energy & Environmental Research Center, University of North Dakota, PO Box 9018, Grand Forks, ND 58202-9018
[2]Consortium for Fossil Fuel Science, University of Kentucky, 533 S. Limestone St., Lexington, KY 40506
[3]Department of Pharmacology, Physiology & Therapeutics, School of Medicine and Health Sciences, University of North Dakota, PO Box 9037, Grand Forks, ND 58203-9037

Introduction

Knowledge about health impacts of particulate matter (PM) grows proportionally with the development of analytical and toxicological techniques and the links between them. Currently, PM toxicity is mainly studied for inorganic species and nonpolar organics. Only recently has a possible contribution from polar organics been recognized because of the analytical difficulty in purifying and identifying polar fractions and the necessity to employ more than one organic solvent to extract a wide polarity range of PM organics.[1]

The advantage of hot pressurized (liquid) water (under sufficient pressure to maintain it in the liquid state) is based on a change in water's polarity by a simple temperature increase. Heating water from 25° to 300°C decreases water's polarity, expressed as a dielectric constant (from 78 to 20).[1, 2] In contrast to hot pressurized water, a polar solvent such as methanol has a dielectric constant of 30. The practical use of controlling water's polarity with temperature is related to the ability to solubilize various organic compounds. Thus the change in solubility with increasing temperature was exploited for sequential extraction of phenols, PAHs, and alkanes from petroleum waste sludge.[3]

Therefore, the aim of this work was to employ hot pressurized water for the extraction and fractionation of organic PM, estimate the importance of the resulting fractions with three *in vitro* assays, and compare the toxicity of the fractions to gas chromatographic/mass spectrometric (GC/MS) characterization.

Experimental

Sample Material. Bulk diesel exhaust PM was collected from the exhaust pipe of a diesel bus. Two samples of diesel exhaust PM were generated with and without 5% diethyl carbonate oxygenate. Bulk wood smoke PM was collected from a chimney that vented an airtight wood stove burning a mix of hardwoods.[4] Fifty-milligram portions of each material were used for all extraction experiments.

Extraction. The hot pressurized water extraction was performed in an apparatus previously described in detail.[5] In brief, the extraction system consisted of an ISCO model 100D syringe pump delivering water at a constant flow rate of 0.5 mL/min to a preheating coil and extraction cell mounted in a gas chromatograph oven. At the outlet of the extraction system, outside of the oven, a valve was placed to maintain the system pressure, ensuring that the water was in the liquid state at all temperatures. The extracts were collected into ice-cooled vial to prevent sample loss.

Toxicity assays. Three *in vitro* toxicity assays were performed. Bacterial genotoxicity assay SOS chromotest was based on the production of β-galactosidase enzyme.[1] The oxidative stress assay was based on the glutathione (GSH) depletion in macrophages (RAW 264.7) determined with monochlorobimane probe.[6] The cytotoxicity assay was monitored using lactate dehydrogenase (LDH) activity.

Results and Discussion

The comparison of fractions collected at different temperatures showed higher genotoxicity in midpolar fractions of diesel exhaust PM corresponding to the presence of nitropyrene and other nitroPAHs. Interestingly, adding diethyl carbonate oxygenate to a reference diesel fuel at a blend level of 5% resulted in increased genotoxicity of diesel exhaust PM (Figure 1). In addition, the different distribution of genotoxicity in fractions of diesel with oxidizer (extracted at 150°–200°C) and reference diesel (extracted at 250°C) suggests the occurrence of different genotoxic components.
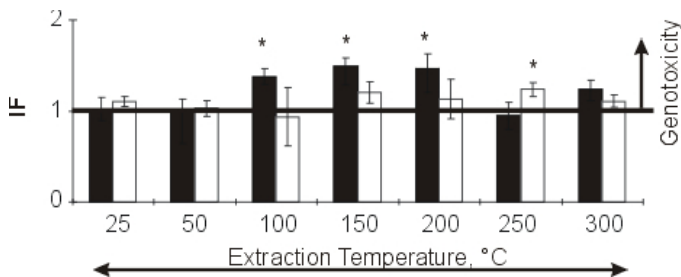

Figure 1. The direct genotoxicity of a wide-polarity range of fractions from diesel exhaust PM generated with (black bars) and without (clear bars) the presence of diethyl carbonate. Induction factor (IF) is defined as a ratio of β-galactosidase (a marker of DNA damage) and alkaline phosphatase (a marker of protein synthesis). Each fraction was diluted 1/50. *significant increase in genotoxicity.

The oxidative stress was evaluated based on glutathione (GSH) depletion, which is major antioxidant in lung tissues, and cytotoxicity to macrophages. For diesel exhaust PM, significant GSH depletion was observed in the nonpolar PAH fraction but also (unexpectedly) in the polar fractions (extracted at 50°–100°C), possibly corresponding to dicarboxylic acids.[7] For wood smoke particulate, midpolarity and nonpolar fractions exhibited more pronounced GSH depletion, which may be caused by methoxyphenols dimers, oxyPAHs, and PAHs.

Conclusions

In summary, the results indicate the toxicological importance of polar air particulate fractions, which have been neglected in previous studies employing non- or slightly- polar organic solvents. Moreover, this work demonstrates the potential of hot pressurized water to selectively extract polar and nonpolar species for toxicological testing. Finally, diesel emissions generated from different fuels or from fuels containing different additives may have different health and environmental impacts.

References
(1)   Kubatova, A.; Steckler, T. S.; Gallagher, J. R.; Hawthorne, S. B.; Picklo, M. J. *Environ. Toxicol. Chem.* **2004,** *23* (9), 2243.
(2)   Hawthorne, S. B.; Kubatova, A., Sampling and Sample Preparation for Field and Laboratory. In *Comprehensive Analytical Chemistry,*

        1st ed.; Pawliszyn, J., Ed., Elsevier: New York, NY, USA, 2002;
        Vol. 37, pp 587.

(3)   Yang, Y.; Hawthorne, S. B.; Miller, D. J. *Environ. Sci. Technol.*
        1997, *31* (2), 430.

(4)   Hawthorne, S. B.; Krieger, M. S.; Miller, D. J.; Mathiason, M. B.
        Environ. Sci. Technol. **1989,** *23* (4), 470.

(5)   Hawthorne, S. B.; Yang, Y.; Miller, D. J. *Anal. Chem.* **1994,** *66*
        (18), 2912.

(6)   Nauen, R.; Stumpf, N. *Anal. Biochem.* **2002,** *303* (2), 194.

(7)   Kawamura, K.; Kaplan, I. R. *Environ. Sci. Technol.* **1987,** *21*, 105.

CHARACTERIZATION OF CARBONACEOUS AIRBORNE PARTICULATE MATTER WITH NEXAFS SPECTROSCOPY

Artur Braun[1], Simon B. Mun[2], Sue Wirick[3,4], Chris Jacobson[4], Alena Kubatova[5], Naresh Shah[1], Frank E. Huggins[1], Gerald P. Huffman[1], and Matti Maricq[6]

[1]Consortium for Fossil Fuel Science, University of Kentucky, Lexington KY, [2]Advanced Light Source, Berkeley National Laboratory, Berkeley CA, [3]National Synchrotron Light Source, Brookhaven National Laboratory, Upton, NY, [4]SUNY, Stony Brook NY, [5]EERC, University of North Dakota, Grand Forks ND, [6]Ford Motor Company, Dearborn MI

Introduction

Diesel soot is believed to be a major constituent of airborne particulate matter (PM) and held partially responsible for global climate change and adverse health effects in humans. We have already published some synchrotron work on diesel soot [1-3] recently. Here we give an overview of our efforts to characterize soot with near-edge X-ray absorption fine structure spectroscopy (NEXAFS). We will present three recent findings, which we think are worthwhile to mention.

1) PM is often studied with electron microscopy, and some electron microscopes provide electron energy loss spectroscopy (EELS) as an extra feature for analysis. Since, EELS has emerged almost to a standard chemical characterization tool for fine PM. We show that EELS fails to resolve the important surface functional groups on carbonaceous PM, while NEXAFS spectra give clear evidence of such groups, allowing even for quantitative analysis.

2) Diesel soot is typically thought to be the major carbonaceous constituent of urban particulate matter. Our NEXAFS spectra of a diverse series of diesel soot from a manifold of sources show a characteristic, strong π resonance due to C=C carbon double bonds at 285 eV. This resonance dominates the entire carbon K-shell spectrum of diesel soot. However, the corresponding available NEXAFS spectra of urban PM show a significantly diminished resonance at 285 eV, hence not confirming that diesel soot is a major constituent of urban PM.

3) Extracts of diesel soot were exposed to highly intense synchrotron radiation for several periods, and NEXAFS spectra were recorded in between. The intensity of the carboxyl group peak in the NEXAFS was significantly reduced, and a new peak, most likely indicative to an organo-carbonate, evolved to the same intensity, giving evidence of the photochemical discharge of soot.

Experimental

Diesel soot was obtained from several independent sources, such as NIST standards 1650 and 2975, and exhaust from a Ford diesel engine car. Soot was also produced at the diesel test engine facility at the University of Utah, from three diesel fuels in a 2-stroke diesel test engine, operated under idle or under load conditions. We also studied NIST 1648 urban PM, and a number of other ambient or biomass derived PM samples. Extraction of volatiles was carried out with sub-critical water. NEXAFS experiments on soot powder, pellets, and dried extracts on gold foil were performed at beamline 9.3.2 at the Advanced Light Source (ALS) in Berkeley National Laboratory, but also with the scanning transmission X-ray microscope at beamline X1-A at National Synchrotron Light Source in Brookhaven National Laboratory.

Results and Discussion

Figure displays the NEXAFS and EELS spectra of diesel soot powder generated in a test engine. The EELS spectrum is very diffuse and shows only one major π resonance at 285 eV, this is the graphitic signature of soot. The NEXAFS spectrum shows this feature much sharper, with a smaller full width at half maximum. In addition, the NEXAFS shows signatures at 287 and 289 eV, indicative to resonances from surface functional groups like C-OH and COOH.
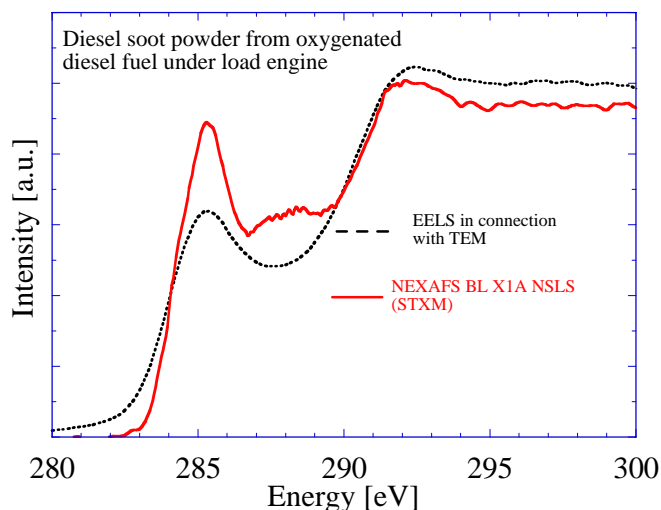

Figure 1. NEXAFS (solid line) and EELS (dashed) spectrum of diesel soot.

Figure 2 shows the NEXAFS spectra from a diesel soot extract, obtained from the STXM microscope in Brookhaven Lab. The radiation beam in this instrument is very intense and obviously induces photochemical reactions in the extract. The carboxyl COOH peak around 288 eV experiences a significant decrease in intensity during irradiation, while at 290 eV a new peak occurs and grows in intensity. We have made exactly the same observation with alginic acid and, since its chemical structure is known, could propose a reaction scheme where carboxyl would decompose under irradiation into carbonate and water. The same would apply to the diesel soot extract. This could be an interesting route to study in-situ photochemical reactions on PM. In addition to the strong effect observed with carboxyl, we see minor changes at 285 eV, which could be due to changes in the benzoquinone species, which are observed in this energy range.

Figure 3 compares the NEXAFS spectra of urban PM, which was sampled by either NIST in St. Louis, Missouri (this is a commercially available standard from NIST, collected over a longer period), or by our group in the city of Lexington, Kentucky. Both spectra show relatively weak signals at 285 eV, where C=C bonds are typically observed. In contrast, hydrocarbons, carboxyl, and carbonyl are observed between 286 and 290 eV and give a much stronger signal in these two urban PM samples.

We compare urban PM with diesel soot, graphite, and bio-mass derived soot in Figure 4. Graphite is a very good reference for carbon NEXAFS work like here. It has a very dominant resonance at 285 eV, indicative to the C=C in the aromatic graphene sheets. The NEXAFS spectrum of diesel soot comes very close to the graphite spectrum, except that diesel soot (here: a soot sample from a Ford diesel car) shows an additional and significant peak at 287 eV due to surface functional groups like C-OH, for instance. The two remaining

spectra in this Figure are from the NIST urban PM sample, and from a deposit in a wood furnace that was fed with 3 year old dried beech wood. These two spectra also have a significant peak at around 287 eV, but the peak height ratio between these and the C=C peak at 285 eV is greatly different from that in diesel soot, and graphite.
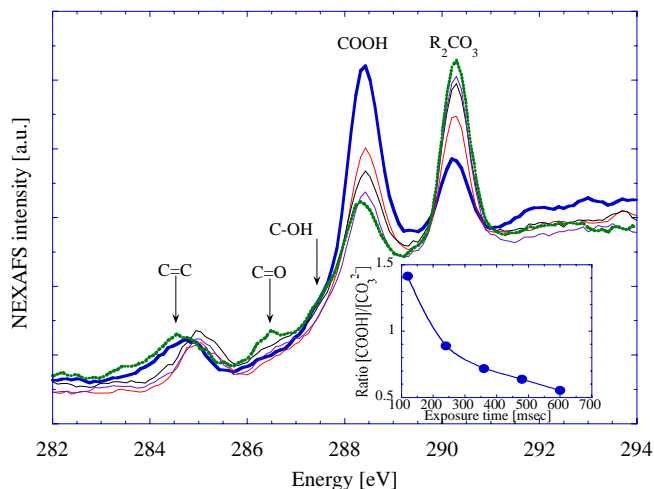

Figure 2. NEXAFS spectra of diesel soot extract sample for various synchrotron beam exposure times. Prior to irradiation, the carboxyl peak (COOH) dominates the spectrum. With increasing exposure, the carbonate resonance (R_2CO_3) evolves and increases.
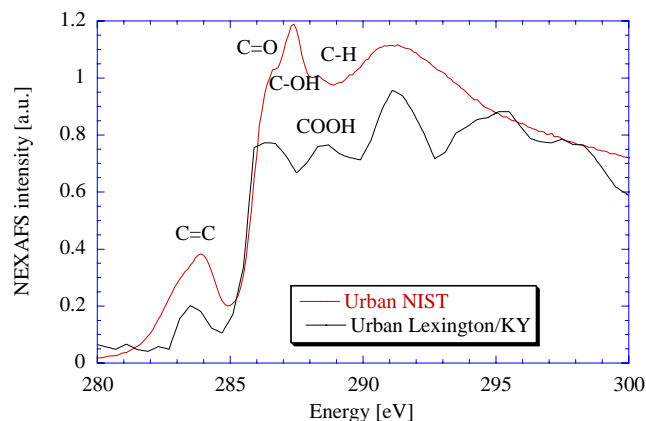

Figure 3. NEXAFS spectra of urban PM collected in St. Louis, and in Lexington (NIST, St. Louis, MO).

The chemical complexity of particulate matter almost mandates to simplify the analysis where ever possible. We have therefore tried to record NEXAFS spectra from soot and other PM extracts. Figure 5 shows how the NEXAFS spectra of soot and volatiles differ depending on whether the "dry" soot core is investigated, or the dried volatiles. The particular sample here is a series of extracts removed with subcritical water at various temperatures.
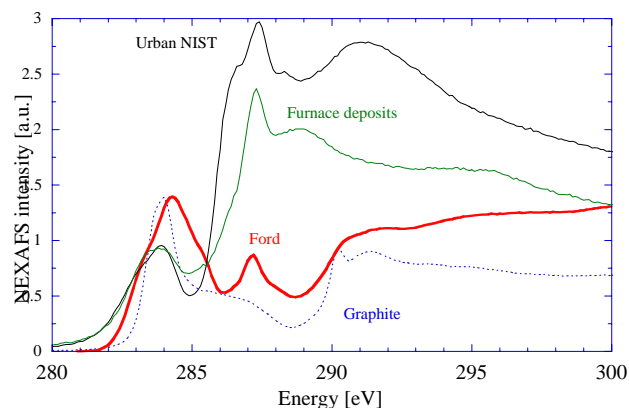

Figure 4. NEXAFS spectra of urban PM collected in St. Louis (NIST), diesel soot (Ford), graphite, and biomass derived soot (Furnace deposits).

Soot extracts, residuals and soot pellets were studied with NEXAFS [3,4]. Similar to graphite, soot spectra show a strong resonance of C=C bonds at 285 eV. Extraction of volatiles enhances the ratio between C=C peak intensity and peaks at energies between 286 eV and 289 eV, which result from aliphatics, C-H bonds, carbonyl and carboxyl groups, for instance. Unlike EELS with TEM [3], NEXAFS permits a detailed study of surface functional groups. Our extraction experiments are intended to facilitate deconvolution of soot spectra.
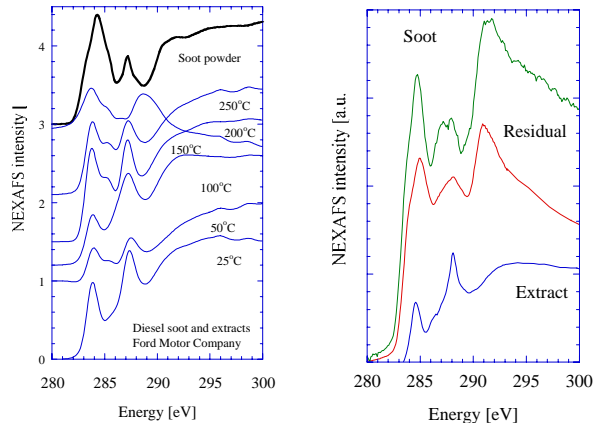

Figure 5. Left: NEXAFS spectra of soot as prepared, one extract, and the corresponding residual. Right: Sequence of NEXAFS spectra from soot and extracts for various extraction temperatures.

The right image in figure 5 shows clearly that the volatiles have only weak C=C peak contributions, while the contributions from the surface functional groups and aliphatics are dominant.

Conclusions

Carbon NEXAFS spectroscopy is a promising technique for the structural characterization and molecular speciation of particulate matter, including its extracts. We point out that these techniques are relatively straightforward and can be done in a high-throughput

mode. A number of conclusions can be made. For instance, radiation induces chemical reactions in soot volatiles. Also, the discrepancy between urban PM and diesel soot reveals that diesel soot is not necessarily the major constituent in urban PM. Of course, further studies are necessary to really confirm this finding, because weathering of soot is not yet included in our studies. Also, note, that all results reported here would not have been able with regular electron microscopy based EELS analysis.

References
(1)   Braun, A.; Huggins, F.E.; Seifert, S.; Ilavsky, J.; Shah, N.; Kelly, K.E.; Sarofim, A.; Huffman, G.P. Combustion and Flame, **2004**, 137 (1/2), 63-72.
(2)   Braun, A.; Ilavsky, J.; Jemian, P.R. *Deformation of diesel soot aggregates studied with ultra small angle X-ray scattering as a function of pellet pressure. Submitted to J.Appl.Phys.*
(3)   Braun, A.; Wirick, S.; Jacobsen, C.; Huggins, F.E.; Mun, S.B.; Shah, N.; Chen, Y.; Huffman, G.P. Carbon, **2005**, 43 (1), 117-124.

IGNITION QUALITY EFFECTS OF ADVANCED FUELS AT REDUCED TEMPERATURES

Joshua D. Taylor and Robert L. McCormick

National Renewable Energy Laboratory
1617 Cole Blvd. MS#1633
Golden, CO 80401
(303) 275-4439

Introduction

A primary goal of the U.S. Department of Energy is to reduce the nation's dependence on imported petroleum. In the transportation sector, this is being pursued by increasing the efficiency of fuel use and by replacing petroleum with non-petroleum based fuels and blending components. These tasks require an understanding of how fuel properties affect combustion efficiency and emissions so fuels can be screened (or tailored) based on their predicted performance in a particular type of engine. Discovering fuels that enable high efficiency operation or that improve public acceptance of existing high efficiency engines is a primary goal of the research described in this paper.

A central issue in screening fuels for use in current compression ignition engines or advanced combustion engines is ignition quality. In current compression ignition engines, ignition quality is quantified in terms of cetane number (CN), which is a measure of the delay between fuel injection and start of combustion in a single-cylinder engine at specified conditions. Although it is a convenient measure of ignition quality with a long history, CN is not necessarily an accurate metric to rank fuels for all operating conditions.

One condition where cetane number may not be the most appropriate metric for ignition quality is under cold-start conditions (*i.e.*, starting an engine that has equilibrated at ambient temperature below 0°C). Cold-start conditions are important for light-duty diesel sociability because these engines can have significantly higher emissions (*e.g.*, white smoke), lower fuel economy, and lower power during and immediately after cold-starting. During cold-start, all engine components are initially at the soak temperature of the vehicle, resulting in substantially lower charge air temperatures. Because of the reduced charge air temperature, ignition delay is longer and combustion is less complete than under normal operation in a hot engine. However, the temperature dependence of ignition delay can vary depending on fuel composition. This is equivalent to saying that different fuels can have different activation energy for ignition, such that the ranking of fuels by ignition delay can change with temperature. This implies that CN (measured at a higher temperature) may not be a sufficient metric for cold-start ignition quality.

In this paper, we investigate the effect of temperature on ignition delay for real fuels and pure compounds using the Ignition Quality Tester (IQT™) – a constant volume combustion apparatus. The goal of this research is to understand how the molecular structure of a fuel compound affects the temperature dependence (activation energy) of ignition delay. From this understanding, we propose several fuel blending components with improved ignition properties for diesel engines at cold-start conditions.

Experimental

The ignition delay of a fuel or pure compound can easily be measured with the IQT™ constant volume combustion apparatus. The IQT™ is equipped with a pintle-type fuel injector and a high-speed pressure transducer. Ignition delay is measured as the elapsed time from injection to the time when the chamber pressure reaches $P_{initial} + 50$ psi. The user may set the charge temperature and pressure arbitrarily, but to be in accordance with ASTM D6890-03a, the standard settings for the charge air are 310 psig and 550ºC. A correlation has been developed to convert the measured ignition delay under these conditions into a derived cetane number (DCN), which corresponds well with the CN measured by ASTM D613 (cetane engine). The system is fully automated; an experiment consists of 15 pre-injections (to equilibrate system temperatures) followed by 32 additional injections. The reported ignition delay is the average value determined from the 32 injections. For a more comprehensive description of this test methodology, see Allard et al.[1] Sample output from the IQT™ apparatus is shown in Figure 1. In this figure, the light line corresponds to the injector needle position and the dark line represents the combustion chamber pressure.
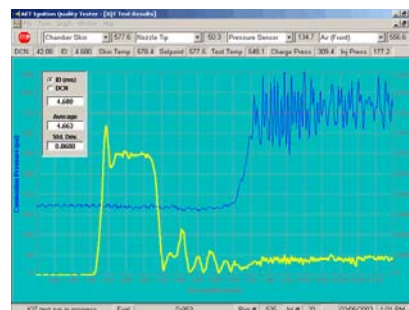

Figure 1. Sample IQT™ output of ignition delay measurement

Although the IQT™ is typically used to measure the DCN of fuels, it can also be used to measure how ignition delay varies with temperature, pressure, and charge composition (*i.e.*, oxygen concentration). In this project, the ignition delay was measured for charge air (21% O_2) at 310 psig and temperatures of 360°–580°C. Fourteen fuels were investigated, including 5 "real" fuel mixtures and 9 pure compounds. The "real" fuel mixtures included California specification diesel (CARB), CARB diesel blended with 20% biodiesel, ultra low sulfur diesel (BP-15) additized with 2000 ppm of a cetane improver (2-ethyl hexyl nitrate or EHN), Fischer-Tropsch (F-T) diesel, and F-T jet fuel (JP5). The pure compounds included heptane, cetane, heptanol, hexyl methyl ether (HME), 2-heptanone, methyl caproate, di- and tri-propylene glycol monomethyl ether (DPGME & TPGME), and triethylene glycol monomethyl ether (TEGME).

Results

The ignition delay data can be conveniently plotted as a log of the rate versus the inverse of temperature (similar to an Arrhenius plot) to determine how a reaction rate varies with temperature. Arrhenius plots are typically used for determining activation energies from rates of elementary reactions, where the activation energy (slope of plot) is a metric for how strongly the rate varies with temperature. Although the spray ignition in the IQT™ is clearly not a single elementary reaction (*i.e.*, spray, evaporation, mixing, ignition chemistry), there is some justification for plotting ignition delay results on an Arrhenius plot[*]. This plotting is logical if we think of ignition in reaction kinetic terms such as the time it takes for the reaction to produce a certain concentration of some reactive intermediate (such as OH• radical) or as the time it takes for a certain

---

[*] To be precise, an Arrhenius plot should be the logarithm of a rate. In this case, a characteristic rate would be the inverse of the ignition delay. The resulting plot would be equivalent to multiplying all values by -1, in which case the negative of the slope would equal the pseudo-activation energy.

fraction of the fuel to be consumed. In this manner, the slope of the plot is analogous to the activation energy for ignition.

Figure 2 shows an Arrhenius-type plot of the ignition delay measurements for a subset of five fuels, and Figure 3 shows all of the data measured. These curves are nonlinear because the ignition rate is not an elementary reaction and the physical delay (*i.e.*, spray, evaporation, mixing) is lumped with the chemical (kinetic) delay.
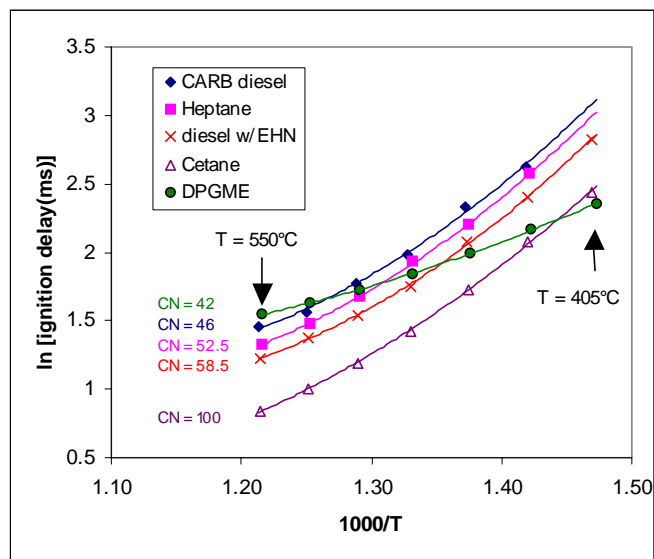

Figure 2. Arrhenius-type plot of ignition delay data for five fuels
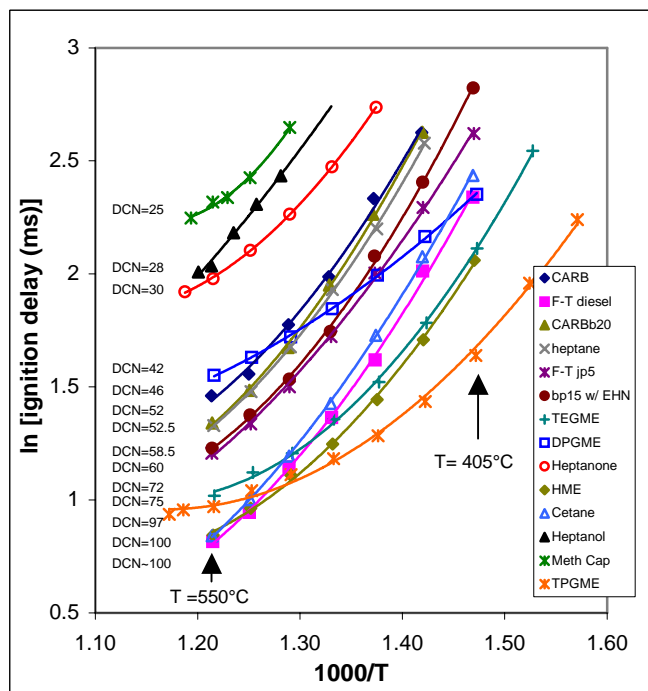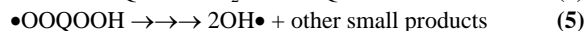

Figure 3. Arrhenius-type plot of ignition delay data for all fuels

Figures 2 and 3 show how the ignition delay of various classes of molecules has different dependence on temperature (*i.e.*, different slopes on the Arrhenius plot). All the hydrocarbon fuels show approximately the same temperature behavior. That is, the curves for all hydrocarbons look similar in shape and slope, but are shifted

vertically by the DCN, which corresponds to the ignition delay at 550°C. Since the slopes are almost the same, the molecules have approximately the same activation energy for ignition. In contrast, many of the oxygenates show a much weaker dependence on temperature (lower relative slope) compared with the hydrocarbon fuels. Most notably different are the acetals[†] (DPGME, TPGME, and TEGME), but HME, 2-heptanone, and methyl caproate also show a reduced slope relative to the hydrocarbon fuels. Heptanol is the only oxygenate that does not show reduced temperature dependence.

Discussion

The reason for the reduced temperature dependence for some of the pure compounds is related to the primary reaction pathway for ignition. During preignition reactions, the initial step is a hydrogen abstraction from the fuel molecule (typically by an OH• radical)[‡]. This is followed by an oxygen addition that creates a peroxy radical and then an internal rearrangement (which amounts to another H-abstraction). The remaining steps in the reaction sequence are a second oxygen addition and then several fast reactions that result in chain branching. The reactions are shown symbolically in Eqns. 1-5, where RH represents a generic fuel molecule and Q is the same as R with one H atom removed.

$$RH + OH\bullet \rightarrow R\bullet + H_2O \qquad (1)$$
$$R\bullet + O_2 \rightarrow RO_2 \qquad (2)$$
$$RO_2 \rightarrow \bullet QOOH \qquad (3)$$
$$\bullet QOOH + O_2 \rightarrow \bullet OOQOOH \qquad (4)$$
$$\bullet OOQOOH \rightarrow\rightarrow\rightarrow 2OH\bullet + \text{other small products} \qquad (5)$$

Since the reactions in Eqns. 1 and 3 both involve H-abstractions and are rate-limiting steps, it is logical to conclude that the overall activation energy for this series of reactions will be influenced by the energy barrier for these two steps. Furthermore, the activation energy for these H-abstractions will be proportional to the strength of the relevant C-H bonds in the fuel molecule and the abstraction will occur fastest where the C-H bonds are weakest.

In a fuel molecule with an electron-withdrawing functional group such as ether or carboxyl, the adjacent C-H bonds are significantly weakened from their normal values. This effect is in addition to the typical C-H bond strengths, where a primary CH_3 has much stronger C-H bonds than a secondary CH_2 that is in turn much stronger than a tertiary CH group. The weakest type of C-H bonds found in these selected compounds is a tertiary C-H bond adjacent to an ether linkage, such as those found in DPGME and TPGME (see Figure 4). The next weakest C-H bonds are secondary C-H bonds adjacent to either an ether linkage or a carboxyl group. In Figure 4, the tertiary C-H bonds adjacent to an ether linkage are shown with the small red (double) circles. Likewise, the secondary C-H bonds adjacent to an ether linkage, alcohol, or carboxyl group are shown with small blue (single) circles.

Furthermore, there is a second H-abstraction (Eqn. 3) that occurs in the ignition chemistry after the peroxy radical is formed. The activation energy for this step will again be proportional to the strength of the C-H bond and depend on the location on the molecule relative to the peroxy radical group. Since 6-membered transition state rings have the lowest ring strain, the most likely location for the internal H-abstraction is on a carbon atom that is 2 atoms away from where the initial abstraction occurred. A 7-membered transition state ring is only a slightly higher energy barrier.

[†] Acetals are molecules with at least two ether functional groups.

[‡] The first initiation reaction is an H-abstraction by O_2 since no OH• radicals are present. However, after the first initiation reaction, H-abstraction is dominated by OH• radical.
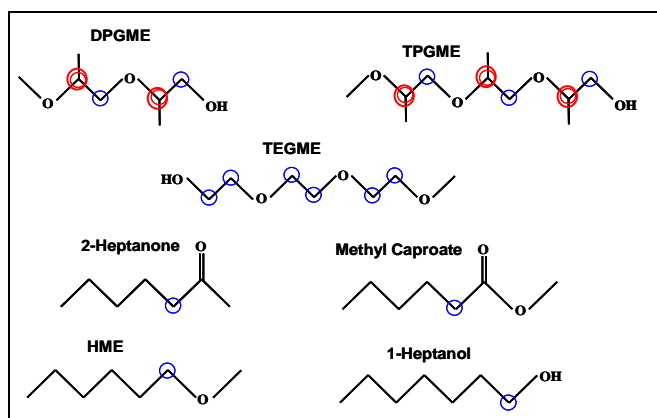
Figure 4. Structures of oxygenates tested in IQT™ with weakened C-H bonds circled

Clearly, the activation energy for DPGME and TPGME would be the lowest of the compounds tested because both have a tertiary C-H bond adjacent to an ether linkage where the initial abstraction would occur (see Figure 4). Subsequently, the internal rearrangement could occur either to a secondary C-H adjacent to an ether with a 6-membered transition state ring or to a tertiary C-H adjacent to an ether with a 7-membered transition state ring. Consequently, DPGME and TPGME show the lowest temperature dependence for ignition delay of the compounds investigated. TEGME has the next lowest activation energy because of its secondary C-H bonds adjacent to ethers for both the initial abstraction and the internal rearrangement. The molecules with the carboxyl group (2-heptanone and methyl caproate) have the next lowest activation energy; followed by hexyl methyl ether. Although the alcohol functional group does decrease the adjacent C-H bond strength, no reduced temperature dependence was observed relative to the hydrocarbons.

Impact on Compression Ignition Fuels. The reduced temperature dependence of these acetals (and other oxygenates) could have a significant impact on cold-start behavior in a conventional diesel engine. For example, DPGME has a DCN of 42 under standard test conditions (550°C). However, at 400°C [§] DPGME ignites faster than cetane (DCN = 100) because of the lower activation energy (see Figure 2). The result is that a vehicle fueled with pure DPGME would have an effective CN of >100 during cold-start. As the engine warms up, the fuel would ignite more like a typical diesel fuel (DCN =42). One possible result of this "effective cetane boost" at low temperatures is better cold-start performance and reduced emissions. Another possible result is that engine manufacturers could design light-duty diesel engines with a lower compression ratio, which could improve engine efficiency (i.e., reduce fuel consumption)[**].

Replacing hydrocarbon fuels with 100% oxygenates is economically impractical, but blending oxygenates with hydrocarbons at a level of 20% is more realistic. Often ignition properties of blends do not scale linearly with composition, so it was necessary to measure this low-temperature "cetane boost" at a 20% blend level. An Arrhenius-type plot of diesel fuel, DPGME, and a 20% blend of DPGME in diesel fuel is shown in Figure 5. Linear fits were applied to the data so the average slopes could be compared.
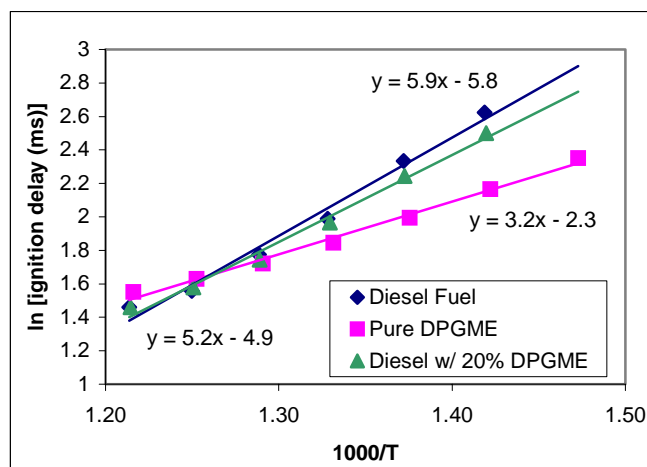

Figure 5. Effect of DPGME blending on activation energy for ignition

Figure 5 shows that the slope of the blend is reduced from that of the diesel fuel. Comparing the slope values from the linear fit shows that the effect is directly proportional to blending level. There is a 20% decrease relative to the difference in slope between the pure diesel and DPGME lines. From the curves of ignition delay for hydrocarbon fuels, one can estimate the effective CN of the 20% DPGME blend versus temperature. The result is a "cetane boost" of 6 CN units at 450°C and 10 CN units at 400°C [§]. Plans are currently underway to conduct engine or vehicle testing of these blends under cold-start conditions to validate this effect.

Conclusions

In this paper we presented data showing the effect of temperature on ignition delay (as measured in the IQT™) for 14 fuels and pure compounds in terms of activation energy for ignition. All hydrocarbon fuels tested showed a similar slope and shape, but most oxygenates showed a reduced dependence on temperature due to lower activation energy for ignition. The mechanism by which molecular structure affects the temperature dependence of ignition delay was described in the discussion of the IQT™ measurements. We propose that the slope of the ignition delay curves is related to the strength of the C-H bonds in the fuel molecules since the bond strength is correlated with the rate of H-abstraction reactions. Several oxygenates were identified that have cold-start ignition benefits, which will be investigated further in future research. Moreover, the fundamental understanding of why these compounds are beneficial may guide future research into other compounds that exhibit similar behavior.

References
(1) Allard, L.N.; Webster, G.D.; Ryan III, T.W.; Matheaus, A.C; Baker, G.; Beregszaszy, A.; Read, H.; Mortimer, K.; and Jones, G. *Society of Automotive Engineers*, **2001**, Technical Paper No. 2001-01-3527.

[§] A decrease in the intake charge air temperature of ~30-45°C results in a reduction of ~100-150°C in the compressed charge temperature assuming adiabatic compression.

[**] Light-duty diesel engines are designed with a higher compression ratio (often greater than 20) to achieve a high enough charge temperature for cold-start. If the engine manufacturer could reduce the compression ratio to ~16, frictional and pumping losses could be reduced resulting in higher engine efficiency.

INVESTIGATION OF A NOVEL OXYGENATE, METHYL 2-ETHOXYETHYL CARBONATE, AS A CLEAN DIESEL FUEL ADDITIVE

Hejun Guo, Xianxiang Huang

Xi'an Research Institute of Hi.-Tech., Hongqing Town, Xi'an 710025, P R China

Shenghua Liu, Longbao Zhou

Department of Automobile Engineering, Xi'an Jiaotong University, Xi'an 710049, P R China

Introduction

Currently, diesel engines are popular on many types of vehicles and machineries simply because they have attractive features of high power output and low fuel consumption. However, there are also environmental repercussions in that detrimental exhaust gases, especially the black smoke that diesel engines emit, contribute to increasingly serious air pollution. Currently, great importance has been attached worldwide to research and utilization of effective techniques to control harmful emissions from modern diesel engines. The addition of oxygenates into diesel fuel has proven to be one of the more promising methods of reducing diesel engine emissions and has been the focus of much research in recent years. Many experimental studies have found that the addition of alcohols, ethers and esters to diesel fuel can lead to significantly lower diesel engine emissions, and it also has been discovered that the reduction in black smoke correlates with the oxygen content of the diesel fuel (1). Since it has a high oxygen content and hence a high emission reduction potential, dimethyl carbonate (DMC) has received much attention recently and has been studied extensively (2-5). As shown by some related research studies, however, this oxygenate possesses a low ignition property so that it cannot be mixed with diesel fuel in large proportions, thereby restricting its practical application. Another research study suggested that when ester and ether groups are incorporated together in the oxygenate molecule, not only is the oxygen content enhanced, which may lead to further reduction in diesel engine exhaust emissions, but also the autoignition performance of the oxygenate may be improved at the same time (6). In the current study, by introducing an ether group into the DMC molecule, a new oxygenate, methyl 2-ethoxyethyl carbonate, is created as a new kind of clean diesel fuel additive.

Experimental

Preparation and characterization. The new oxygenate was prepared using DMC (4 mol) and ethylene glycol monoethyl ether (1 mol) as reactants. The transesterification reaction was carried out in a flask equipped with a fractionation column, with its top outlet temperature maintained between 62°C and 68°C, for sufficient time, using fine powder of potassium hydroxide (KOH, 0.01 mol) as catalyst. Upon reaction completion, no more methanol was produced, and the crude product was cooled to room temperature and filtered to remove solid KOH sediments. The crude product was then purified under vacuum to obtain the final desired colorless compound.

The chemical structure identification was accomplished with FTIR, ^{1}H NMR and GC-MS analytical techniques. An EQUINOX55 FT-IR spectrometer was used to conduct IR analyses. Its sample cell was constructed from KBr crystal. A superconducting NMR spectrometer of INOVA type made by VARIAN company was employed to carry out ^{1}H NMR analyses. CDCl$_3$ was selected as solvent, and TMS as the standard substance. The watched frequency was 400 MHz. A GC-MS apparatus of 6890GC-5973MS type was utilized to perform purity and MS analyses. The size of the capillary column selected was 50m×0.53mm×1um and SE-30 was chosen as stationary phase. In the ionization source, electron-impact energy was adjusted to 70 eV, and its temperature was maintained at 230 °C.

Engine testing. A single cylinder, 4-stroke, water-cooled, direct-injection diesel engine was modified so that determination of exhaust emissions, power output and fuel consumption could be determined. The technical parameters of the engine are listed in Table 1. A commercial No.0 diesel fuel meeting China national standard specification was used as base reference fuel into which the oxygenate was added for investigation. In the experiments, oxygenate volume percentages of 15%, 20% and 25% were selected for tests. A Bosch smoke tester of FOD-201B type was used to indicate smoke number, and an on-line exhaust emission analyzer was utilized to examine NOx, CO, and unburned HC. Power output was evaluated on an electrical eddy-current dynamometer and fuel consumption was appraised with an electric scale.

Table 1. Parameters of DI Diesel Engine Used

Parameter	Bore	Stroke	Connecting rod length	Displace-ment
Magnitude	100 mm	115 mm	190 cm	0.903 L
Parameter	Compression ratio	Combustion chamber	Rated power	Rated speed
Magnitude	18	ω shape	11 kW	2300 rpm

The engine tests were conducted under conditions of ambient temperature of 27°C, humidity of 81%, and engine water-cooling temperature of 80°C. In the experiments, when the engine went into steady operation at fixed state, all kinds of measurements were made according to certain well-defined procedures. It was found that even operating on the fuel blend containing 25% by volume of the oxygenate, the engine still ran normally during the tests.

Results and Discussion

Chemical structure of the oxygenate. The main absorption frequencies exhibited in the IR spectrum obtained for the oxygenate are listed in Table 2 with their group attributions identified. GC-MS analytical results demonstrated that there was only one peak corresponding to the oxygenate detected in its chromatograph. The following mass peaks (in amu) were revealed by mass spectrometry: M+1 at mass 149, $[CH_3OCOOCH_2CH_2]^+$ at 103, $[CH_3OCOOCH_3]^+$ at 90, $[CH_3OC(OH)OH]^+$ at 77, $[CH_2OCH_2CH_3]^+$ at 59, $[cycloCH_2CH_2-OCH_2CH_2]^+$ at 72, $[OCH_2CH_3]^+$ at 45, $[CH_3O]^+$ at 31, $[CH_2CH_3]^+$ at 29, and $[CH_3]^+$ at 15.

Table 2. IR Spectral Data for Methyl 2-Ethoxyethyl Carbonate

Frequency cm^{-1}	Group attribution	Vibration type	Strength
2977.0	-CH$_3$, -CH$_2$	ν_{as}	m
2871.2	-CH$_3$, -CH$_2$	ν_s	m
1764.7	C=O	ν	s
1444.6	-CH$_2$	δ	s
1387.9; 1374.9	-CH$_3$	δ	m
1270.0	=C-O (ester group)	ν_{as}	s
1130.9	C-O-C (ether group)	ν_{as}	m

Table 3 displays the ^{1}H NMR data obtained for the oxygenate. From the results illustrated in Table 1, Table 2 and the MS data, it is easily concluded that the oxygenate synthesized is indeed methyl 2-

ethoxyethyl carbonate, with its chemical structure being $CH_3OCOOCH_2CH_2OCH_2CH_3$.

Table 3. [1]**H NMR Data for Methyl 2-Ethoxyethyl Carbonate**

Chemical shift, ppm	1.226	3.551	3.669	3.802	4.298
Proton peak splitting	triplet	quartet	triplet	singlet	triplet
Coupling constant	6.8 Hz	6.8 Hz	4.8 Hz	-	4.8 Hz
Peak area /Proton number	3.00/3	2.11/2	2.09/2	3.17/3	1.87/2

Exhaust emissions and performances. Two sorts of engine operation conditions of full-load and partial-load at 2000 rpm were selected for studying changes of emissions, power and fuel economy.

Figures 1 and 2 demonstrate the results of CO emissions in full-load tests and partial-load tests, respectively. The figures reveal that the emitted CO expressed as a volume percentage of total gaseous emissions declined remarkably with the addition of methyl 2-ethoxyethyl carbonate. In full-load tests, as can be easily seen from Figure 1, CO decreased with the increase of the oxygenate content at each speed tested. When adding 25% by volume of the new oxygenate, CO decreased by 29.2% to 40.5%, relatively. In partial-load tests, the absolute reduction in CO emissions apparently depends considerably on brake mean effective pressure(BMEP): as the pressure rose, the absolute decrease became larger and larger. In fact, the relative reduction from 46.7% to 69.4% in partial-load tests was approached.
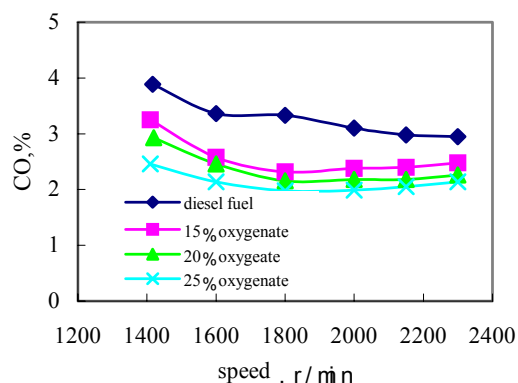

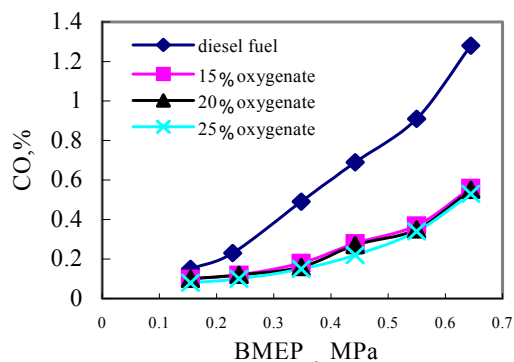**Figure 1.** Effect of the oxygenate on CO emissions at full loads

Figure 2. Reduction in CO emissions under partial-load conditions at a speed of 2000 rpm

Figure 3 displays the change of smoke emissions with brake mean effective pressure under different partial loads. The figure readily shows that the Bosch smoke number is lowered remarkably by the addition of methyl 2-ethoxyethyl carbonate. In partial-load tests, as was the case for CO emissions described above, the absolute reduction in smoke emissions is apparently related to brake mean effective pressure, for as the pressure rose smoke emissions decreased more and more. The maximum reduction in smoke emissions by 50 % was achieved at pressures of 0.23 MPa and 0.44 MPa, respectively.
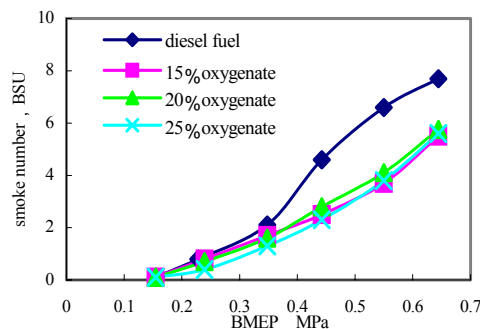

Figure 3. Reduction in smoke emissions under partial loads at a speed of 2000 rpm
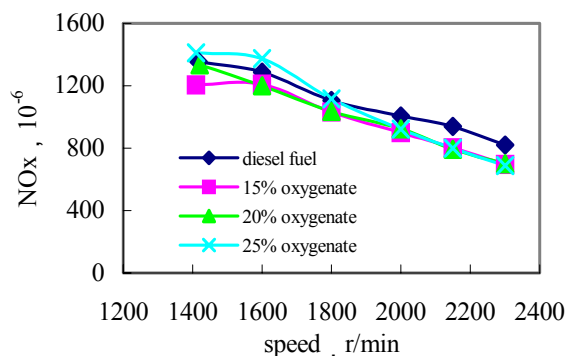

Figure 4. Results of NOx emissions at different speeds in full-load tests
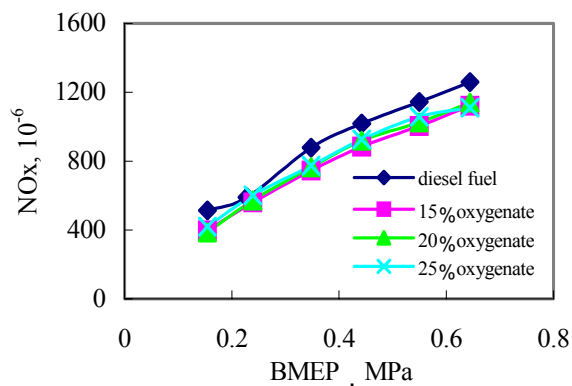

Figure 5. NOx emissions under different partial loads at a speed of 2000 rpm

Figure 4 exhibits plots of NOx emissions as a function of speed for different contents of the compound under full-load conditions. It is apparent that the emitted NOx is only somewhat reduced with the addition of methyl 2-ethoxyethyl carbonate. Under full-load conditions, NOx was reduced absolutely by 151×10^{-6} at 1417 rpm and reduced relatively by 15.9% with maximum at 2300 rpm when adding 15% of the new oxygenate by volume.

Figure 5 reveals the effect of adding methyl 2-ethoxyethyl carbonate on NOx emissions under partial-load conditions. As was the case in the full-load tests, NOx emissions decreased only a little in partial-load tests at each oxygenate content level tested. Under partial-load conditions, NOx reduced absolutely by 139×10^{-6} at 0.55 MPa and reduced relatively by 22.8% with maximum at 0.15 MPa when adding 15%(v) of the new oxygenate.

The impact of the oxygenate addition with different contents on unburned HC emissions in engine exhaust under full-load and partial-load conditions was also measured in the experiments. Unfortunately, at each engine operation mode, unburned HC increased substantially when the engine combusted diesel fuel blends containing different content of methyl 2-ethoxyethyl carbonate. In full-load characteristic, HC emissions were at levels varying from 56×10^{-6} to 110×10^{-6} when the engine was fueled with neat diesel fuel; these values were increased to 11×10^{-6} to 20×10^{-6} when fueled with the fuel blend containing 25% by volume of the new oxygenate. In the tests of partial loads at a speed of 2000 rpm, the emission level varying from 1×10^{-6} to 31×10^{-6} for pure diesel fuel increased by 7×10^{-6} to 24×10^{-6} with 25% by volume of the new oxygenate mixed in diesel fuel. Similar observations of increased HC emissions have been reported for mixes of different oxygenates and diesel fuel in other investigations (7-9). The reason why unburned HC increases is because it is also influenced by many other factors apart from incomplete fuel burning in combustion flame during engine operation. To a large extent, HC emissions also originate from unburned hydrocarbons in the combustion chamber quench layer where the fuel combustion reaction cannot take place due to a much lower temperature. When oxygenate is introduced, the heat value of the diesel fuel blend decreases and consequently engine combustion temperature declines, which not only causes less NOx formation as mentioned above, the level of which correlates with combustion temperature, but also allows the quenched layer thickness to become larger leading to increased HC emissions. Although HC emissions increase when engines are fueled with the oxygenate, their levels are still so low that they are not a crucial factor that need be considered, unlike smoke, CO, and NOx, the reductions of which are currently afforded much more significance worldwide.
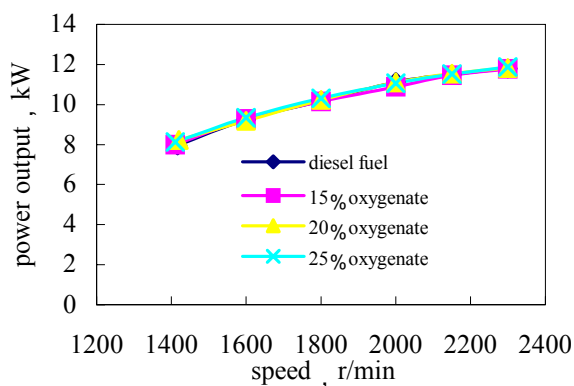

Figure 6. Results of power output in full-load characteristic tests

Figures 6 and 7 display the results of engine power and fuel consumption, respectively, determined in full-load characteristic tests at different speeds. As clearly seen from Figure 6, the power output, for the diesel engine employed, did not change noticeably. Normally, it drops somewhat when fuelling with different oxygenates. Figure 7 shows that fuel consumption increased with the oxygenate content. For this engine, the fuel economy rose by about 2.5% to 5.5% with the fuel blend containing 25% by volume of the oxygenate. Due to

the amount of oxygen contained in the fuel, which reduces the energy released per unit volume, more fuel has to be burned to keep engine power output the same as that obtained by burning pure diesel fuel.
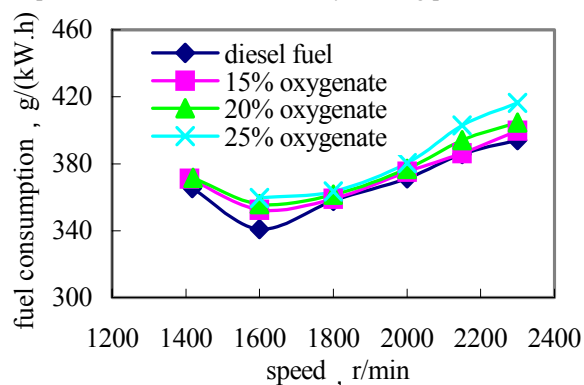

Figure 7. Fuel economy full-load characteristics

Conclusions

(1) A new type of oxygenate, methyl 2-ethoxyethyl carbonate, has been chemically prepared and structurally identified through FTIR, ^{1}H NMR and GC-MS analyses.

(2) Introduction of the substance into diesel fuel lowers exhaust emissions significantly. For an engine operating under full-load conditions, CO is reduced by 29.2% to 40.5% when diesel fuel is doped with 25% by volume of the oxygenate. NOx is decreased by 15.9% from the maximum when diesel fuel is doped with 15% of it.

(3) For the same engine operating under partial-load conditions at a speed of 2000 rpm, CO and smoke decrease substantially with increasing load. CO is reduced by 46.7% to 69.4%, smoke reduced by 50% from the maximum when diesel fuel is doped with 25% by volume of the oxygenate; NOx is reduced by 22.8% to the maximum when diesel fuel is doped with 15% of it. HC emissions increase substantially under both full-load and partial-load conditions, but they are still low enough not to be an important environmental factor compared to other types of emissions.

(4) For the engine working under full-load conditions, power output does not drop noticeably, while fuel consumption increases by 2.5% to 5.5% with diesel fuel containing 25% by volume of the new oxygenate.

References
1. Liotta F J J, Montalvo D M., SAE Paper 932734, 1993
2. Murayama T, Zheng M, Chikahisa T, et al, SAE Paper 952518,1995
3. Huang Yongchneg , Wang Hewu, Zhou Longbao, Bai Fucheng, Journal of Xi'an Jiaotong University, 2000, 34 (5), 5
4. Wang Hewu, Zhou Longbao, Transactions of CSICE, 2001, 19 (1), 1
5. Shi Kefeng, Pan Keyu, Li Jianguo, Yao Bo, Shen Ruoyu, Transactions of CSICE, 2004, 22 (3), 221
6. Hejun Guo, Xianxiang Huang, Xuanjun Wang, Zhili Zhang, Prepr. Pap. - Am. Chem. Soc., Div. Pet. Chem.,224, 49 (2), 232
7. Lu Xingcai, Zhang Wugao, Huang Zhen, Transactions of CSICE, 2004, 22 (3), 210
8. Zhang Wugao, Yang Jianguang, Li Shuze, and Huang Zhen, Automotive Engineering, 2003, 25 (4), 334
9. Lu Xingcai, Huang Zhen, Zhang Wugao, and Yang Jianguang, Transactions of CSICE, 2004, 22 (1), 193

INVENTORY OF COMBUSTION EMISSIONS OF POLYCHLORINATED DIBENZO-P-DIOXIN (PCDD) AND POLYCHLORINATED DIBENZOFURANS (PCDF) IN THE UNITED STATES

David H. Cleverly

National Center for Environmental Assessment (8623N)
Office of Research and Development
U.S. Environmental Protection Agency
1200 Pennsylvania Ave., NW
Washington DC, 20460

Introduction

PCDDs and PCDFs represent a class of aromatic hydrocarbons consisting of a triple-ring structure of two benzene rings interconnected by a third oxygenated ring. Theoretically 75 PCDD and 135 PCDF are possible, and their physical chemical properties are determined by the number of chlorine atoms and their respective positions on the molecular nucleus. Figure 1 displays the chemical structure of PCDDs and PCDFs. There are eight positions whereby a hydrogen atom can be substituted by a chlorine atom.
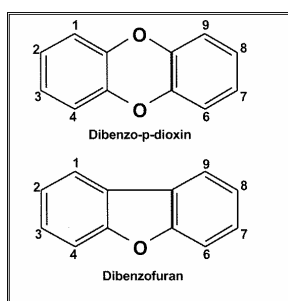

Figure 1. Chemical structure of dibenzo-p-dioxin and dibenzofuran

The environmental effects and toxicology of PCDDs/PCDFs is largely mediated and controlled by the presence of chlorine atoms in the 2,3,7,8 positions. There are 7 PCDDs and 10 PCDFs with this substitution pattern. In most instances, PCDDs and PCDFs appear as mixtures in environmental samples. The Toxic Equivalence (or TEQ) procedure is an accepted convention for translating the proportion of congeners within the mixture to an equivalent concentration of 2,3,7,8-TCDD (the most toxic member of the class).[1] The simplicity of this approach is to allow for the assessment of the approximate toxicity of the mixture.

In order to identify the sources of PCDDs and PCDFs, the USEPA has conducted an inventory of all known source activities in the U.S.[2] The dioxin inventory originally presented estimates of environmental releases for the years 1987 and 1995. Currently the USEPA is updating the inventory to incorporate releases for the year 2000. The inventory allows for the observation of environmental time-trends, and for the ranking of sources by magnitude of release. The dioxin inventory has consistently shown that the dominant sources of PCDDs and PCDFs to the environment are combustion sources. PCDDs and PCDFs are formed in the cool down zone of combustion sources either from the oxidation of carbon, or from precursor compounds.[3] The former has been referred to as *de Novo* synthesis, which consists of heterogeneous formation as surface catalyzed reactions at temperatures from $200^0 - 400^0$C. The latter is the result of homogenous reactions in the gas phase at temperatures from $500^0 - 800^0$C. Both processes require the presence of a transition metal catalyst and a source of chlorine. Most fuels are capable of forming PCDDs and PCDFs when combusted. The following is a summary of PCDD/PCDF emissions from a variety of combustion sources from USEPA's dioxin inventory.

Methods

The initial steps to constructing the dioxin inventory were to categorize combustion sources on the basis of types of combustion technology and types of fuel combusted. The assumption to this is that similar technologies combusting similar fuels will have similar emissions of PCDDs and PCDFs. Combustion categories were further subcategorized based on utilization of specific types of air pollution control devices (APCD). The type of APCD does impact the amount of PCDD/PCDF that is released from the stack. Engineering reports on the results of detecting PCDDs and PCDFs from the stacks of particular combustion source technologies were collected and evaluated in terms of fitting within a particular combustion source category. Figure 2 illustrates this point. The key aspect to this is the creation of homogeneous categories supported by similarity in design, function, process, and utilization of feeds and fuels. Superimposed on this is the dynamics of air pollution control in terms of efficiency in capturing and reducing PCDDs and PCDFs in combustion gases prior to leaving the stack.
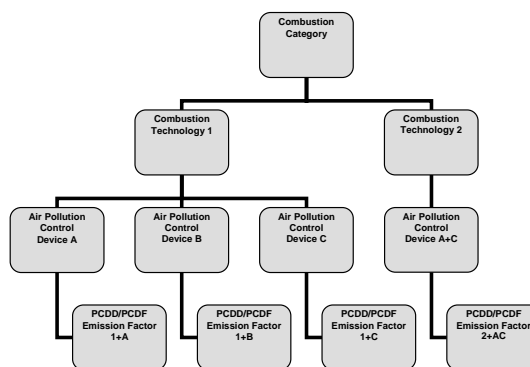

Figure 2. Example of classification scheme employed to estimate PCDD and PCDF emission factors.

Another important aspect to estimating annual releases of PCDD/PCDF was the development an emissions profile representative of the combustion category. To accomplish this, stack gas emissions of PCDD/PCDF were normalized on the basis of mass TEQ emitted per mass or volume of fuel combusted or materials processed, e.g., g TEQ emitted /kg of fuel; g TEQ emitted/L fuel; g TEQ emitted/kg of materials processed. Such units are referred to as emission factors, and they permit comparisons to be made across different technologies. Emission factors are helpful for calculating annual total emissions of PCDD and PCDFs either from individual facilities or from a group of similar technologies. In some cases most every member of the combustion technology category had been stack tested for emissions of PCDDs and PCDFs and this produced highly representative emission factor. In the other extreme where only a few facilities had been tested estimates of annual emissions were derived from extrapolating emission factors of tested facilities to untested facilities. This process introduced uncertainty in estimating emissions from the source. Table 1 is a summary of TEQ emission factors for various combustion sources representative of source activities in the year 2000.

Table 1. TEQ emission factors for combustion sources

Source Category	Source Subcategory	Source Subcategory	TEQ	Emission Factor Units
Waste Incineration	Municipal waste combustion		2.82	ng TEQ/kg waste combusted
Waste Incineration	Hazardous waste incineration		2.13	ng TEQ/kg waste combusted
Waste Incineration	Boilers/industrial furnaces		1.21	ng TEQ/kg waste combusted
Waste Incineration	Halogen acid furnaces		0.84	ng TEQ/kg waste feed
Waste Incineration	Medical waste / pathological incineration		630.00	ng TEQ/kg waste combusted
Waste Incineration	Crematoria	Human	434.00	ng TEQ/body
Waste Incineration	Crematoria	Animal	0.12	ng TEQ/kg animal
Waste Incineration	Sewage sludge incineration		6.74	ng TEQ/kg dry sludge combusted
Power/Energy Generation	Vehicle fuel combustion, unleaded gas	Unleaded gas	1.60	pg TEQ/km driven
Power/Energy Generation	Vehicle fuel combustion, diesel	Diesel	182.00	pg TEQ/km driven
Power/Energy Generation	Wood combustion	Residential	0.50	ng TEQ/kg wood combusted
Power/Energy Generation	Wood combustion	Industrial	0.60 - 13.2	ng TEQ/kg wood combusted
Power/Energy Generation	Coal combustion	Utility	0.08	ng TEQ/kg coal combusted
Power/Energy Generation	Coal combustion	Residential	2 - 7.5	ng TEQ/kg coal combusted
Power/Energy Generation	Oil combustion	Industrial/utility	0.23	ng TEQ/L oil combusted
Other High-temperature Sources	Cement Kilns	Hazardous waste	1.11 - 30.70	ng TEQ/kg clinker produced
Other High-temperature Sources	Cement Kilns	Non-hazardous waste	0.26	ng TEQ/kg clinker produced
Other High-temperature Sources	Lightweight aggregate kilns		1.99	ng TEQ/kg waste feed
Other High-temperature Sources	Petroleum refining catalyst regeneration		1.59	ng TEQ/barrel reformer feed
Other High-temperature Sources	Kraft recovery boilers		0.03	ng TEQ/kg solids combusted
Other High-temperature Sources	Hot mix asphalt		0.00	ng TEQ/kg waste combusted
Minimally Controlled Combustion	Backyard barrel burning		76.80	ng TEQ/kg waste combusted
Minimally Controlled Combustion	Land clearing		20.50	ng TEQ/kg biomass
Minimally Controlled Combustion	Yard waste combustion		20.50	ng TEQ/kg biomass
Minimally Controlled Combustion	Prescribed burning		20.50	ng TEQ/kg biomass
Minimally Controlled Combustion	Forest fires		20.50	ng TEQ/kg biomass
Metallurgical Processes	Ferrous metal sintering		0.62 - 4.61	ng TEQ/kg sinter

Results and Discussion

The annual emissions of TEQ (g/yr) were estimated by multiplying the TEQ emission factor by the annual amount of fuel combusted or materials that were processed by the combustion facility. This was done for all members of the combustion category. The sum of these calculations produced an estimate of g TEQ emitted for each combustion technology in years 1987, 1995 and 2000. Figure 3 is a summary of the TEQ annual emissions from combustion sources for the years 1987, 1995 and 2000.
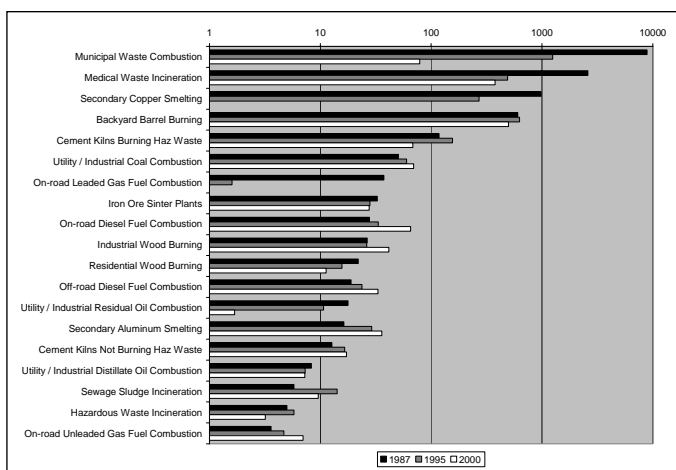

Figure 3. TEQ emissions from combustion sources for years 1987, 1995 and 2000

The USEPA dioxin inventory indicates that the annual TEQ releases to the environment from all reasonably quantifiable sources were approximately 1,549 g, 3,281 g and 13,961 g in the year 2000, 1995, and 1987, respectively Of the 1,549 g TEQ emitted from all sources to the U.S. environment in the year 2000, 1422 g TEQ (92%) were from combustion sources. Between 1987 and 2000, there was approximately an 89% reduction in total TEQ releases to the U.S. environment. In 1987 and 1995, the leading sources of TEQ emissions to the U.S. environment were municipal waste combustors. However, by 2000, the leading source of TEQ emissions was the uncontrolled and open burning of residential refuse in backyard barrels. Technological improvements in controlled combustion technology, operation and air pollution control devices are responsible for the decreases in TEQ emissions over time. For examples, between 1987 and 2000 there was approximately a 99% decrease in PCDD and PCDF emissions from municipal solid waste incineration; a 85% reduction from medical waste incineration and a 42% reduction from cement kilns burning hazardous waste. However, uncontrolled combustion remains an important source of TEQ emissions to the open and circulating environment.

References

1. Van den Berg,M: Birnbaum,L; Albertus Bosveld, T.C.; Brunström, B; Cook, P; Feeley, M; Giesy, J. P.; Hanberg, A; Hasegawa, R; Kennedy, S.; Kubiak, T ; Larsen, J ; van Leeuwen, F.X.; Liem, A.K.;Cynthia Nolt, Peterson, R; Poellinger, L; Safe, S; Schrenk, D ; Tillitt, D; Tysklind, M; Younes, M; Wærn, F; Zacharewski, T . Toxic Equivalency Factors (TEFs) for PCBs, PCDDs, PCDFs for Humans and Wildlife. Environ Health Perspect. 1998 Dec;106(12): p.775-92.
2. The Inventory Of Sources Of Dioxin In The United States. National Center for Environmental Assessment,U.S. Environmental Protection Agency, EPA/600/P-98/002Aa, April 1998.
3. Stanmore, B.R. 2004. Combustion and Flame 136:p. 398-427.

COMPARISON OF NITRO-POLYCYCLIC AROMATIC HYDROCARBON LEVELS IN CONVENTIONAL DIESEL AND ALTERNATIVE DIESEL FUELS

Crystal D. Havey[1], R. Robert Hayes[2], Robert L. McCormick[3], and Kent J. Voorhees[1]

[1]Colorado School of Mines, Department of Chemistry and Geochemistry, 1500 Illinois St, Golden, CO 80401
[2]Renewable Fuels and Lubricants Research Laboratory, National Renewable Energy Laboratory, 1980 31st St., Denver, CO 80216
[3]Center for Transportation Technologies and Systems, National Renewable Energy Laboratory, 1617 Cole Blvd., Golden, CO 80401

Introduction

Use of alternative fuels for diesel engines, such as synthetic diesel and biodiesel, has the potential to reduce petroleum consumption and thus dependence on foreign imports. If the alternative fuels are produced from highly renewable sources, they lower life-cycle greenhouse gas emissions. They are also known to cause a significant reduction in certain regulated pollutant emissions: CO, NO_x, hydrocarbons, and particulate matter (PM). Ideally these emissions reductions will correspond to a decrease in the environmental risks and health hazards associated with diesel engine exhaust. Compounds, such as nitro-polycyclic aromatic hydrocarbons (NPAHs), while unregulated, are also known to pose health and environmental hazards. Measurement of the levels of NPAHs in exhaust from alternative and conventional fuels allows for evaluation of alternative fuel usage effects on emission of these unregulated toxic compounds.

Negative ion chemical ionization (NICI) has been used for the detection of NPAHs in diesel soot.[1] In NICI analysis, both solid phase extraction and LC fractionation were necessary to obtain desired results. A novel ionization source containing a trochoidal electron monochromator has been developed previously[2] and has been used here for analysis of diesel fuel emissions. This source allows for both electron capture and dissociative electron capture to be carried out using very controlled electron energies ($\pm 0.3 eV$). NPAHs have a strong ability to undergo electron capture at near-0eV producing molecular ions, and can also be subject to dissociative electron capture at 3.5eV producing an NO_2^- fragment.

Incorporation of the trochoidal electron monochromator source into a mass spectrometer system creates a sensitive and selective technique for detection of NPAHs in complex matrices. The high selectivity of the electron monochromator-mass spectrometer (EM-MS) allowed for minimal sample cleanup in order to achieve desired results. Comparisons will be presented of the NPAH content, as measured by EM-MS, in the emissions produced from a modern production diesel engine running on conventional and alternative diesel fuels.

Experimental

Diesel Samples. Test fuels presented here include a conventional diesel fuel and a 50% blend of biodiesel and conventional diesel. The fuels were run in a 2002 Cummins ISB 300 engine. It is a modern engine with cooled-EGR, high-pressure common rail injection, and a variable geometry turbocharger designed to meet the EPA 2004 regulated emissions requirements. The engine was run on the federal Heavy-Duty Transient Cycle, which is used for EPA certification of engines. The PM was collected onto 47mm Teflon-coated glass fiber pads located in line.

Sample Extraction and Cleanup. Internal standards (1-nitronaphthalene-d7, 4-nitrobiphenyl-d9, 1,5-dinitronaphthalene-d6, 9-nitroanthracene-d9, 3-nitrofluoranthene-d9 from CDN Isotopes, Pointe-Claire, Quebec, Canada and 1-nitropyrene-d9 from Cambridge Isotope Laboratories, Andover, MA) were spiked onto the filter pads of certain samples for quantitative purposes. The PM was extracted off of the filter pads using dichloromethane (Mallinckrodt UltimAR universal grade, Phillipsburg, NJ). The samples were placed on a shaker table for one hour. Once the filter was removed from the sample solution, hexane (HPLC grade, Mallinckrodt, Phillipsburg, NJ) was added to create a 20:80 dichloromethane:hexane mix. Solid phase extraction was carried out on aminopropyl solid phase cartridges (Alltech Assoc., Inc., Deerfield, IL), with the 20:80 mix driving polar interferences from the sample onto the phase.[1] The samples were then concentrated down to approximately 100µL, using toluene (HPLC grade, Mallinckrodt, Phillipsburg, NJ) as a keeper.

Instrumentation. A JEOL MStation JMS-700T mass spectrometer equipped with a JEOL trochoidal electron monochromator ionization source was used for all analyses. For each sample, one microliter was injected onto a Hewlett Packard 6890 Series GC system, equipped with an on-column injection port. A 30m RTX-5Sil MS column (Restek Corp, Bellefonte, PA), i.d. 0.25mm, was used to obtain desirable separation of the NPAHs. EM-MS analysis was carried out using selected ion monitoring (SIM) of m/z 46 for the NO_2^- fragment at 3.5eV for identification of each compound by retention time. SIM monitoring of the molecular ions at near-0eV was used for confirmation of the individual compounds.
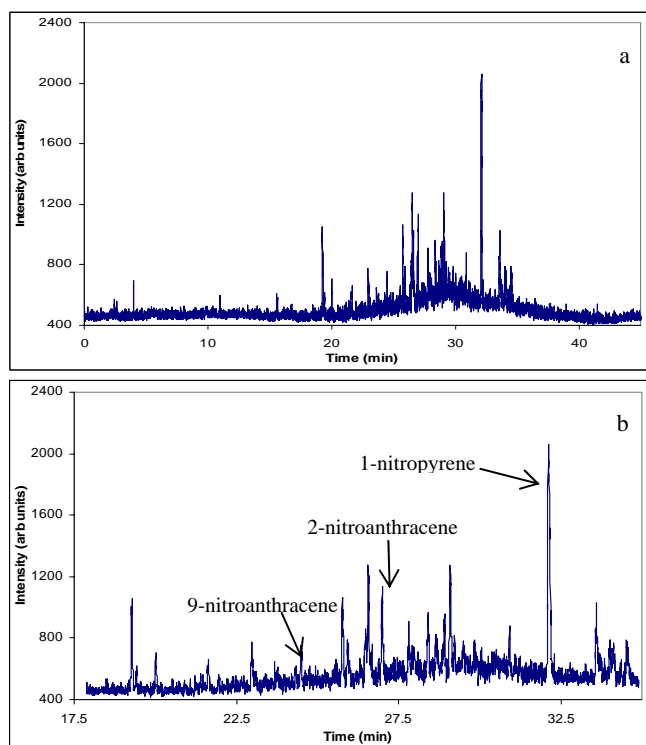

Figure 1. SIM chromatogram (m/z 46) of a conventional diesel sample a) full scale and b) expanded for detail.

Results and Discussion

Results obtained for conventional and biodiesel samples are presented here. Figure 1 shows a SIM chromatogram of m/z 46 of a conventional diesel sample (no internal standards were used). Peaks of 2-nitroanthrancene, 9-nitroanthracene, and 1-nitropyrene have been identified based on retention times. Further analysis of the molecular ions (Figures 2 and 3) confirmed these assignments.

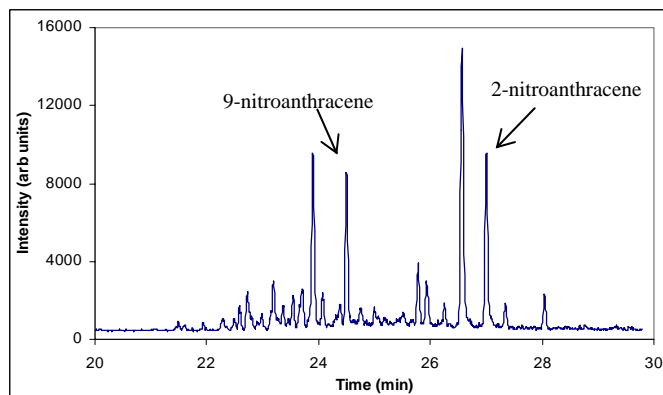Figure 2 also contains indications of other nitroanthracene isomers and/or isomers of nitrophenanthrene.

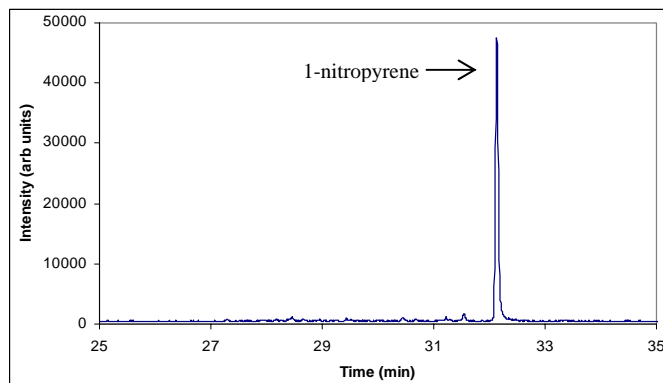**Figure 2.** SIM chromatogram (m/z 223) of a conventional diesel sample.

Figure 3. SIM chromatogram (m/z 247) of conventional diesel sample.

An m/z 46 SIM chromatogram of a biodiesel sample (with internal standards) is shown in Figure 4. The 6 large peaks in the chromatogram are the internal standards. No other peaks were observed at a detectable level. These results are very preliminary and additional analyses need to be conducted in order to be conclusive of these observations. It is possible that NPAHs potentially present in the sample are being masked by the internal standards. Adjustment of internal standard content as well as concentration is under review to optimize the use of the internal standards.
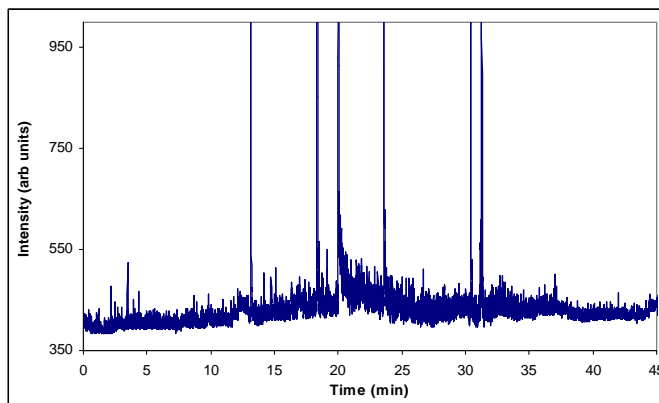

Figure 4. SIM chromatogram (m/z 46) of biodiesel sample.

Conclusions

Preliminary studies of NPAH content in conventional and biodiesel emissions have been compared. The use of an electron monochromator as the ionization source for the mass spectrometer allowed for minimal sample cleanup in order to obtain results with little interference. Further work is being conducted on a gas to liquids (GTL) synthetic diesel fuel made by the Fischer-Tropsch (FT) process and blends with various levels of FT fuel combined with more conventional refinery diesel fuel. Qualitative and quantitative comparisons will be made of all samples to provide insight on the effect of alternative fuels on production of NPAHs in diesel emissions.

References
1. Bamford, H. A.; Bezabeh, D. Z.; Schantz, M. M.; Wise, S. A.; Baker, J. E. *Chemosphere.* 2003, 50, 575.
2. Laramée, J. A.; Kocher, C. A.; and Deizner, M. L. *Anal. Chem.* 1992, 64 (20), 2316.

EFFECTS OF JET FUEL AROMATIC CONCENTRATION ON THE EMISSIONS OF A T63 ENGINE

Orvin Monroig[1], Edwin Corporan[1], Matthew J. DeWitt[2], Ben Mortimer[2], David Ostdiek[2], and Matt Wagner[1]

[1] Air Force Research Laboratory/Propulsion Directorate
1790 Loop Rd. N. Bldg. 490, WPAFB, OH 45433-7103

[2] University of Dayton Research Institute
300 College Park Dayton, OH 45469-0116

Introduction

Jet fuels are comprised of a wide range of hydrocarbon compounds with varying functionalities. Although there can be hundreds or thousands of individual compounds within the fuel, the components can be grouped into four primary classes: paraffins, aromatics, cycloparaffins, and olefins. The proportions in which these types of compounds are present largely define the physical and chemical characteristics of the fuel[1]. The aromatic content has been shown to have a strong effect on these characteristics. For example, the total aromatic content can simultaneously affect the overall fuel density (physical) and the hydrogen-to-carbon ratio (H/C) (chemical); this latter characteristic has been shown to influence the combustion efficiency. Aromatics have also been recognized as soot precursors during the combustion process as they promote polycyclic aromatic hydrocarbon (PAH) growth and subsequent particulate matter (PM) production[2]. This is important because particle emissions from stationary and mobile combustion sources are regulated by the EPA. Separate standards exist for the allowable quantity of particulate matter emissions of "coarse particles" that range from 2.5 to 10 micrometers in diameter (PM10) and fine particles less than 2.5 micrometers in diameter (PM2.5). Therefore, reduction of soot emissions can provide environmental benefits that satisfy regulatory requirements.

Increased understanding on the role of aromatics in the formation of PM would greatly assist in the development of strategies to reduce PM emissions from turbine engine combustors. Though aromatics have been shown to promote PM production, as previously stated, large-scale investigation with actual fuels with varying aromatic concentration is difficult due to changes to other properties. Therefore, a study was conducted to independently assess the impacts of aromatic content in jet fuel on particle emission production on an actual turbine engine.

Experimental

Baseline Fuel. A natural gas derived synthetic jet fuel (synjet) was used as the baseline fuel for this study. The synjet provided an aromatic-free jet fuel with similar chemical characteristics (hydrocarbon range) and physical properties as Jet A-1 or JP-8[3]. The fuel is comprised primarily of branched and linear alkanes, with zero aromatic and heteroatomic content.

Aromatic Blend. The aromatic blend was formed by a combination of three different aromatic solvent produced by Exxon (100, 150, and 200). This approach was employed rather than the addition of a single-component since the mixture was believed to be more representative of the range of aromatic components within actual jet fuels. To help determine the appropriate ratio of solvents for the aromatic blend, an extraction of the aromatic components was conducted on two JP-8 samples using high pressure liquid chromatography (HPLC). The extractions were then analyzed by Gas

chromatography/mass spectrometry (GC/MS) to quantify the individual species and to determine the molecular weight distribution of the aromatic components. Each solvent was also separately analyzed by GC/MS for identification and quantitation of its components. A comparison of the aromatic fraction extracted from a JP-8 fuel and that obtained from the aromatic blend is shown in **Figures 1** and **2**. Based on this analysis, the appropriate blend ratio of the three solvents was obtained to provide an overall aromatic distribution similar to that in a typical JP-8. Overall, 25, 53, and 23 percent of the Exxon 100, 150 and 200 aromatic solvents respectively were found to provide the best match to the desired distribution without significantly altering the overall volatility of the mixture. The aromatic blend was added to the synjet fuel at concentrations of 5, 10, 15, 20 and 25 percent by volume to evaluate the sensitivity of particulate emissions to the concentration of aromatics in the fuel.
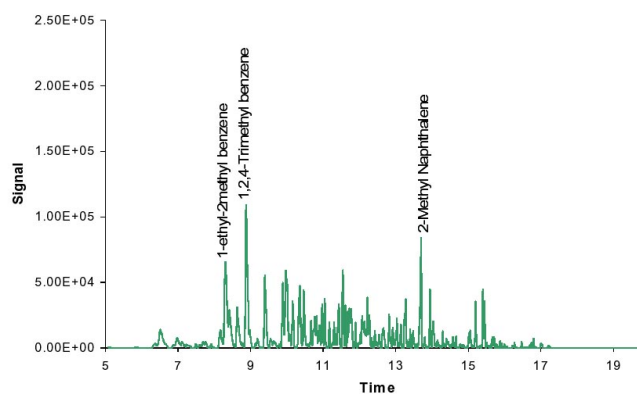

Figure 1. Gas chromatogram for HPLC extraction of aromatic fraction in JP- 8
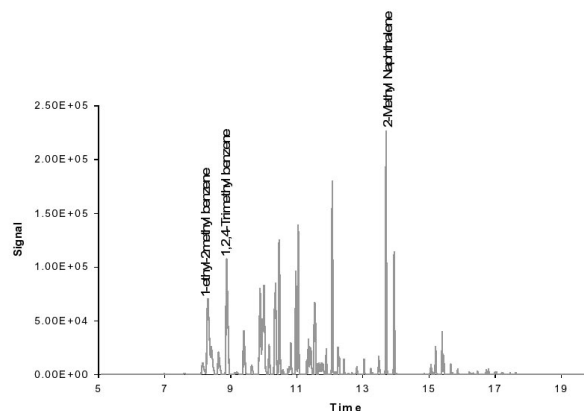
Figure 2. Gas chromatogram for the aromatic blend

T63 Engine and Fuel System. A T63-A-700 turboshaft engine, used primarily in helicopter applications, was used in this study. The engine is located in the Engine Environment Research Facility (EERF) in the Propulsion Directorate at Wright-Patterson Air Force Base, and is used to evaluate turbine engine lubricants, fuels, and sensors in an actual engine environment.

The synjet fuel was supplied to the T63 from an external tank. The aromatic blend was injected via two ISCO Model 1000D syringe

pumps immediately downstream of the fuel flow meter. The required aromatic flow rate was computed from the measured fuel flow rate and the target aromatic concentration. The synjet/aromatic blend passed through a static mixer to ensure a homogeneous mixture at the engine fuel nozzle. For evaluation of the 25% aromatic concentration, the blend and synjet were premixed in the external tank due to capacity limitation with the injection pumps.

The engine was operated at idle and cruise conditions. For these experiments the fuel flow rate was adjusted to maintain a constant turbine outlet temperature. This approach assured the best run-to-run repeatability in these combustion tests.

Sampling Method. Particulate emissions from the T63 engine were captured and transported to the analytical instruments via an oil-cooled probe installed facing the flow in the center and near the exit of the engine to help capture a "representative" sample of the engine exhaust and avoid diluting or contaminating with surrounding air. . The probe design is based on an AEDC/NASA/UMR design and consists basically of three concentric tubes with three fluid passages. The outermost passage flows the recirculating cooling oil, the middle passage provides particle free dilution air (which is injected into the sample stream at the probe tip), and the center passage transports the diluted sample to the instruments. The exhaust sample is diluted with dry air at the tip of the probe to prevent water condensation and particulate loss to the wall due to high wall-sample temperature gradients, and to prevent saturation of the particulates instrumentation. The diluted sample was drawn into the analytical instruments via a vacuum pump, and the air dilution and sample flows were controlled with highly precise flow controllers. Due to the high particulate count from this engine, dilution rates of 94-98% were used (only 2-6% of the sample from the exhaust entered the analyzers).

Instrumentation. Commercially available aerosol instruments were used to measure particle number density, the particle size distribution and the particulate mass concentration. Specifically, emissions were characterized using a TSI Model 3022A Condensation Nuclei Counter (CNC) and a MetOne Model 237B Laser Particle Counter (LPC) to provide a count of particles per unit volume (particle number density), a TSI Model 3936 Scanning Mobility Particle Sizer (SMPS) to obtain a particle size distribution and a Rupprecht & Pataschnick Series 1105 Tapered Element Oscillating Microbalance (TEOM) to obtain real-time particulate mass emissions. Furthermore, an in-house developed smoke machine was used to collect particulate samples on quartz and paper filters for subsequent analysis. This included determination of engine smoke number, quantitation of the PM mass, qualitative soot composition via temperature programmed oxidation, and identification and quantitation of the absorbed polycyclic aromatic hydrocarbons (PAH) via gas Chromatography/mass Spectrometry (GC/MS). Major and minor gaseous emissions were quantified using a Fourier Transform Infrared (FTIR) analyzer. Discussions in this paper will focus only on the particle number density, size distribution, mass and smoke number data. The remaining data analysis will be covered in a subsequent publication.

Results and Discussion

Test results for both engine conditions showed a strong correlation of the particulate emissions to the overall aromatic concentration in the blend. Higher absolute particulate production was observed at cruise due to the higher rates of PAH and soot formation as the result of higher combustion temperatures and pressures. As shown in **Figure 3,** there was a significant increase in the particle number density (PND) at both engine conditions relative to combustion with the neat synjet fuel. The relation of PND

increase with aromatic concentration was fairly linear for both conditions; however, the increase was significantly more notable at the idle condition. This could be due to several reasons. Increased soot nuclei, initiated by the increased aromatic species in the fuel, may have passed through the combustor without completely combusting due to the lower temperatures found at idle, or the CNC may have counted fine semi-volatile particles from uncombusted or pyrolyzed aromatic compounds. GC/MS analyses of the soot samples may provide insight into these dramatic increases in particle concentration at idle with the aromatics.
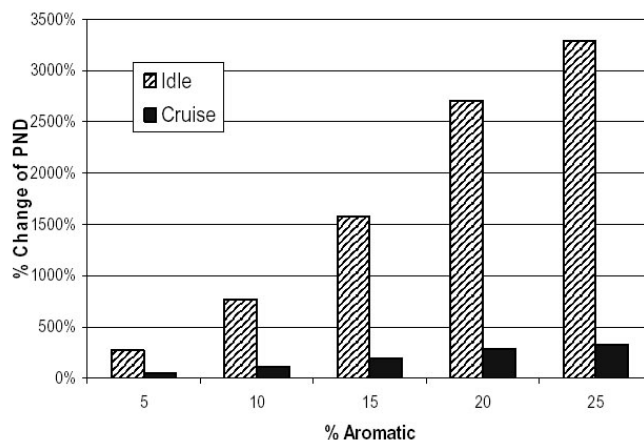

Figure 3. Changes in particle number density as a function of fuel aromatic concentration at idle and cruise conditions in T63 engine

The particle size distribution for the idle and cruise conditions are shown in **Figures 4** and **5**. The data indicate that although there was an increase in the total particle number density with the higher aromatic content, the relative shape of the distribution was not altered. This implies that the aromatics most likely affect the initial formation of the PM precursors (e.g., PAHs), but do not significantly alter the growth mechanism. The shift in the particle size distribution to the right as the aromatic concentration increased, suggests that the larger number of particles due to the increased aromatics, underwent coagulation and growth reactions, leading to increases in the mean particle size. This behavior is more evident at cruise due to the relatively high concentration of particles.
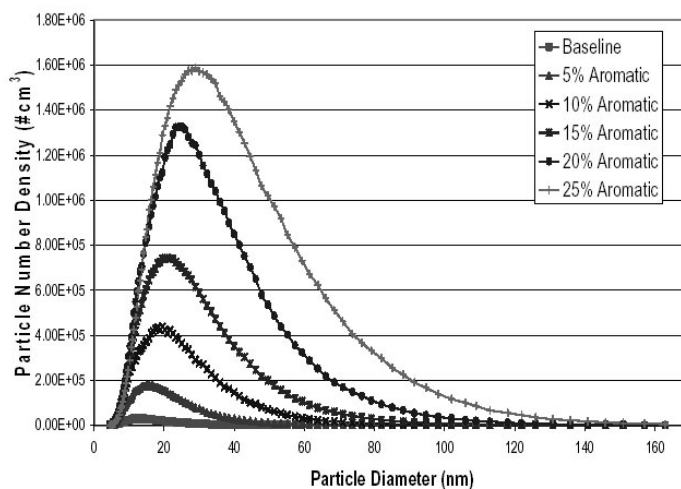

Figure 4. Particle size distribution at idle condition with varying aromatic concentration in the synjet fuel
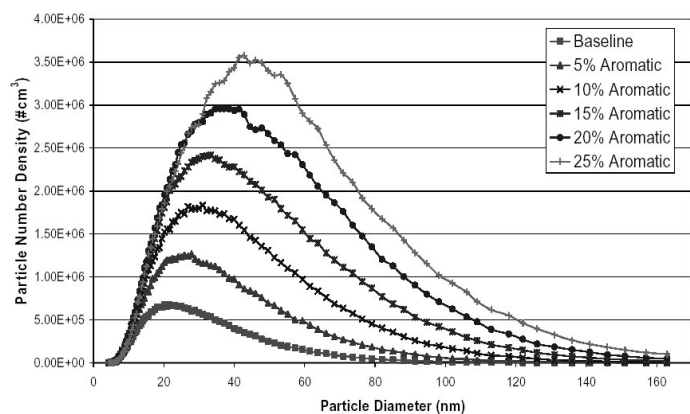
Figure 5. Particle size distribution at cruise condition with varying aromatic concentration in the synjet fuel

The smoke numbers for the tests conducted as a function of fuel aromatic concentration for both engine conditions are shown in **Figure 6**. As expected, the smoke numbers were significantly higher for cruise than for idle. The smoke number increased linearly with the aromatic concentration for the cruise condition, and showed significant increases with aromatics at idle. These trends are in good qualitative agreement with the particle number and size distribution data.
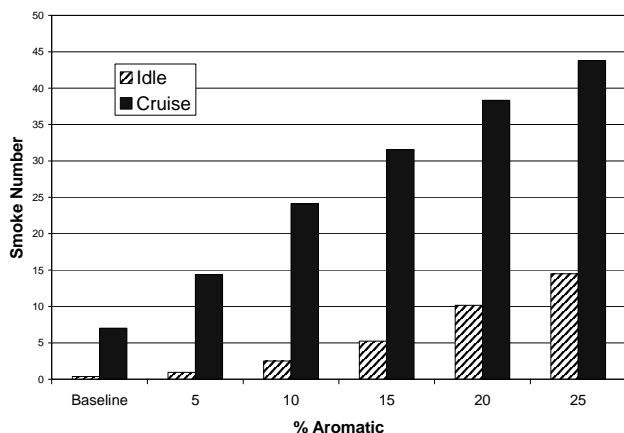

Figure 6. Smoke number at idle and cruise condition with different aromatic concentration.

Particle Mass Emissions. The particle mass emissions measured with the TEOM for the different concentrations of aromatics are shown in **Figure 7**. As shown, the mass emissions trends as a function of aromatic concentrations are similar to those of the smoke number. For the idle condition, although increases in mass were measured with increased aromatics, the low particle mass loading on the TEOM filter increased the uncertainty in the measurement and thus, precluded an accurate trend as a function of aromatics.

Gaseous emissions. The aromatics were observed to have negligible effect on the primary gaseous emissions; specifically, the CO, CO_2, and NO_x. Subsequent analysis of soot filters will provide more insight into the volatile hydrocarbons species that were not quantified with the gaseous emissions system. These results will be published in a future publication.
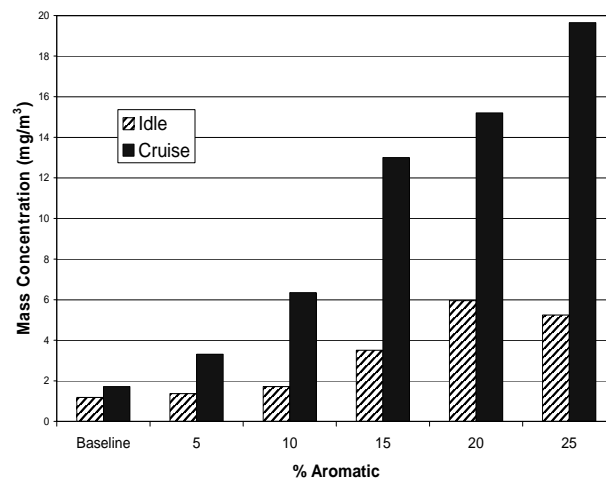

Figure 7. TEOM Mass concentrations as a function of aromatic concentration

Conclusions

The effects of fuel aromatic content on the emissions of a T63 engine were studied. A natural gas derived synthetic jet fuel (synjet), used as the baseline fuel, was doped with a blend of aromatic solvents at different concentrations to simulate the aromatic components in a typical jet fuel. Results show that the addition of aromatics had negligible impacts on gaseous emissions from the T63 engine. As expected, for both engine conditions, strong correlations of higher particle emissions as a function of aromatic concentration were observed. The increases in particle number relative to the baseline fuel were significantly higher for idle than for cruise, likely because of increased soot nuclei or uncombusted (or pyrolyzed) aromatic species. Significant increases in particle mean diameter and smoke number were also observed with the increase in aromatics for both conditions. This study clearly shows the sensitivity of soot emissions to aromatic concentration, and further demonstrates the strong influence of aromatics on engine soot/particulate emissions from actual turbine engines.

References

Lefebvre, A. H., 1983, "Gas Turbine Combustion," 1st Edition.
1. Ritcher H., Howard J.B., "Formation of Polycyclic Aromatic Hydrocarbons and Their Growth to Soot-A Review of Chemical Reaction Pathways," Prog. Energy and Comb. Sci. 26 (2000) 565-608.
2. Edwards, J.T., Minus, D., Harrison, W., Corporan, E., DeWitt, M., Zabarnick and S., Balster, L., "Fischer-Tropsch Jet Fuels-Characterization for Advanced Aerospace Applications," AIAA Paper 2004-3885.

REDUCTION OF TURBINE ENGINE PARTICULATE EMISSIONS USING SYNTHETIC JET FUEL

Edwin Corporan[1], Matthew J. DeWitt[2], Orvin Monroig[1], David Ostdiek[2], Ben Mortimer[2] and Matt Wagner[1]

[1] Air Force Research Laboratory/Propulsion Directorate
1790 Loop Rd. N. Bldg. 490, WPAFB, OH 45433-7103

[2] University of Dayton Research Institute
300 College Park Dayton, OH 45469-0116

Introduction

Mobile and stationary combustion sources are major contributors of particulate matter emissions. In 1997, the US Environmental Protection Agency (USEPA) set a new air quality standard for airborne fine particulate matter (PM) with diameter of 2.5 μm or less (PM2.5) [National Research Council, 1998]. This PM2.5 standard was established based on human health studies that showed the previous PM standard for particulate matter with diameters of 10 μm or less (PM10) was insufficient to address the harmful effects caused by these smaller particles. The more stringent environmental standards imposed by the USEPA have increased interest into the research and development of solutions to better characterize and reduce PM emissions from combustion sources. Solutions ranging from technological improvements to engines, including improved fuel injection or combustion concepts, to chemistry-based techniques, such as the use of fuel additives, blends and/or fuel reformulation, are being considered by engine manufacturers and research organizations. Although soot emissions from combustion sources have been studied extensively for many years, the chemical and physical processes that control the formation of nascent soot particles are still poorly understood [Ritcher and Howard, 2000]. However, it is widely recognized that the aromatic species in the fuel play a major role in the formation of large polycyclic aromatic hydrocarbons (PAH) and eventual soot nuclei. It has been postulated that the PAH species grow via reactions with stable and radical species including single-ring aromatics, other PAH and C_2-C_4 radicals to form larger PAH molecules. The growth of these multi-ring species leads to the nucleation of small soot particles which subsequently undergo growth by coagulation and mass addition.

Due to the influential role of aromatics in the initial PAH formation, the reduction of the fuel aromatic concentration by either improved processing or blending with a low or zero aromatic fuel will most likely result in a reduction in soot emissions. However, recent studies exploring the effects of biodiesel (zero aromatic) as a fuel extender in JP-8 showed only marginal reductions in particulate emissions despite reducing aromatics by up to 20% by volume [Corporan, 2004]. This was attributed to the inefficient combustion and subsequent decomposition of the large molecular weight biodiesel compounds, which underwent molecular growth reactions to form hydrogen-deficient molecules and eventual soot, thereby offsetting the benefits of reduced aromatics. Reductions in particulate emissions would be realized if the blend fuel was more similar to the base components in JP-8. Accordingly, the present study was performed with a zero-aromatic synthetic jet fuel (synjet) comprised of normal and branched paraffins with a molecular weight distribution similar to JP-8. The fuel was tested neat and at several blend ratios with JP-8 to study its potential to reduce particulate emissions relative to the JP-8 fuel. Previous research has demonstrated the potential of

synthetic jet fuel to provide more thermally-stable and cleaner-burning fuels than current petroleum-derived JP-8 [Edwards, 2004]. In addition to the potential environmental benefits, synthetic jet fuels (natural gas or coal derived) may reduce future fuel costs and foreign oil dependency. Considering that the United States consumes approximately 26 billion gallons of jet fuel per year, the use of jet fuels containing even small amounts of synthetic fuel could translate into significant reductions in the use of petroleum-based crude oil.

Experimental

T63 Engine and Fuel System. The synthetic jet fuel emissions assessment was conducted on a T63-A-700 turboshaft engine. The helicopter engine is located in the Engine Environment Research Facility (EERF) in the Propulsion Directorate at Wright-Patterson Air Force Base, and is used to evaluate turbine engine lubricants, fuels, fuel additives, and sensors in an actual engine environment. A detailed description of the engine is provided in an earlier publication [Corporan, 2004].

The baseline JP-8 fuel was supplied to the engine from an underground facility tank. The JP-8/synjet blends were supplied from an external tank pressurized with nitrogen to feed the engine pump. The engine was initially operated using JP-8 and then transitioned to operation with the fuel blends. After transition, for a given engine operating condition, the fuel flow rate was controlled to obtain a constant T_5 (turbine exit temperature). This approach ensured the best run-to-run repeatability with respect to engine power output and combustor temperature for the conditions considered. For these tests, the engine was operated at idle and cruise power conditions.

Emissions Instrumentation. Particulate emissions from the T63 engine were captured and transported to the analytical instruments via an oil-cooled probe. The probe was installed facing the flow in the center and near the exit of the engine to help capture a "representative" sample of the engine exhaust and avoid diluting or contaminating with surrounding air. In order to minimize particle loss by diffusion and impaction, the probe and sample lines were built with stainless steel tubing, and sharp bends were avoided. The engine exhaust sample was immediately diluted at the probe tip and the sample line was maintained at 75°C to minimize water condensation and particulate loss to the wall due to high wall-to-sample temperature gradients. Sample dilution also prevented saturation of the analytical equipment. The diluted sample was drawn into the instruments via a vacuum pump, and the dilution air and sample flows were controlled with high precision flow controllers. All analytical measurements were corrected for dilution flow to obtain actual values.

On-line analysis of the mostly non-volatile particulate emissions sampled at the engine exit was performed using a TSI Model 3022A Condensation Nuclei Counter (CNC) to provide a count of the total particles per unit volume (particle number density) and a TSI Model 3936 Scanning Mobility Particle Sizer (SMPS) to obtain a particle size distribution. For the latter, a nano Differential Mobility Analyzer (DMA) TSI Model 3085 with a Model 3025 CNC were used in the SMPS to classify and quantify the particles 4-160 nm in diameter. In addition to the particle measurements, mass concentration emissions were measured using a Rupprecht & Pataschnick Tapered Element Oscillating Microbalance (TEOM) Model 1105.

Gaseous emissions were extracted using an undiluted, oil-cooled probe and quantified using a Horiba FIA-510 total hydrocarbon analyzer (THC), an M&C PMA-10 oxygen analyzer,

and an MKS MultiGas 2030 Fourier-Transform Infrared (FTIR) based gas analyzer. Most gases were quantified using the FTIR analyzer, which is capable of quantifying all non-symmetric gaseous species at parts-per-billion (ppb) to percent sensitivity and can simultaneously analyze and quantify more than thirty gases.

An in-house designed smoke machine was used to quantify the engine smoke numbers, which were measured following the SAE Aerospace Recommended Practice (ARP) 1179. For the measurement, the engine exhaust is sampled at a preset flow rate (typically 0.25-0.50 ft^3/min) and passed through a paper filter. The smoke number is calculated via the difference in reflectance of the filters measured using a Photovolt Instruments Model 577 reflectometer before and after collection of the soot sample. Only a limited number of smoke number measurements were made in this study.

Fuels. JP-8 is petroleum-based commercial Jet A-1 fuel with a military additive package that includes an icing inhibitor, corrosion inhibitor/lubricity enhancer and an anti-static additive. The synthetic jet fuel was obtained from Syntroleum Corporation, a natural gas recovery company located in Tulsa, Oklahoma. Syntroleum Corporation uses a proprietary process to convert natural gas into synthetic oil which can then be subsequently upgraded into various fuels and other hydrocarbon-based products (see www. syntroleum.com). The first-step of the process is the production of synthesis gas (syngas--carbon monoxide and hydrogen) by reacting the natural gas with air in a proprietary auto-thermal reformer reactor. The second step converts the synthesis gas into synthetic crude via the Fischer-Tropsch process, in which the gas flows into a reactor containing a proprietary catalyst, converting it into synthetic oil. This synthetic crude is then processed to obtain jet or diesel fuels. The paraffinic feedstock used in this study provided physical properties consistent with those required to meet the specification of a JP-8.

The JP-8 and synjet fuels were analyzed using GC/MS to provide quantitative information about their chemical composition. Their respective chromatograms are shown in **Figures 1** and **2.** JP-8 is composed of numerous hydrocarbons with normal paraffins being the primary species. The n-paraffins range from n-octane (n-C_8) to n-hexadecane (n-C_{16}), with maximum concentration from n-decane (n-C_{10}) to n-dodecane (n-C_{12}). JP-8 also contains lower concentrations of cyclic paraffins, olefins and aromatics. As shown in Figure 2, similar to JP-8, the synjet fuel is also composed largely of alkane compounds, but it is primarily comprised of branched paraffins.
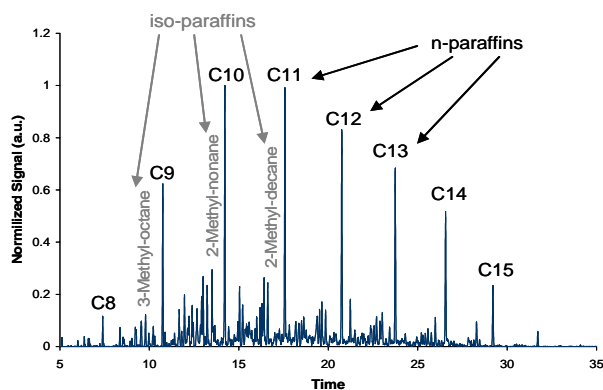

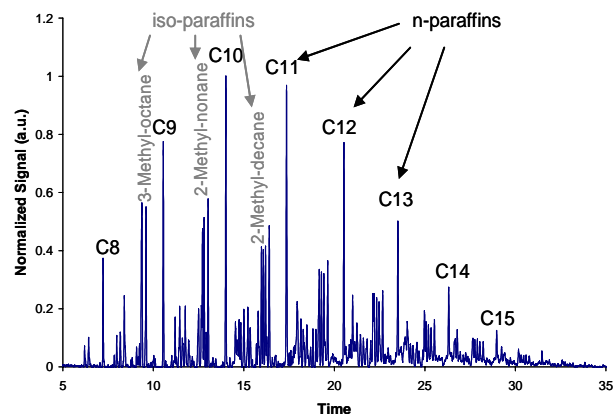**Figure 1**. Gas chromatogram of JP-8 fuel

Figure 2. Gas chromatogram of synthetic jet fuel

Results of the specification tests of the neat fuels using standard ASTM methods are shown in Table 1. As shown, the synjet properties conform to those for JP-8, except for the API Gravity (density of fuel slightly low) and the properties due to the additive package. Of note are the aromatic content and the freeze point of the fuels. Jet fuels contain aromatics mainly due to their higher energy density relative to the aliphatic compounds and to swell elastomers and prevent leaks through seals in fuel system components. These latter issues should be addressed before acceptance of synjet fuels for use in aircraft fuel systems. The lower freeze point of the synjet is attributed to the high concentration of iso-paraffins relative to the normal paraffins.

Table 1. ASTM Fuel Specification Tests for JP-8 and Synthetic Jet Fuel

ASTM Tests	Standard	JP-8 (POSF 3773)	Synthetic Fuel (POSF 4734)
Total Acid Number, mg KOH/g (D3242)	Max 0.015	0.000	0.001
Aromatics, %vol (D1319)	Max 25.0	15.9	0.0
Distillation-Residue, % vol (D86)	Max 1.5	0.7	1.4
Distillation-EP, ° C (D86)	Max 300	256	271
Freezing Point, °C (D5972)	Max -47	-51	-59
Existent Gum, mg/100mL (D381)	Max 7.0	1.0	0.20
Viscosity @ -20°C, cSt (D445)	Max 8.0	4.4	4.6
Particulate Matter, mg/L (D5452)	Max 1.0	0.2	0.10
Water Reaction (D1094)	Max 1B	1	1
FSII (DiEGME), % vol (D5006)	0.10-0.15	0.07*	0.00*
Conductivity, pS/m (D2624)	150-600	176	0*
API Gravity @ 60°C (D4052)	37-51	45.4	55.3*
Flash Point °C (D93)	38	60	49

Results and Discussion

Neat JP-8, synthetic jet fuel and seven JP-8/synjet fuel blends in increments of 12.5% by volume were evaluated on the T63 to assess the impacts of the synjet fuel on emissions and overall engine performance. Test data show no adverse impacts on engine performance or penalties on total engine fuel flow using the synjet fuel. That is, the fuel flow required to obtain a constant turbine exit temperature (T_5) using the synjet or JP-8/synjet blends was approximately the same as with the baseline JP-8. In addition, the engine was observed to operate smoothly during the transition from neat JP-8 fuel to the JP-8/synjet blend.

Particulate Emissions. Reductions in T63 particle number density emissions using several blend ratios of synjet in JP-8 are shown in **Figure 3**. As expected, particle number density (#/cm^3) decreased significantly with increased concentrations of synjet fuel, which was attributed largely to the reduced aromatic concentration in the resultant fuel or blend. Reduction of the aromatics decreases the concentration of "seed" molecules that contribute to the formation of soot nuclei, therefore decreasing the production of fine soot particulate relative to use of a higher aromatic JP-8 fuel. Dilution of the aromatic content with a "low-sooting", higher hydrogen-to-carbon ratio, iso-paraffinic fuel was also a factor in promoting the reduction of particulate emissions. This behavior had been seen previously on the T63 engine with blends of paraffinic solvents in jet fuel (Corporan, 2004).
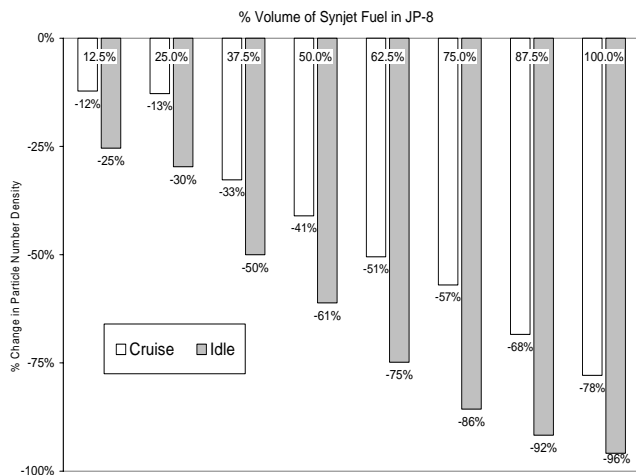
Figure 3. Reductions in particle number density emissions from T63 engine as a function of synthetic fuel in JP-8

Blending with synjet also significantly reduced the mean diameter of the particulate exhaust. **Figure 4** displays a strong linear relationship between the mean particle diameter and the concentration of synjet in the fuel blend for both idle and cruise conditions. These results suggest that particle coagulation from these hydrocarbon fuels is a physical process with little dependence on combustor conditions. The resultant smaller diameter particles are primarily the result of reduced number of particles available for coagulation and surface growth. Shifts in the particle size distribution curves to smaller diameter particles and lower concentrations for both engine conditions were observed with increased concentration of synjet fuel. Since the particulate mass is related to the diameter and number of particles, a reduction in these parameters should result in a reduction in the total PM mass.
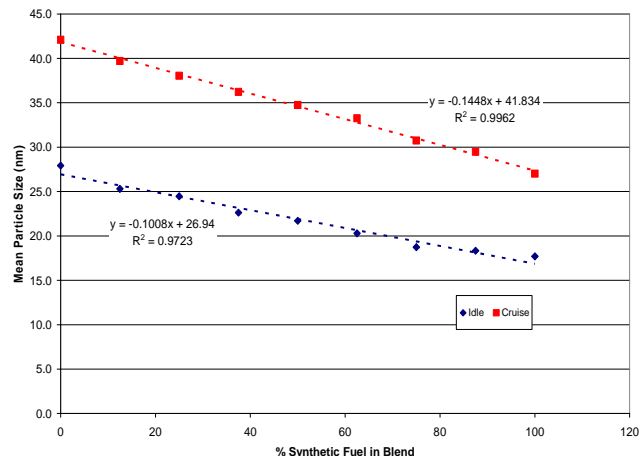
Figure 4. Effects of synthetic fuel on particle mean diameter emissions from T63 engine

Accordingly, direct mass measurements with the TEOM showed reductions of up to 95% with neat synjet fuel relative to operation with JP-8 (see **Figure 5**.). Unfortunately, data for the neat synjet at idle and the 87.5% synjet in JP-8 were not obtained due to incorrect setting of the dilution flow, which resulted in low signal-to-noise data from the TEOM. Reductions of approximately 50% were observed for both engine conditions for the 50% synjet blend, which supports the near linear correlation between the aromatic concentration and particulate mass.
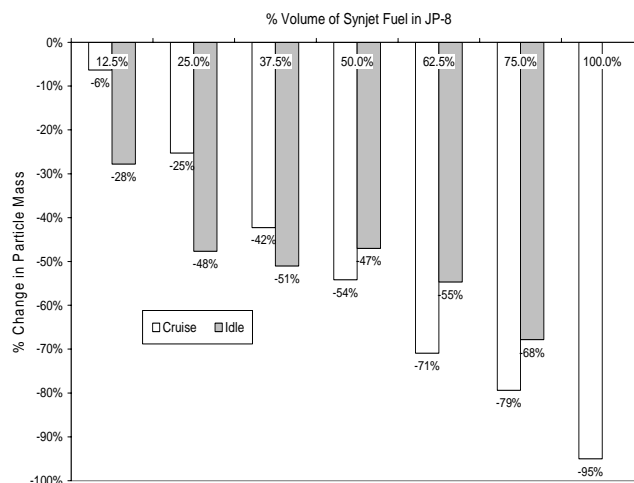
Figure 5. Reductions in particulate mass emissions from T63 engine as a function of synthetic fuel in JP-8

Smoke Number. Smoke numbers for the test conditions studied are shown in Table 2. Consistent with the particle mass and number data, significant reductions in smoke numbers were observed for the synjet fuel and blends relative to operation with JP-8.

Table 2. Smoke Numbers for T63 Engine Operating with Blends of Synthetic Jet Fuel and JP-8

Engine condition	Concentration of Synthetic Fuel in JP-8					
	0	12.5%	25%	37.5%	75%	100%
Idle	6.42	3.97	3.78	2.65	0.17	0.04
Cruise	29.7	26.62	23.73	19.7	8.68	3.81

Gaseous Emissions. The synthetic fuel had negligible effect on the primary gaseous emissions; specifically, the CO, CO_2, NO_x and unburned hydrocarbons. This was expected since the engine fuel flow rates and combustion temperatures were unaffected with the addition of the synjet. Only SO_x emissions were reduced as the result of the sulfur-free nature of the synjet fuel.

Conclusions

Reductions in turbine engine particulate emissions using a natural gas derived synthetic jet fuel (synjet) were demonstrated in a T63 engine. Greater than 90% reduction in particulate mass and number density and over 80% reduction in smoke number were observed with neat synjet fuel relative to operation on JP-8. Negligible effect on gaseous emissions (except for reductions in sulfur oxides) and no measurable fuel flow penalties or detrimental effects on engine performance were observed with neat synthetic fuel or the blends. Although significant emissions benefits were produced with the synthetic fuel (neat and blended), studies on material compatibility and additional emission studies on more relevant platforms should be conducted. In addition, economic and logistic considerations should be evaluated to further assess the potential of using synthetic fuels in military aircraft either neat or as a JP-8 fuel extender.

References
1. National Research Council, "Research Priorities for Airborne Particulate Matter, 1. Immediate Priorities and a Long-Range Research Portfolio," National Academy Press (1998).
2. Ritcher H., Howard J.B., "Formation of Polycyclic Aromatic Hydrocarbons and Their Growth to Soot-A Review of Chemical Reaction Pathways," Prog. Energy and Comb. Sci. 26 (2000) 565-608.
3. Corporan, E., DeWitt, M., Reich R, Monroig O., Larson, V., Aulich, T., Mann, M. and Seames, W., "Impacts of Biodiesel on Pollutant Emissions of a JP-8 Fueled Turbine Engine," AWMA Paper 751, Air Waste and Management Association National Meeting (2004).
4. Edwards, J.T., Minus, D., Harrison, W., Corporan, E., DeWitt, M., Zabarnick and S., Balster, L., "Fischer-Tropsch Jet Fuels-Characterization for Advanced Aerospace Applications," AIAA Paper 2004-3885.
5. Corporan, E., DeWitt, M.J. and Wagner, M., "Evaluation of Soot Particulate Mitigation Additives in a T63 Engine" Fuel Proc. Tech. 85 (2004) 727-742.
6. Corporan, E., DeWitt, M.J., Monroig, O. and Wagner, M; "Influence of Fuel Chemical Composition on Particulate Matter Emissions of a Turbine Engine," Proceedings of ASME Turbo Expo Paper No. GT2004-54335, (2004).

NANOSTRUCTURED SORBENTS FOR HEAVY METALS EMISSIONS CONTROL-A REVIEW

Pratim Biswas, Achariya Suriyawong, Marina Smallwood, James D. Noel, Myonghwa Lee, and Daniel E. Giammar

Washington University in St. Louis
Environmental Engineering Science Program
One Brookings Drive, Campus Box 1180
St. Louis, MO 63130

Introduction

Metallic species are encountered in many high temperature processes – both as a natural, trace constituent in fuels and as an industrially processed commodity. Sources include coal combustors, waste incinerators, oil combustors, jet engines, smelters, steel production processes, welding, deactivation furnaces for demilitarization operations, and many others. When introduced into a combustion system, the volatile heavy metals vaporize at high temperatures, and nucleate and grow in the cooler downstream regions. This results in the formation of a submicrometer aerosol. Conventional particle control devices are not effective in capturing particles in these size ranges[1,2]; resulting in an enrichment of these heavy metals in the exhaust gases. Several studies have reported that combustion sources are a major contributor of heavy metals in the atmosphere[3,4]. In addition, fine particles pose an enhanced health risk, and many of these metals are toxic constituents in these size ranges[5-8]. Thus, there is a need to develop control methodologies for the capture of heavy metals in combustion systems.

There are several methods that have been proposed for control of toxic metal emissions from combustors[1,9]. Bulk sorbents have been have been shown to be effective for capture heavy metal species in combustion systems, however, they are plagued with several physico-chemical limitations[10,11]. Once the metallic species has chemisorbed to the outer surface, the inner volume is rendered ineffective. Thus a large volume of bulk sorbent is required to capture trace metals. Furthermore, they have been ineffective in certain environments, for example when chlorine is present[12]. In addition bulk sorbents have not been found to effectively suppress the nucleation of the heavy metal species. An alternate approach is the use of novel nanostructured sorbent agglomerate processes for the capture of heavy metals in combustion environments[13,14]. Several studies have investigated the effectiveness of this process for the capture of heavy metals such as lead [15]. The nanostructured sorbent consists of an agglomerate of nanometer sized primary particles. Thus the agglomerate has a very high surface area to allow for chemisorption of the heavy metal species. However, the agglomerate is large enough that it is readily captured.

In this paper, the use of nanostructured sorbents for controlling metal emissions from combustors is reviewed. First, the descriptions of the pathways of trace heavy metal species (lead, cadmium, mercury and others) and the sorbent-metals interactions, bulk and nanostructured sorbents, in combustion system are discussed. This is followed by a recent experimental data for the capture of gaseous mercury using nanostructured sorbents in laboratory-scale coal combustors. The conclusion of this review will discuss the use of aerosol dynamic models to optimize injection strategies to ensure that sorbents have a high specific surface area, retain their active sites for metal capture, and the size distribution that would result in the most effective capture in a particle control device.

Mechanistic pathways of trace heavy metal species and the sorbent-metals interactions in combustion environment

Several researchers have conducted studies on metallic species aerosol formation and growth dynamics in high temperature aerosol flow reactors. Key aspects studied include; transfer of the toxic metal species from the matrix (such as the fuel or waste) to the gas phase, their transformation in the gas phase, ultimate formation, and growth dynamics in a varying temperature field[9]. The resultant size distribution of the aerosol in combustion systems establishes the capture characteristics in pollution control devices, atmospheric transformation rates, transport and deposition characteristics, visibility effects, and health effects.

Figure 1 illustrates the mechanistic pathway of toxic metal species in combustion system resulting in particle formation with and without the addition of sorbents.. As the temperature cools at the exit of the combustor, the species nucleate to form stable clusters. The nucleation rate also depends on the speciation of the metallic species. The oxides typically have low vapor pressures, and tend to nucleate rapidly when the temperature decreases. Certain heavy metals, such as mercury, remain in the elemental state[14]. Some heavy metals like mercury also have high vapor pressures and therefore tend to nucleate slowly. The nucleated clusters can then grow by collisions and by condensation of molecular species. The primary particles in an agglomerate may restructure due to sintering thus altering the morphology and the size. Studies have shown that the metallic species that result in a submicrometer aerosol are difficult to capture using conventional particle control devices[1,2,16].
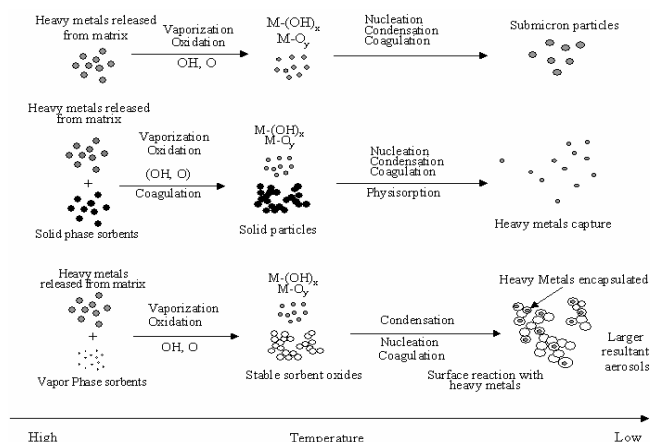

Figure 1. Mechanistic pathway of toxic metal species in combustion system resulting in particle formation.

The use of nanostructured sorbents has demonstrated suppression of the homogenous nucleation pathway; and chemisorption of the vaporous metallic species with the sorbent, by a large available specific surface area of the sorbent material [13]. The growth dynamics of the sorbent particles are critical in establishing the surface area and the overall mobility diameter. These factors will change as a result of the time-temperature history that the sorbent encounters in the combustion system. Sintering of the sorbent will tend to reduce the available surface area and convert the material to more of a bulk material; whereas too short a residence time will result in an agglomerate size that is not effectively trapped in the particle control device. To firmly understand and predict the sorbent particle structure, an aerosol dynamics model that accounts for particle growth has been developed. The model accounts for collisional growth, and accounts for the change in surface area due to both collisions and

sintering. Use of such models allows optimize injection strategies for most effective capture of heavy metal species. Preliminary data for titanium dioxide sorbents for the capture of mercury in coal combustion exhausts is provided.

Mercury capture using nanostructured sorbents

Figure 2 illustrates the mechanistic pathways of the transformation of mercury species in a coal combustor, and the interaction with the sorbent materials. In typical combustion exhausts, the mercury remains in the elemental state in the gas phase. The indicated oxidation pathways are relatively slow, thus mercury remains in the elemental state primarily. While aerosol surfaces such as that of fly ash may result in some transfer to the particle phase, this is a minimum. This is primarily due to the low reactivity of the fly ash species to the gas phase mercury. The presence of chlorine and other radicals in the combustion environment may promote chemical oxidation. In summary, there is a distribution of the mercury but most of it remains in the gas phase which precludes its capture in existing particle control devices. Understanding the pathways of mercury transformation in the combustion system allows the design of effective capture methodologies.   A designed injection strategy provides the availability of a high surface area agglomerate sorbent to scavenge the mercury vapors and promote their heterogenous oxidation, as illustrated in the bottom part of **Figure 2**. Clearly the high surface area agglomerate has to be engineered in a manner that there is an affinity for the gas phase mercury species. The goal is to associate the mercury species with the sorbent and its transfer to the particle phase so that it is readily captured in conventional control devices. Another objective is that the mercury be firmly bound to the sorbent surface so that it is not readily entrained once disposed to the environment.
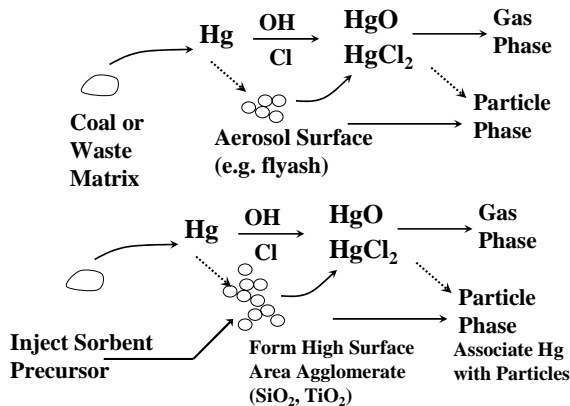

Figure 2. Pathways of Hg in a coal combustor. Section below indicates potential pathway in presence of a sorbent

Experimental. The experimental set up to study Hg capture using sorbents in a coal combustor is depicted in **Figure 3.** A detailed description of the flow reactor system, *in situ* generated TiO$_2$, and the experimental procedure is similar to the one developed by Wu *et. al*[14]. In this work, the sorbent was injected into a laboratory scale coal combustion system. Titanium (IV) isopropoxide (Ti[OCH(CH$_3$)$_2$]$_4$; 97% Aldrich) was used as precursor for TiO$_2$. Coal feed rate was maintained at 0.9 g/hr. The sorbent precursor was pre-heated to 80 ^{o}C; and the carrier gas (N$_2$) flow rate was 0.2 lpm. Furnace temperature was maintained at 1100 ^{o}C with excess air (1.75 lpm air feed rate) to ensure complete combustion. Dilution air was added at the exit stream to obtain 0.5

µm cutoff size using cascade impactor. A UV lamp and electrostatic precipitator were used as photochemical reactors. The real time differential mobility analyzer (DMA) and condensation particle counter (CPC) were used to obtain particle size distributions.
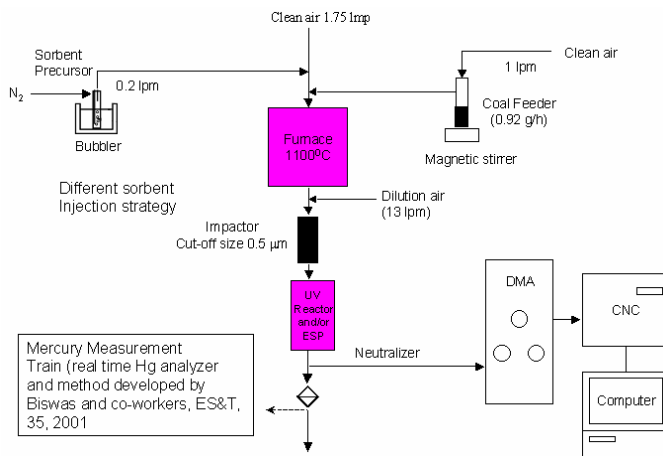

Figure 3. Schematic diagram of the experimental system for coal combustion studies

Sorbent injection strategies

The evolution of sorbent morphology, size and number concentration undergoing collisional growth and sintering were modeled. The influence of fractal structure on the collision kernel can be accounted for from the free molecular regime to the continuum regime. The model equations based on the work by Kruis *et al*.[18] and Jeong and Choi[19] were modified to predict the evolution of the sorbent size distribution and the morphology of the agglomerates. Using a model that accounts for the morphology of the aggregates in a dynamical manner allows for more accurate prediction of the surface area and the collisional rates of growth, in contrast to more traditional models that assume spherical particles. The variation of flue gas temperatures, similar to those found at full-scale facility, were taken into account since temperature is an essential parameter in both determining the collision rate as well as characteristic sintering time. Four sorbent injection locations were selected to simulate: at the combustor, after combustor, after heat exchanger and before the electrostatic precipitator (ESP). The temperatures at these locations are 1500, 1000, 275 and 150 ^{o}C, respectively.
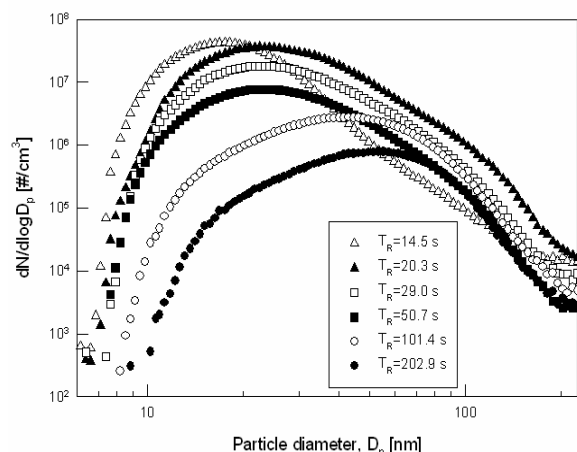
Figure 4. Size distributions of particles at the exit of the furnace at 1100 ^{o}C.

Results and discussion.

Fly Ash Size Distributions. Size distributions were measured for a variety of different conditions. For coal combustion alone, the size distributions of the submicrometer ash at 1100 ^{o}C are shown for different residence times in the furnace (**Figure 4**). Larger geometric mean diameters were observed for longer residence times, primarily due to collisional growth. Predictions of a lognormal model[20] were used to confirm the different trends. The size distribution of the fly ash with the sorbent precursor or solid phase sorbents injections were also determined and will be discussed.

Mercury Capture. Experiments were conducted over a range of conditions such as with UV light source, with ESP and without any light source to determine the dependence of mercury capture. Results of experiments wherein pre-synthesized sorbent was injected was compared to that in which the sorbent was formed from the precursor species in the combustor. In addition, the effects of injection locations on mercury removal efficiency will be presented. Results indicate that a co-feed of the sorbent precursor with the coal results in a high capture of the mercury species. Injecting the sorbent precursor also allowed best control of its characteristics (size and morphology), and this was studied by using some of the model predictions described in the next section.
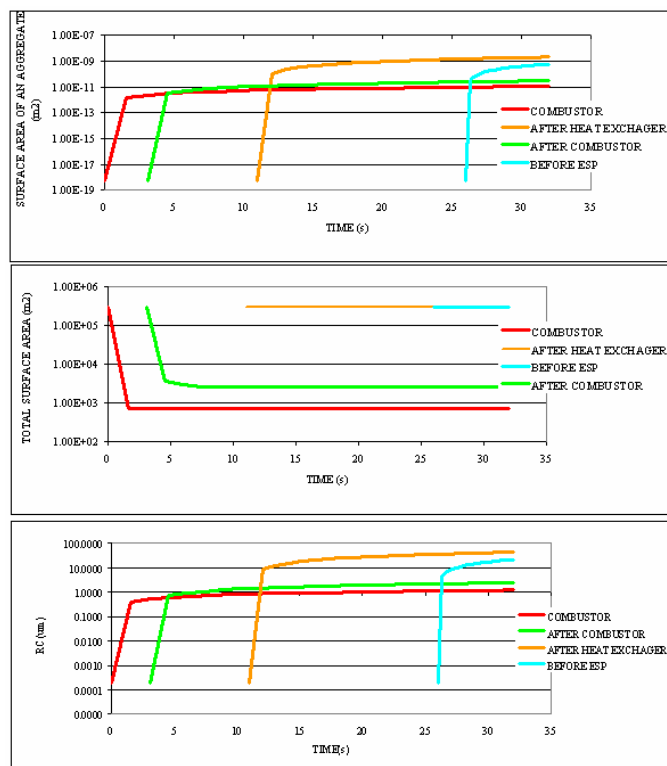

Figure 5. Predicted surface area of a TiO$_2$ aggregate, total surface area of TiO$_2$ in the system and a TiO$_2$ aggregate size with 1 mole of TiO$_2$ injected.

Sorbent Particle Characteristics. The simulation results of TiO$_2$ injection are shown in **Figure 5.** Sorbents injected after heat exchanger and before ESP provided highest total agglomerate surface area, while the surface area obtained from the injection at the combustor and after combustor were three-fold less. The sorbent agglomerate size was found largest (~10 µm) where the sorbents were injected into the flue gas after heat exchanger and smallest (~0.5 µm) when sorbents were injected into the combustor. This demonstrates that sintering process prevail under high temperature, while coagulation process dominate at lower temperatures. The simulated agglomerate sizes of the sorbents lie within the range that would result in its effective capture using a conventional particle control device. Sorbents should be injected into the system at the lower temperature zone, to minimize amount of sorbent used and to maximize the removal of heavy metals..

Conclusions

A brief review of nanostructured sorbent processes for heavy metals capture in combustion environments was discussed. The importance of the need to identify the pathways of the metal species and their transformations was elucidated. Results from laboratory scale systems for the study of mercury capture in coal combustion environments was discussed. Results of an aerosol dynamics model that accounted for both collisional growth and sintering of the sorbent particles were used to determine injection strategies that would promote high effectiveness in capture of the metal species, and their capture in existing particle control devices.

References

(1) Linak, W. P.; Wendt, J. O. L., Toxic Metal Emissions from Incineration - Mechanisms and Control. *Progress in Energy and Combustion Science* **1993,** 19, (2), 145-185.

(2) Zhuang, Y.; Kim, Y. J.; Lee, T. G.; Biswas, P., Experimental and theoretical studies of ultra-fine particle behavior in electrostatic precipitators. *Journal of Electrostatics* **2000,** 48, (3-4), 245-260.

(3) Nriagu, J. O., Legacy of Mercury Pollution. *Nature* **1993,** 363, (6430), 589-589.

(4) Ondov, J. M.; Wexler, A. S., Where do particulate toxins reside? An improved paradigm for the structure and dynamics of the urban mid-Atlantic aerosol. *Environmental Science & Technology* **1998,** 32, (17), 2547-2555.

(5) Oberdorster, G., Effects and fate of inhaled ultrafine particles. *Abstracts of Papers of the American Chemical Society* **2003,** 225, U955-U955.

(6) Lippmann, M.; Frampton, M.; Schwartz, J.; Dockery, D.; Schlesinger, R.; Koutrakis, P.; Froines, J.; Nel, A.; Finkelstein, J.; Godleski, J.; Kaufman, J.; Koenig, J.; Larson, T.; Luchtel, D.; Liu, L. J. S.; Oberdorster, G.; Peters, A.; Sarnat, J.; Sioutas, C.; Suh, H.; Sullivan, J.; Utell, M.; Wichmann, E.; Zelikoff, J., The US Environmental Protection Agency particulate matter health effects research centers program: A midcourse report of status, progress, and plans. *Environmental Health Perspectives* **2003,** 111, (8), 1074-1092.

(7) Miller, C.; Biswas, P.; Leikauf, G., Combustion generated nickel species aerosols: Role of chemical and physical properties on lung injury. *Aerosol Science and Technology* **2001,** 35, (4), 829-839.

(8) Zhou, Y. M.; Zhong, C. Y.; Kennedy, I. M.; Leppert, V. J.; Pinkerton, K. E., Oxidative stress and NF kappa B activation in the lungs of rats: a synergistic interaction between soot and iron particles. *Toxicology and Applied Pharmacology* **2003,** 190, (2), 157-169.

(9) Biswas, P.; Wu, C. Y., Control of toxic metal emissions from combustors using sorbents: A review. *Journal of the Air & Waste Management Association* **1998,** 48, (2), 113-127.

(10) Uberoi, M.; Punjak, W. A.; Shadman, F., The Kinetics and Mechanism of Alkali Removal from Flue-Gases by Solid Sorbents. *Progress in Energy and Combustion Science* **1990,** 16, (4), 205-211.

(11) Uberoi, M.; Shadman, F., Sorbents for Removal of Lead Compounds from Hot Flue-Gases. *Aiche Journal* **1990,** 36, (2), 307-309.

(12) Scotto, M. V.; Uberoi, M.; Peterson, T. W.; Shadman, F.; Wendt, J. O. L., Metal Capture by Sorbents in Combustion Processes. *Fuel Processing Technology* **1994,** 39, (1-3), 357-372.

(13) Owens, T. M.; Biswas, P., Vapor phase sorbent precursors for toxic metal emissions control from combustors. *Industrial & Engineering Chemistry Research* **1996,** 35, (3), 792-798.

(14) Wu, C. Y.; Lee, T. G.; Tyree, G.; Arar, E.; Biswas, P., Capture of mercury in combustion systems by in situ-generated titania particles with UV irradiation. *Environmental Engineering Science* **1998,** 15, (2), 137-148.

(15) Biswas, P.; Zachariah, M. R., In situ immobilization of lead species in combustion environments by injection of gas phase silica sorbent precursors. *Environmental Science & Technology* **1997,** 31, (9), 2455-2463.

(16) Helble, J. J., A model for the air emissions of trace metallic elements from coal combustors equipped with electrostatic precipitators. *Fuel Processing Technology* **2000,** 63, (2-3), 125-147.

(17) Zhuang, Y.; Biswas, P., Submicrometer particle formation and control in a bench-scale pulverized coal combustor. *Energy & Fuels* **2001,** 15, (3), 510-516.

(18) Kruis, F.E.; Kusters, K.A.; Pratsinis, S.E.; Scarlett, B., A simple model for the evolution of the characteristics of aggregate particles undergoing coagulation and sintering. *Aerosol Science and Technology* **1993**, 19, 514-526.

(19) Jeong , J..I.; Choi, M., A simple bimodal model for the evolution of non-spherical particles undergoing nucleation, coagulation and coalescence. *J. Aerosol Science* **2003**, 34, 965-976.

(20*)* Pratsinis,S.E. Simultaneous nucleation, condensation, and coagulation in aerosol reactors*. **Journal of Colloid and Interface Science** **1988,*** 124, 416-.

NEW SORBENTS FOR MERCURY REMOVAL FROM FLUE GASES

Gokhan O. Alptekin, Margarita Dubovik, and Michael Cesario

TDA Research, Inc.
12345 W. 52nd Avenue
Wheat Ridge, CO 80033

Introduction

Coal-fired power plants currently emit about 41 tons of mercury per year, about 40% of the total U.S. man-made mercury emissions. The U.S. Environmental Protection Agency (EPA) determined the need to reduce mercury emissions from power plants by implementing maximum achievable control technology. Although, substantial reductions will likely be required over the next decade, there are still uncertainties, particularly related to the cost and effectiveness of existing mercury control technologies. An ideal mercury abatement system would be easy to retrofit into the existing coal-fired electric utilities. An attractive approach is dry sorbent injection where the sorbent injected into the flue gas reacts with gas phase mercury and the mercury-laden sorbent is removed with the fly ash either by a fabric filter or by an electrostatic precipitator (ESP). The requirements for such a sorbent are straightforward: 1) it should be low cost, 2) it should remove mercury with high capacity, and 3) it should not present any environmental problems in its own right. Another less obvious but very important consideration is that the sorbent collected with the fly ash, must not degrade and limit the normal potential uses of fly ash.

Several physical adsorbents, particularly activated carbons, can remove mercury from flue gases produced by coal combustion[1,2]. However, activated carbons are non-selective adsorbents; most of the flue gas components adsorb on carbon, competing with mercury, thus, the efficacy of carbon-based sorbents is severely compromised. To improve the adsorption capacity, it is common to chemically modify the activated carbons with various chemical promoters including sulfur, iodine, chlorine and nitric acid, although the carbon treatment processes significantly increase the cost of the sorbent (chemically modified activated carbons costs about 4 times of the unmodified carbon)[3]. As a result, both for promoted and unpromoted carbons, the projected annual cost of abatement is high in the order of $38,000 per pound of mercury removed (based on the combined operating and annualized capital costs) or over $4 million per year for a 250 MW power plant[4]. In fact, all these estimates understate the difficulties and costs associated with using carbon-based sorbents. Much of the fly ash collected in the particulate control module is sold as an extender to Portland cement: fly ash can replace as much as 80% of the cement in some grades. However, fly ash that contains carbon is not suitable for use in cement. The problem is much more serious than lost sales. If the fly ash is not salable for concrete, it has no use at all, and immediately becomes an expensive waste problem.

TDA Research, Inc. is developing a new sorbent/catalyst combination to carry out oxidation of mercury and subsequent capture and removal of all mercury species. The sorbent is made of non-carbon based materials and has a high mercury absorption capacity, thus will not alter the properties of the fly ash. The sorbent can be produced as an injectable powder for easy integration into the existing power plant infrastructure. This paper summarizes the initial testing results of the new sorbent material.

Experimental

Sorbent Synthesis. Synthesis method of the sorbent was described in detail in prior literature[5]. As part of this work, several formulations were screened according to their physical properties, including porosity, surface area, crush strength of the pellet and active material content. In the selection of proper active material and support, the material costs were taken into consideration. The choice of substrate materials included conventional supports, which are low-cost and have high surface area (150 to 580 m^2/g measured by the manufacturers). The best formulations with the desired physical properties were tested for their sulfur removal performance under simulated conditions.

Test Setup. For these experiments, a fixed-bed reactor was used to measure sorbent performance for removing mercury from flue gases. The sorbent reactor consists of a 2.5 cm-OD quartz-lined stainless steel reactor tube that contains a frit at its mid-point to support monoliths or pellets. A Mellen tube furnace surrounding the reactor was used to control the temperature. The desired gases were introduced into the system through electronic mass flow controllers. After mixing in a manifold, the gas stream is preheated above the dew point of water to prevent condensation. The mixture then passes through a saturator where water was mixed into the feed stream by a peristaltic pump. The preheated feed mixture was combined with a mercury laden-gas stream. Mercury was introduced using permeation tubes (VICI Metronics, Inc, CA), blending trace amounts of mercury into the synthetic flue gas. The preheated feed gas stream was then directed to the reactor. A valve system also allowed the feed gases bypass the reactor and flow directly to the analytical system for accurate measurement of the feed gas composition. The gas exiting the packed bed was conditioned before releasing into the environment.

Analytical System. To analyze for mercury, a Genesys Laboratory Systems Process Sentinel mercury vapor detector was used with a detection limit of nominally 1.0 μg /m^3 and a range of 1-999 μg/m^3 of mercury. After the tests, selected sorbent samples were sent to analysis in a local laboratory for chemical analysis using Inductively Coupled Plasma Atomic Absorption to confirm to mercury uptake of the sorbents.

Results and Discussion

In the proposed dry sorbent injection system, the sorbent/catalyst combination will be injected into the flue gas stream after the air preheater. At the injection location the flue gas temperature may range from 120 to 180°C, depending on the efficiency of the economizer and air pre-heater (a recuperative heat exchanger that heats the air to the boiler). Higher temperatures promote faster kinetics for mercury oxidation reaction. The removal process of mercury, however, favors lower temperatures, where lower equilibrium Hg concentration can be achieved (i.e., high removal efficiency). The preliminary bench-scale experiments were carried out to measure mercury absorption capacity of the sorbent at temperatures, very closely simulating the temperatures of the cold-side and warm-side of typical particulate control unit. In a typical test, we used a 2% O$_2$, 6% CO$_2$, 8% H$_2$O and 84% N$_2$ on volume basis to simulate the flue gas.

The sorbent achieved mercury absorption capacities ranging from 7.5 to 11.0 mg/g depending on temperature and space velocity. **Figure 1** shows the mercury breakthrough profile over the sorbent at 140°C under the flow of a sulfur-free simulated flue gas. The gas hourly space velocity and mercury inlet concentration through the test were maintained at 60,000 h^{-1} and 0.12 mg/m^3, respectively. The mercury absorption capacity of the sorbent was calculated as 10.85 mg/g at a pre-breakthrough level. Test result also suggests that the sorbent is capable of achieving over 95% mercury removal efficiency. The capacity of the sorbent is among the highest reported in the literature[6].
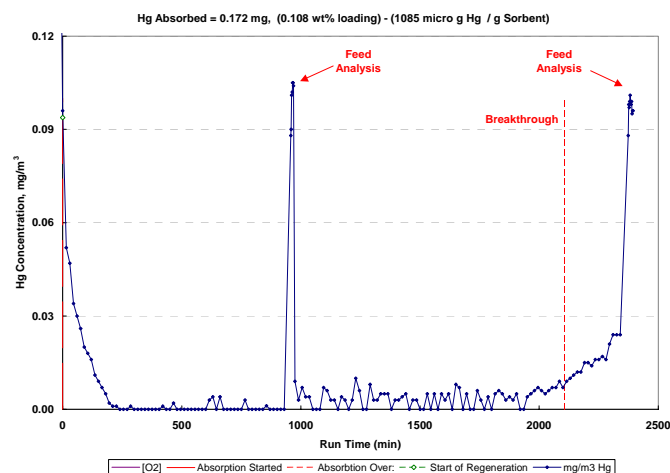
Figure 1. Mercury breakthrough profile over TDA sorbent with simulated flue gas containing 2% O_2, 6% CO_2, 8% H_2O and 84% N_2 on volume basis. Hg Inlet Conc.= 0.12 $\mu g/m^3$, T= 140°C, GHSV=60,000 h^{-1}.

Although effective flue gas desulfurization technologies are available that can reduce the sulfur emissions to very low levels, some amount of sulfur is likely to be present in the flue gas. Bench-scale experiments with sulfur containing simulated flue gas were carried out to demonstrate the mercury removal potential of the sorbent in the presence of sulfur. For these experiments, flue gas streams containing 3 and 300 ppmv sulfur dioxide (SO_2) was passed through the sorbent bed maintained at 140°C. These sulfur concentrations represents a flue gas stream with upstream Flue Gas Desulfurization and a flue gas generated with low sulfur coal combustion with no upstream desulfurization.
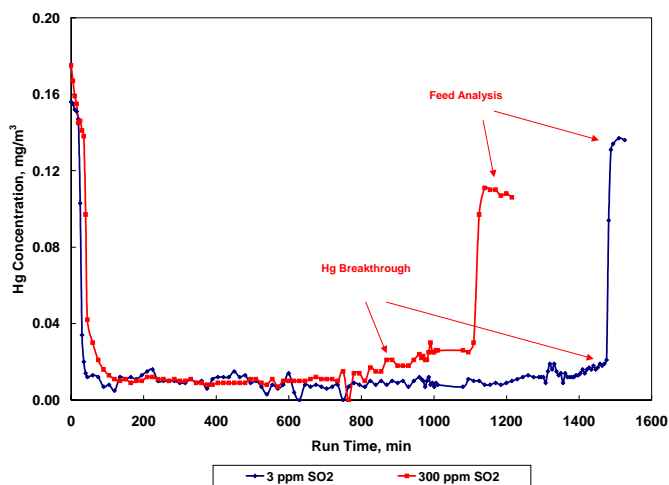

Figure 2. Mercury breakthrough profile over TDA sorbent with simulated flue gas containing 2% O_2, 6% CO_2, 8% H_2O and 84% N_2 on volume basis. Hg Inlet Conc.= 0.18 $\mu g/m^3$, T= 140°C, GHSV=650,000 h^{-1}.

The sulfur tests were carried out at 650,000 h^{-1} gas hourly space velocity, simulating the very short gas-solid contact times in dry sorbent injection systems. Table 1 shows the mercury absorption capacity of the sorbent at different SO_2 inlet concentrations. The mercury capacity of the sorbent is reduced as the sulfur level of the flue gas increased.

Table 1. Effect of SO_2 concentration on the mercury absorption capacity of the sorbent.

SO2 Concentration (ppmv)	Hg Absorption Capacity (microgram/g)
3	966
300	648

The preliminary bench-scale tests suggest that TDA's sorbent shows promise to effectively control mercury emissions even in high sulfur flue gas streams.

Acknowledgment

References
1. Carey, T.R., Hargrove J., Richardson, R., Meserole, F., **1997**, *Proceedings of the Air Waste Management Meeting*, Paper No. 97-WA72A05, 90th AWMA, Toronto, Canada.
2. Miller, S.J., Laudal, D.L., Chang, R., Bergman, P.D., **1994**, *Proceedings of the Air Waste Management Meeting*, Cincinnati, OH.
3. Sjostrom, S., Smith, T., Hunt, R., Chang, R., Brown T., **1998**, *Proceedings of the Air Waste Management Meeting*, San Diego, CA.
4. U.S. EPA, **1997**, *Mercury Study Report to Congress*, EPA-452/R-97.
5. Alptekin, G.O., Hitch, B., Dubovik, M., and Cesario, M., **2004**, Proceedings of 19th Western Coal Symposium, Billings, MO.
6. Granite, E., Pennline, H., Hragis, R., **2000**, *Ind. Eng. Chem. Res.,* 39, 1020.

SULFUR IMPREGNATION ON ACTIVATED CARBON FIBERS BY H₂S OXIDATION FOR MERCURY CONTROL

Wenguo Feng[1], Seokjoon Kwon[2], Eric Borguet[3], and Radisav Vidic[1]*

[1] Department of Civil and Environmental Engineering, University of Pittsburgh, Pittsburgh, PA 15261
[2] Connecticut Agricultural Experimental Station, New Haven, CT 06504
[3] Department of Chemistry, Temple University, Philadelphia, PA 19122

Introduction

Previous studies suggested that sulfur impregnated activated carbons offer much larger capacity for permanent sequestration of mercury from coal fired power plants as compared to virgin sorbents [1]. In addition, sulfur impregnation is feasible through oxidation of H₂S from waste streams [2].

Coskun and Tollefson [3] showed that sulfur loading increased with the increase in reaction temperature from 24 °C to 152 °C. Stejins et al. [4] reported that the only products formed below 200 °C are water and elemental sulfur. However, for temperatures above 300 °C, formation of SO₂ becomes significant. The carbon activity was maximized between 150 °C and 200 °C [5]. Bandosz suggested that products of H₂S oxidation were mainly elemental sulfur and sulfuric acid [6]. It was believed that a more acidic environment promotes the formation of sulfur oxides and sulfuric acid while a basic environment favors the formation of elemental sulfur (sulfur radicals). Mikhalovsky [7] suggested that carbon surface functional groups and transition metals affected the catalytic activity and selectivity to different products. It was believed that surface functional groups contribute significantly to the formation of SO_x during H₂S oxidation.

The objective of this study is to investigate the fundamentals of the sulfur impregnation process (pathways and products) through H₂S oxidation and associated impact on mercury uptake by these sulfur-impregnated sorbents.

Experimental

Sulfur impregnation onto Activated Carbon Fibers (ACFs) by H₂S oxidation was conducted using a fixed bed reactor system. The gases were supplied from pressurized tanks. H₂S and O₂ (O₂: H₂S = 4:1) were diluted by N₂ to a desired concentration by controlling the flow rate of each gas. The total gas flow rate to a quartz reactor (38cm long with 1cm OD) was maintained at 150 ml/min. The reactor was positioned vertically in the middle of a tubular furnace. The effluent gases were analyzed continuously by a Quadrupole Mass Spectrometer (QMS) 300. Two sets of experiments were conducted with ACF10 and ACF25. ACF10 was allowed to adsorb H₂S at 80°C and 150°C until the effluent H₂S concentration reached the influent level. These samples were labeled as ACF10-80C and ACF10-150C. ACF25 was impregnated with sulfur at 150ºC for 2, 6 and 24 hours. These samples were labeled as ACF25-150C-2hrs, ACF25-150C-6hrs, ACF25-150C-24hrs. The average amounts of sulfur deposited on the sorbent were determined from the breakthrough curve.

Samples before and after sulfur impregnation were characterized with respect to: surface area and pore size distribution based on nitrogen adsorption at 77K (Autosorb 1-MP, Quantachrome, Boynton Beach, FL); surface composition based on SEM-EDAX (Philips XL30 SEM equipped with an EDAX detector) and XPS analysis (Physical Electronics Model 550 equipped with a cylindrical, double-pass energy analyzer).

Results and Discussion

Table 1 summarizes average sulfur contents of the sorbents produced based on the QMS analysis of the H₂S breakthrough curve. Low temperature (e.g., 80 ºC) does not facilitate significant sulfur deposition through H₂S oxidation, even after a complete H₂S breakthrough was attained. Both ACF-10 and ACF-25 achieved much higher sulfur content at 150 ºC. This may indicate that H₂S oxidation can only take place inside smaller pores. This hypothesis is supported by pore size distribution measurements shown in Figure 1, which depicts changes in the pore size distribution of ACF10 after sulfur impregnation at 80 °C and 150 °C. It is clear that sulfur deposition at 80 °C was accomplished by pore filling rather than by monolayer deposition as the loss of the small pores was obvious, while very few medium micropores were occupied by sulfur molecules. No obvious difference in sulfur contents was found for ACF-10 and ACF-25 after complete breakthrough at 150 °C. This may be related to the similar small micropore volume of the two sorbents.

Table 1. Summary of Sulfur Impregnation Results

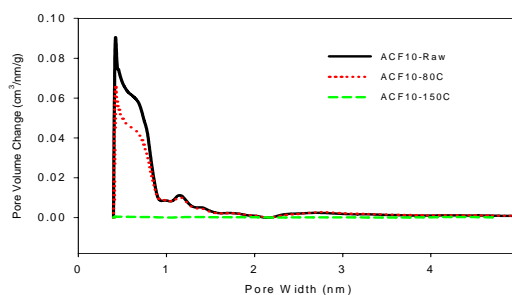| Sample Name	Average S% (QMS) (wt%)	Surface S% (EDAX) (wt%)	Pore Volume (cm³/g)	Surface Area (m²/g)
ACF10-Raw	0.2	0.2	0.371	920
ACF10-80C	6.7	1.14	0.299	710
ACF10-150C	26.3	34.5	0.0048	8.3
ACF25-Raw	0.2	0.2	0.741	1950
ACF25-150C-2hrs	4.1	1.02	0.714	1880
ACF25-150C-6hrs	10.2	7.36	0.634	1610
ACF25-150C-24hrs	30.5	34.41	0.015	100

Figure 1. Pore size distribution of ACF-10 before and after sulfur impregnation at different temperatures

Figure 2 shows changes in the pore size distribution of ACF25 as a result of sulfur impregnation at 150 °C for 2, 6 and 24 hours. It is clear that the initial loss in the pore volume after only 2 hours of impregnation occurred in small and medium micropores, while large pores were not affected by sulfur deposition. As the impregnation time was extended to 6 hours, further reduction in small and medium pores was observed. Reduction in the large pore volume was observed only after the amount of sulfur deposited on the ACF surface exceeded 20 wt% after 24 hours of impregnation. Similar conclusion can be made for the data shown in Figure 1 and Table 1, where the sulfur content exceeded 20 wt% before filling of large micropores was accomplished.
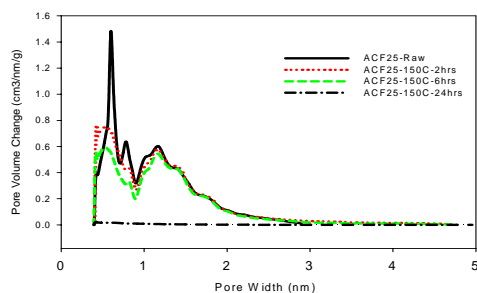
Figure 2. Pore size distribution of ACF-25 before and after S impregnation at different reaction times

SEM-EDAX analysis was conducted for ACFs before and after sulfur impregnation. EDAX provided the elemental compositions of the outer layer of the ACF samples, which were listed in the third column of Table 1. The average sulfur content impregnated at outer surface of the ACF at 80 ºC is much lower than that in the bulk. This means that the sulfur tends to deposit more inside than outside of the sorbent particle at lower temperatures. The increase in temperature resulted in sulfur deposition at the outer surface, as can be seen from Table 1. ACF-25 after shorter impregnation times (2 hours and 6 hours) also exhibited lower surface coverage as compared with the average sulfur content. For longer impregnation times (24 hours), surface sulfur content was higher than the average. This behavior suggests that sulfur impregnation occurs from the inside to the outside of the adsorbent particle.

Figure 3 shows the derivative weight loss of ACF-10 after sulfur impregnation at different temperatures. Sulfur was released in two temperature ranges (200-300 ^{o}C and 350-550 ^{o}C), which indicates the presence of two types of binding sites on the carbon surface. It is also clear that impregnation at higher temperature (150 ºC) leads to the formation of more thermally stable forms of sulfur species as evidenced by the shift of the second peak to higher temperature.
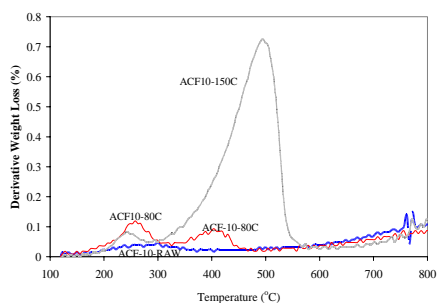

Figure 3. TGA analysis (Derivative Weight Loss) of ACF-10 before and after sulfur impregnation

The sulfur forms on ACF-25 before and after sulfur impregnation were also investigated by XPS. Figure 4 shows a peak around 164 eV (elemental sulfur) for the sulfur spectrum, which indicates that sulfur on ACF surface is mainly present in the elemental form.

As can be seen from Table 1, longer oxidation times lead to greater sulfur content on the ACF surface. However, higher sulfur content does not necessarily translate into better mercury removal because of the loss of surface area and pore volume associated with deposited sulfur (Figure 2). Under the experimental conditions evaluated in this study, sulfur impregnated ACFs with sulfur content of around 5 wt.% and reasonable pore structure demonstrated highest mercury uptake capacity (Figure 5).
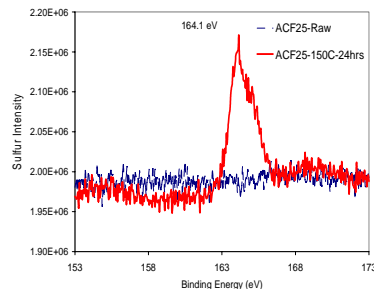

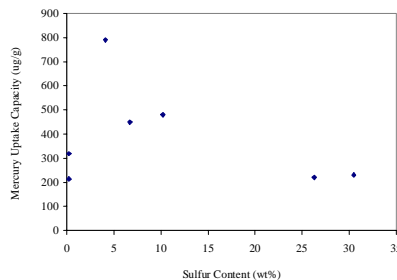**Figure 4**. XPS Spectrum of ACF25 before and after sulfur impregnation

Figure 5. Mercury uptake capacity as a function of sulfur content

Conclusions

Sulfur impregnated on the surface of ACF through H_2S oxidation was mainly in the form of elemental sulfur. The increase in impregnation time at 150 ºC leads filling of the pores by the deposited sulfur until there is complete loss of the original pore volume. Impregnation at lower temperature (80 ºC) and/or shorter impregnation time leads to partial pore filling as the dominant mechanism for sulfur deposition. The pathway for the impregnation process can be explained by a combination of pore filling and monolayer adsorption. Higher temperature resulted in more stable sulfur bonding with the carbon surface. Increase in the sulfur content does not lead to enhanced mercury uptake.

References
(1) Liu, W., Vidic, R.D., and Brown, T.D. *Environ. Sci. Technol.*, **2000**, 34(1), 154-159.
(2) Feng, W., Feng, X., Borguet, E. and Vidic, R.D. 35th Meeting of the American Chemical Society, Pittsburgh, PA, October 19-22, 2003.
(3) Coskun, I.A. and Tollefson, E.L., *The Canadian Journal of Chemical engineering,* **1980**. 58, pp72-76.
(4) Steijns, M., Derks, F., Verloop, A., Mars, P., *Journal of Catalysis,* **1976.** 2, 87-96.
(5) Ghosh, T.K., Tollefson, E.L. *The Canadian Journal of Chemical Engineering,* **1986**. 64, 969-976.
(6) Bandosz, T.J., *J. Colloid and Interface Science,* **2002**. 246(1), 1-20.
(7) Mikhalovsky, S.V. and Zaitsev, Y.P., *Carbon,* **1997**. 35(9), 1367-1374.

EVALUATION OF MERCURY CONTROL TECHNOLOGIES FOR SUBBITUMINOUS COAL-FIRED COMBUSTION SYSTEMS

Jill M. Mackenzie, Steven A. Benson, Donald P. McCollor, Michael J. Holmes

Energy & Environmental Research Center
University of North Dakota
15 North 23rd Street
Grand Forks, ND 58203

Introduction

Mercury speciation (elemental, oxidized, or particulate) in coal-derived combustion flue gases impacts the ability and the approach to control mercury emissions. Mercury speciation is largely dependent upon coal composition but is also influenced by plant configuration and operating parameters. Controlling mercury in coal-fired power plants is very complex and there is not a "one-size-fits-all" mercury control technology that can be applied to all coals and all power plant configurations. For example, mercury in the oxidized form is more reactive and easier to capture in existing equipment than mercury in the elemental form. Elemental mercury will require additional technologies for mercury oxidation or enhanced sorbents for control. Mercury control technology research and development efforts are focused on mercury measurement, speciation, reactions with particulate and flue gas, development of high temperature oxidation chemicals, sorbent (powder activated carbon [PAC] and non-carbon materials) enhancements, and advanced control technologies with tests conducted at the pilot plant scale and in existing air pollution control equipment.

Measurement of elemental, oxidized, and particulate forms of mercury is a critical part of developing and assessing control technologies. The Ontario Hydro (ASTM D6784-02) is the standard method for mercury speciation in flue gas but does not provide "real time" data.

As noted previously, mercury speciation in flue gases is dependent upon coal composition. The most significant influence on mercury speciation is the chlorine content. Appalachian and interior bituminous (Illinois) coals have high chlorine above 200 ppm and will produce flue gas that contains high proportions of oxidized mercury. Lignite and subbituminous coals have very low chlorine contents (less than 30 ppm) and produce flue gases that have high proportions of the more difficult to capture elemental mercury.

Mercury control technologies for Electric Generating Units (EGU) emission control configurations being investigated include: plants equipped with electrostatic precipitators (ESP) and/or baghouses (fabric filters [FF]), plants with wet and dry scrubbers, and plants equipped with selective catalytic reduction for NOx control and scrubbers.

Mercury control technologies for ESPs involve the injection of sorbents upstream of the ESP. Short term testing of PAC has been conducted in pilot- and full-scale ESP systems. PAC injection showed capture efficiencies for eastern bituminous (Brayton Point with 2 ESPs) of up to 90% control with a high level of carbon injection of 20 lb/Mmacf. PAC injection upstream of an ESP at sub-bituminous fired Pleasant Prairie plant showed 60% control with 10 to 20 lb/Mmacf. The mercury present in the Brayton Point flue gas was dominated by particulate and oxidized mercury forms but still required high levels of carbon injection to attain the levels of mercury control. The elemental form of mercury is dominant in the Pleasant Prairie flue gas and is not very reactive. The challenge is to develop a technology to capture elemental mercury, effectively and economically. Recent efforts have focused on reducing the quantity of PAC by using sorbent enhancement additives (SEA). The use of SEA can reduce PAC requirements to less than 5 lb/Mmacf. Pilot-scale testing has recently been conducted using SEA and PAC injection for mercury control for utilities firing subbituminous coals. The results of testing conducted in the pilot plant with the ESP only configuration will be presented.

Experimental

The pilot-scale particulate test combustor (PTC) was used in this effort to combust the coal. The PTC is a 550,000-Btu/hr pulverized coal (pc)-fired unit designed to generate fly ash representative of that produced in a full-scale utility boiler. A schematic diagram of the PTC is shown in Figure 1. The combustor is oriented vertically to minimize wall deposits. A refractory lining helps to ensure adequate flame temperature for complete combustion and prevents rapid quenching of the coalescing or condensing fly ash. The PTC is fired axially upward from the bottom of the combustor, and secondary air is introduced concentrically to the primary air with turbulent mixing. Coal is introduced to the primary air stream via a screw feeder and eductor. The PTC can be equipped with various air pollution control devices (APCD). The PTC can be configured with any of the following APCD: electrostatic precipitator, baghouse, Advanced Hybrid[TM], and spray dryer absorber (SDA) followed by an ESP or baghouse.

The PTC instrumentation permits system temperatures, pressures, flow rates, flue gas constituent concentrations, and APCD operating data to be monitored continuously and recorded on a data logger.

Flue gas samples can be taken at any combination of two of three available system sample points: the furnace exit, the particulate control device inlet, and the particulate control device outlet. After passing through sample conditioners to remove the moisture, the flue

Figure 1. Diagram of PTC
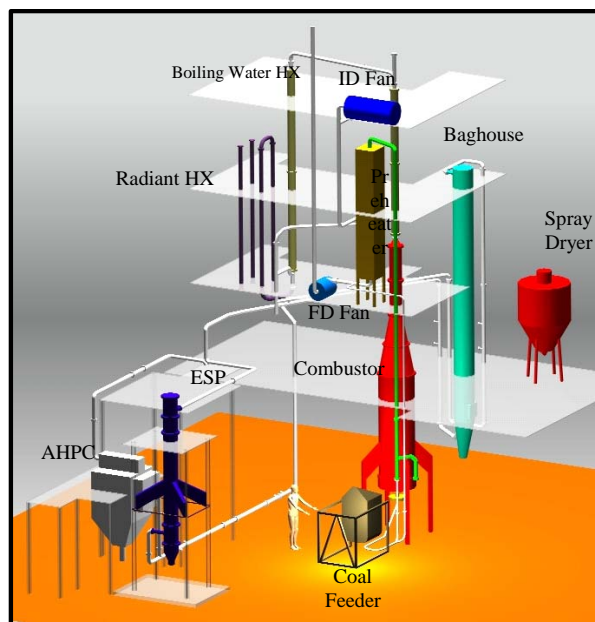
gas is typically analyzed for O_2, CO, CO_2, SO_2, and NO_x. Except for CO and CO_2, each constituent is normally analyzed at both the furnace exit and the outlet of the particulate control device simultaneously, using two analyzers.

For this testing an ESP, consisting of a single-wire, was used. The ESP is designed to provide a specific collection area of 125 ft^2/1000 acfm at 300°F. Since the flue gas flow rate for the PTC is 130 scfm, the gas velocity through the ESP is 5 ft/min. The plate spacing for the unit is 11 in. The ESP has an electrically isolated plate that is grounded through an ammeter, allowing continual monitoring of the actual plate current to ensure consistent operation of the ESP from test to test. The tubular plate is suspended by a load cell which helps to monitor rapping efficiency. In addition, sight ports are located at the top of the ESP to allow for on-line inspection of electrode alignment, sparking, rapping, and dust buildup on the plate. The ESP was designed to facilitate thorough cleaning between tests so that all tests can begin on the same basis.

Continuous emission monitors (CEMs) were used to measure NO_x, NO, SO_2, O_2, CO, and CO_2 simultaneously at the pollution control device inlets and outlets. NO_x was determined using two Thermoelectron chemiluminescent NO_x analyzers. The O_2 and CO_2 analyzers were made by Beckman, and the SO_2 analyzers were manufactured by DuPont. Each of these analyzers was regularly calibrated and maintained to provide accurate flue gas concentration measurements.

Two Tekran continuous mercury monitors (CMM) were used to measure Hg^0 and total gaseous mercury ($Hg[g]$) concentrations simultaneously at the PCD inlet and outlet locations to determine the $Hg(g)$ removal efficiency of various control strategies designed to improve the mercury capture of the pollutant control system. Tekran's sampling system is constructed of Teflon® and quartz glass. The analyzer employs a system of parallel gold amalgamation cartridges that automatically alternate between adsorb and desorb cycles. Cold vapor atomic fluorescence spectroscopy is used for detecting and quantifying Hg^0 concentrations ranging from 0.002 to 2.0 µg/Nm^3. An internal permeation source provided automatic recalibration. The fly ash sampling components of an EPA Method 29 sampling train, a glass nozzle and probe and quartz-fiber filter maintained at the flue gas temperature, were used to obtain particle-free gas samples for CMM analysis. Although CMMs can only directly measure Hg^0 concentrations, the EERC has developed a proprietary flue gas conditioning and conversion system that removes acid gases and transforms Hg^{2+} into Hg^0 so that $Hg(g)$ can be quantified and gaseous Hg^{2+} concentrations can be estimated by difference (i.e., $Hg^{2+} = Hg[g] - Hg^0$). The validity of CMM measurements were evaluated using ASTM Method D6784-02 (Ontario Hydro method).

Results and Discussion

Baseline pilot-scale combustion tests were conducted to establish Hg species concentrations in the resulting flue gases; to determine whether Hg speciation varies across the ESP; and to evaluate the validity of CMM measurement results by comparing to those obtained simultaneously using ASTM Method D6784-02. For example, compared in Figure 2 are CMM and ASTM Method D6784-02 analysis results that were obtained simultaneously during the combustion of the subbituminous coal at the ESP inlet and outlet. Both methods indicate that Hg^0 predominates in the subbituminous coal combustion flue gas and that $Hg(g)$ concentrations at the ESP outlet are similar to those measured at the ESP inlet indicating that the ESP does not effectively capture $Hg(g)$ or transform Hg^0 into other species.
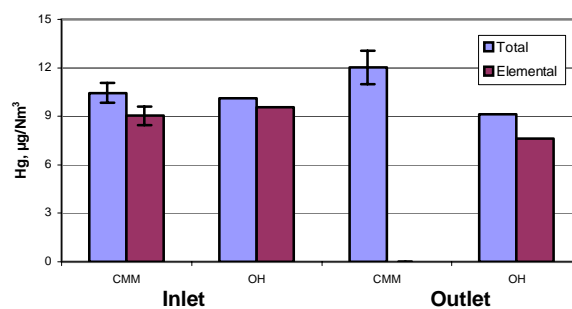

Figure 2. Mercury speciation measurements using CMM and Ontario Hydro methods at ESP inlet and outlet.

The results of mercury removal using injection of DARCO® FGD activated carbon injection upstream of an ESP are shown in Figure 3. Figure 3 compares the mercury removal efficiency obtained in the EERC PTC equipped with an ESP to results obtained at a full-scale pulverized coal fired power plant equipped with an ESP only. These results show that significant quantities of carbon are required to remove mercury from the flue gas. Large amounts of DARCO® FGD were required to effectively remove $Hg(g)$ with an ESP from the flue gas because of mass transfer limits and lack of reactivity between $Hg(g)$ and the entrained DARCO® FGD particles.
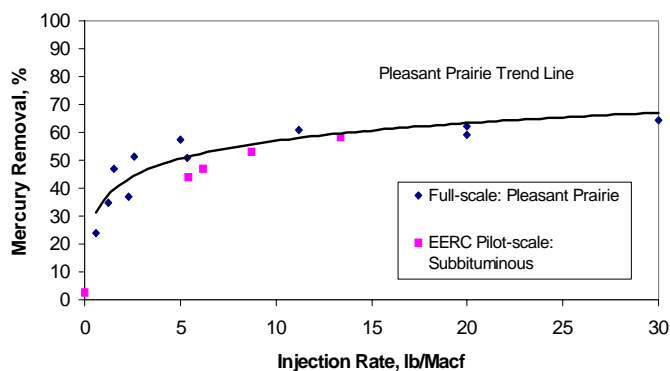

Figure 3. Comparison of full scale and pilot-scale testing results.

SEA1 or calcium chloride ($CaCl_2$) was evaluated as an Hg^0 oxidation and sorbent enhancement additive. During combustion SEA1 will thermally decompose and most of the Cl released will react with water vapor to produce HCl. It is also anticipated that some of the volatilized Cl will recombine with Na and Ca to form NaCl and $CaCl_2$. A very small proportion of the Cl is anticipated to remain in its atomic form, react to form HOCl, or through catalysis reactions with metals to form Cl_2. Theoretically, Cl, HOCl, and Cl_2 are chemically reactive with Hg^0 (1-3). In addition, Cl attached to a catalytic site on fly ash or C (unburned C or injected activated C) surfaces can oxidize Hg^0 and enhance Hg capture (4).

Sorbent and coal additive combinations of DARCO® FGD with SEA1 ($CaCl_2$) were also very effective in promoting ESP $Hg(g)$ capture. The SEA1 additive promoted the formation of $Hg(p)$, thus improving ESP $Hg(g)$ capture as shown in Figure 4.
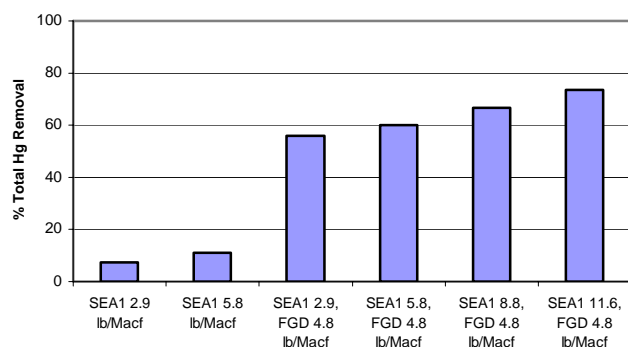
Figure 4. Improved mercury capture using a sorbent enhancement additive with the coal, combined with injection of activated carbon upstream of ESP.

References
1. Sliger, R.N.; Kramlich, J.C.; Marinov, N.M. Towards the Development of a Chemical Kinetic Model for the Homogeneous Oxidation of Mercury by Chlorine Species. *Fuel Processing Technology* **2000**, *65–66*, 423–438.
2. Niksa, S.; Helble, J.J.; Fujiwara, N. Kinetic Modeling of Homogeneous MercuryOxidation: the Importance of NO and H_2O in Predicting Oxidation in Coal-Derived Systems. *Environ. Sci. Technol.* **2001**, *35*, 3701–3706.
3. Edwards, J.R.; Srivastava, R.K.; Kilgroe, J.D. A Study of Gas-Phase Mercury Speciation Using Detailed Chemical Kinetics. *J. Air & Waste Manage. Assoc*. **2001**, *51*, 869–877.
4. Gale, T.K.; Merritt, R.L.; Cushing, K.M.; Offen, G.R. Mercury Speciation as a Function of Flue Gas Chlorine Content and Composition in a 1 MW Semi-Industrial Scale Coal-Fired Facility, Mega Symposium, Washington, D.C., 2003, Paper 28.

EXPERIMENTAL STUDY OF MULTI-POLLUTANT CONTROL DEVICES (SCR, ESP AND FGD) ON MERCURY REMOVAL

Zhongxian Cheng, Yan Cao and Wei-Ping Pan

Institute for Combustion Science and Environmental Technology
Western Kentucky University
1 Big Red Way
Bowling Green, KY 42101

Introduction

Laboratory and full scale testing has shown that a significant amount of mercury (Hg) is potentially captured in existing pollution control devices, but the percent reduction varies greatly from unit to unit due to a large number of variables in the transport and control in coal-fired boiler systems. When considering a single unit with a defined range of process conditions and fuel quality, the Hg chemistry can be experimentally determined and control issues can be adequately addressed. However, these results cannot easily be transferred to other units with dissimilar conditions, resulting in high research costs and long development times. Conditions and gas compositions in a combustion zone and back-pass of a boiler system may influence the form of gaseous elemental (Hg^0) versus oxidized (Hg^{2+}) mercury, that enters the pollution control equipment. However, a quantitative understanding of this chemistry is not available.

To further support a quantitative understanding, work is sought in the areas of 1) developing an understanding of the Hg chemistry in the combustion zone and back-pass of coal-fired boiler systems prior to the gases entering any pollution control equipment, and 2) chemistry and transport with solids/sorbents as Hg passes through pollution control equipment with specific interest in the capture of Hg in Wet Flue Gas Desulfurization (WFGD).

With eventual EPA regulation of Hg emissions from utilities, the pressure will fall on power plant operators to understand the change in Hg chemistry as it gets transported during and post-combustion processes. DOE along with EPA and EPRI as well as other organizations have a significant concerted effort underway with industry to identify economical approaches to control and reduce the amount of Hg emitted from coal-fired power plants. However, fundamentally-based research that increases knowledge regarding Hg chemistry and transport, or addresses technology barriers associated with Hg control, will still be needed. In this research, APCDs consist of three major types of devices – Selective Catalyst Reduction (SCR) for NOx emissions, Electro Static-Precipitator (ESP) for particulate and WFGD for SOx control.

Experiments

Experiments were performed in several power plants and standard Ontario hydro speciation method (OHM) was used to measure mercury concentration at SCR, ESP and FGD facilities.

Results and Discussion

The Impact of SCR on Mercury Chemistry. There are indications that SCR and that Selective Non-catalytic Reduction (SNCR) may oxidize some of the Hg^0 in the flue gas.[1, 2] A limited amount of data is available in the ICR Hg emission database regarding the potential effects of these post-combustion NOx controls on Hg capture. Tests on the single pulverized-coal boiler unit, using a Cold Side-Electrostatic Precipitator (CS-ESP) with SNCR, shows an average Hg capture that is significantly higher than the six units tested with a CS-ESP with no post-combustion NOx controls (91 percent with versus 46 percent without SNCR). A comparison of tests for pulverized-coal boiler units, using a Spray Dryer Absorber (SDA) with a Fabric Filter (FF), shows no discernable difference in Hg capture with or without the use of an SCR for post-combustion NOx control.

Tests on a pilot-scale, pulverized-coal combustor, equipped with a SCR and a CS-ESP, showed increased Hg capture when bituminous coals were burned but not when a subbituminous coal was burned. Hg emission reductions were observed when the SCR system was operated normally, with the injection of ammonia upstream of the SCR catalyst. A study of the effect of SCR technology on Hg illustrated (a) the Hg removal efficiency ranged from 84% - 92% when bituminous coal was burned in the units with SCR and WFGD systems; whereas removals without the SCR ranged from 43% to 51%, and (b) SCR operating at low space velocity resulted in a higher extent of Hg oxidation.[3]

For the past century, the oxidation of HCl to Cl_2 has been known as a catalyzed reaction. A recent paper reported the Deacon reaction is also catalyzed at about 400ºC by iron compounds, which are abundant in eastern and mid-continent coal ashes.[4]

Our recent field studies suggest that the operation of SCRs could affect the occurrence and distribution of Hg species in the coal combustion flue gases. The tests were conducted on seven units include wall-fired and tangential-fired PC boilers, as well as a cyclone coal boiler. Various sulfur (S) and Cl content of the test coal, mostly East bituminous coal, with 0.75 to 3.18% S, and from 246 to 1922 ppm Cl.

Two additional conditions, were also tested on two of the boilers under an operating SCR system with NH_3 off and SCR bypassed, measurement between catalyst layers were also carried out on two test units.

The data indicates the effects of SCR on Hg speciation depend largely upon fuel properties, catalyst type, and flue gas condition at the catalyst zone. Significant discrepancies can also be observed on individual units, burning the same coal under various operating conditions. For example, the unit that fires high sulfur Indiana coal converts Hg^0 to Hg^{2+} by the SCR (with a 2-layer catalyst) under several testing cases. The possible mechanisms for SCR effect we proposed include: (1) Catalytic enhancement of the Hg oxidation by chlorine in the flue gas; (2) Enhancement of the gas phase reactions between Hg and chlorine by changing the flue gas chemistry (e.g. increasing SO_3, decreasing NOx); (3) increasing flue gas residence time for these oxidation reactions, and enhancement of the mixture between solid and gas phases

Thus, further understanding of the roles of Cl and its compounds in the SCR system is needed and a lot of questions are needed to answer, such as, does Cl inhibit or promote the catalytic effect in the system? what is the maximum level of HCl that can be handled in the SCR system? what is the effect of fly ash, other gas species like SO_3, NOx and others on the conversion of mercury species?

The Impact of ESP on Mercury Removal and Vapor Phase Re-emission. By filtering suspended particles from the flue gas, an ESP is highly effective in removing adsorbed Hg especially in systems containing a high LOI, where large numbers of carbon particles capture a significant portion of the Hg present. Theoretically, an ESP would capture more vapor-phase Hg in additional to particular-bound mercury (Hg^P) which was already absorbed by fly ash at the ESP Inlet. However, most experimental cases have shown an opposite trend from to field-testing data that was collected from full-scale utility units. Data from 21 units are represented with ESP efficiency varying from 90% to 99.99%; the activities of fly ash in flue gas varied from low to high, and flue gas temperature varied from 125 ^{o}C to 170 ^{o}C. Thus, there is a need to understand which parameter (or combination of parameters) of an ESP plays the key role on Hg removal through an ESP. Key

questions include what degree does flue gas and ash composition contribute to the vapor-phase mercury remission? Alternatively, does the standard OHM sampling method have inherent bias in the Hg measurement system? Also, are there methods to optimize Hg removal efficiency through an ESP by varying fly ash activity and/or flue gas composition?

The Impact of FGD on Mercury Capture. FGD was first used in the early 1970s. Approximately 15% of coal-fired utility boilers, representing 25% of the power generating capacity, in the United State uses wet FGD systems to control SO_2 emissions now. This technology utilizes a scrubber where flue gas is contacted with the scrubbing liquid in a co- or counter-current flow. In the last decade, it was found that FGD application reduces Hg emission as well. Gaseous compounds of Hg^{2+} are water-soluble and can be absorbed in the aqueous slurry to form mercuric sulfide in the sludge. A DOE-funded study[5] showed that the nominal Hg removal for wet FGD systems on units firing bituminous coals is approximately 55 percent, with the removal of Hg^{2+} between 80 and 95 percent. Studies[6] at a 10-MWe research facility suggested a possible conversion of the Hg^{2+} captured in the scrubbing media and reemissions as Hg^0. An interim report[7] stated that 23 units with wet FGD systems have been tested so far. Twenty-one of the test units burned pulverized coal, while the other two test units burned bituminous coal in cyclone-fired boilers. One unit was equipped with a PM scrubber, and the other had a CS-ESP. The results of emission tests on wet FGD systems indicated that the best levels of total mercury capture were exhibited by units burning bituminous coal and equipped with a FF (98 percent), CS-ESP (75 percent), or HS-ESP (50 percent). The higher capture levels for bituminous-fired boilers equipped with the CS-ESP, HS-ESP, or FF control devices are consistent with the high levels of Hg^0 oxidization associated with these coal-boiler control classes.

Our experiment data suggested that the operating condition of FGDs could affect the Hg removal efficiency as well as Hg^0 re-emission. In most cases, conversion of Hg^0 from Hg^{2+} was observed. The tests were conducted on seven units including configurations of wall-fired and tangential-fired PC boilers as well as a cyclone coal boiler. Various S and Cl contents of the test coal, mostly Eastern bituminous coal, are from 2.5 to 3.5% S, and from 220 to 1000 ppm Cl. Five of these seven units were equipped with an SCR system. Significant Hg^0 re-emission was observed on two scrubbers, including one using liquid chemical as a scrubbing agent. Another was operated under a forced oxidation limestone scrubber condition, a blend of high sulfur Kentucky coal with PRB was burnt. From this figure, it can be observed that with an SCR on-line, there was remarkable impact on Hg^{2+} capture and Hg^0 re-emission through the scrubber. A high conversion rate of Hg^0 to Hg^{2+} was measured while the SCR was by-passed.

Also our measured data indicated that the majority of Hg emitted from the scrubber is Hg^0 when the SCR was off-line, while the major portion of Hg speciation at the FGD exhaust was Hg^{2+} when the SCR was in service. In general, the ratio of Hg^0 to Hg^T increased with an increasing Hg^0 concentration at the FGD Inlet. This may indicate that there was a limitation to capturing Hg^{2+} by slurry due to residence time issues and mass diffusion from the gas phase to the solution, This phenomena will need further investigation.

In accordance with the information mentioned above, improvements in wet scrubber Hg capturing performance depends primarily on the oxidation of Hg^0 to Hg^{2+}, as well as the vapor Hg^{2+} removal speed by the slurry. This may be accomplished by (1) the injection of an appropriate oxidizing agents, (2) the installation of fixed oxidizing catalysts upstream of the scrubber to promote oxidization of Hg^0 to Hg^{2+}, (3) using chemical additives to oxidize Hg^0 to Hg^{2+} in the scrubber or (4) using chemicals to react with vapor Hg^{2+} in the scrubber to form a solid precipitates, eliminating the possibility of re-emitting Hg^{2+} to Hg^0. For the first two approaches, the results of bench-scale research conducted by the EPA showed that the both presence of HCl and NOx in flue gas and iron in fly ash assists in oxidation. Meanwhile, the chloride in the WFGD system will also promote the conversion of Hg^0 to Hg^{2+}.

Thus, there is a need to understand which FGD parameters play a key role on Hg removal through the FGD. Is it pH value, liquid-to-gas ratio, or other chemical concentrations such as chloride, Ca^{2+}, SO_3 etc? To what degree does flue gas composition contribute to the Hg0 remission and Hg removal efficiency? How can the FGD be modified to optimize the Hg removal efficiency by controlling the flue gas composition and scrubber chemistry?

Conclusions

Experimental studies on mercury removal show that multi-pollutant control devices (SCR, ESP and FGD) have potentials to capture mercury. But some critical parameters that affect mercury chemistry and removal efficiency are needed to be identified.

References
(1) Machalek, T., Ramavajjala, M., Richardson, C., Dene, C., Goeckner, B., Anderson, H., and Morris, E., "Pilot Evaluation of Flue Gas Mercury Reactions Across an SCR Unit," Paper # 64, Combined Power Plant Air Pollutant Control Mega Symposium, Washington, May 19-22, **2003.**
(2) Lee, C.W., Srivastava, R. K., Ghorishi, S. B., Hastings, T. W. and Stevens, F. M., "Study of Speciation of Mercury under Simulated SCR NOx Emission Control Conditions," Paper No. 41, Combined Power Plant Air Pollutant Control Mega Symposium, Washington, May 19-22, **2003**.
(3) Chu, P.; Laudal, D.; Brickett, L.; Lee, C.W.; "Power Plant Evaluation of the Effect of SCR Technology on Mercury", Combined Power Plant Air Pollutant Control Mega Symposium, May 19-22, Washington, DC, Paper # 106 **2003**
(4) Gullet, B.K.; Bruce, K. R.; Beach, L.O. Chemosphere, 1945, 20 (10-12), **1990**.
(5) DeVito, M.S., and W.A. Rosenhoover. "Hg flue gas measurements from coal-fired utilities equipped with wet scrubbers." Presented at 92nd Annual Meeting of the Air & Waste Management Association, St. Louis, MO. June 20-24, **1999**.
(6) Redinger, K.E., A. Evans, R. Bailey, and P. Nolan. "Mercury emissions control in FGD systems." Presented at the EPRI/DOE/EPA Combined Air Pollutant Control System, Washington, DC. August 25-29, **1997**.
(7) Kilgroe, J.D., Sedman, C.B., Srivastava, R.K., Ryan, J.V., Lee, C.W., Thornele, S.A., Control of Mercury Emissions from Coal-Fired Electric Utility Boilers: Interim Report", Office of Research and Development, US EPA, EPA-600/R-01-109, December, **2001.**

EVALUATION OF MERCURY BINDING MECHANISMS TO COAL COMBUSTION BYPRODUCTS THROUGH A SEQUENTIAL EXTRACTION PROCESS

James D. Noel, Marina Smallwood, Jessica L. Mohatt, Achariya Suriyawong, Daniel E. Giammar, and Pratim Biswas

Washington University in St. Louis
Environmental Engineering Science Program
One Brookings Drive, Campus Box 1180
St. Louis, MO 63130

Introduction

Mercury is a toxic metal whose emission control was stipulated under Title III of the Clean Air Act Amendments of 1990. On December 14, 2000 the US Environmental Protection Agency announced its intent to regulate emissions. The EPA plans to propose final mercury regulations by December 15, 2004 and require compliance three years later in December 2007.[1] The Clean Air Act Amendments raised new awareness of the potential health effects from stationary sources and stipulated that toxic metal emissions were to be controlled by the use of maximum achievable control technologies (MACT), particularly from combustion systems.[2, 3] Coal-burning utilities account for approximately 30% of total mercury emissions from anthropogenic sources. This percentage is expected to increase incoming years due to the mandated control of mercury emissions from solid and medical waste incinerators.[4] Even though mercury is a trace metal found in coal varying with coal rank in the range of 0.01 to 3.3 ppm_w, its emission (over 2000 tonnes of mercury worldwide) is substantial due to the large quantity of coal burned every year.

Control technologies for removing mercury from the flue gas include scrubbing solutions and sorbent addition to coal or downstream of the combustion zone. Dry sorbents have the potential to remove both elemental and oxidized forms of mercury, and sorbent addition is one of the most promising technologies for reducing mercury emissions.[1, 4] The objective of sorbent injection methods is to effectively capture the toxic metal species of interest, suppress the fraction in the sub-micrometer mode, and preferably transform mercury to an environmentally benign form.[5]

Biswas and co-workers have developed an *in situ*-generated sorbent agglomerate that has been demonstrated to be very effective in the capture of heavy metals. A titanium-based (TiO_2) nano-structured sorbent agglomerate when irradiated with ultraviolet (UV) light has been shown to effectively capture mercury in combustor exhausts.[3] A titanium precursor (titanium tetra-isopropoxide $Ti[OCH(CH_3)_2]_4$) of TiO_2 is introduced directly into a combustion system. The titanium precursor decomposes at high temperatures and is oxidized to form titania particles (TiO_2). Gaseous mercury physically adsorbs to the titania particles; however, this bond is not very strong. The adsorbed mercury is then photocatalytically oxidized on the titania particle surface with ultraviolet (UV) irradiation and binding to the sorbent is enhanced. Since the mercury is now associated with particulate agglomerates, it can be captured with the fly ash using conventional particulate control devices.[6] Fly ash is the major solid by-product of coal combustion (10-50% w/w).[7]

The physical and chemical transformations of mercury during the combustion of coal affect the distribution and speciation of mercury in ash residues. Speciation as well as concentrations of mercury in ashes is important, because speciation determines solubility and toxicity.[8] The mobility, and thus the bioavailability, of heavy metals depends on the characteristics of the particle surface, the strength of bond formed with the surface, and the composition of leaching solution.[9] Sequential extractions can furnish detailed information about the origin, mode of occurrence, bioavailability, physiochemical availability, and mobility of trace metals in solid samples.[10, 11]

In this study, the mercury binding mechanisms of two different fly ashes, without the addition of a sorbent used to capture gaseous mercury, were investigated using a sequential extraction process. The sequential extraction process is evaluated and refined by by applying it to laboratory-synthesized materials with known mercury binding mechanisms. In the future, the mercury binding mechanisms of fly ash from a lab-scale combustor that uses TiO_2 sorbent to capture mercury will be investigated using a sequential extraction process.

Experimental

Materials. The materials to be investigated in this study fall into two categories: 1) fly ash attained from third parties and 2) lab-synthesized materials. Two different types of fly ash were investigated. One came from an Ameren UE full scale power plant. The other came from a pilot-scale coal combustor at the Energy and Environmental Research Center (EERC) in North Dakota.

The sequential extraction process was evaluated by applying the process to two lab-synthesized materials with known mercury binding mechanisms: mercury(II) adsorbed onto goethite and mercury co-precipitated with goethite. Co-precipitation involves the incorporation of mercury within the goethite crystalline lattice. Goethite with adsorbed mercury was prepared according to methods of Kim *et. al.*[12] Goethite co-precipitated with mercury was prepared using a goethite synthesis method developed by Schwertmann *et. al.*[13] in a solution of mercury nitrate. The co-precipitated goethite with mercury will also have mercury adsorbed onto the surface, but the Kim *et. al.* preparation method will not have mercury within the goethite crystalline structure.

Water used in this study was deionized water purified by a Millipore Milli-Q Gradient system (resistivity > 18.2 MΩ-cm). All chemicals used were ACS grade or better. Nitric and hydrochloric acid were Trace Metal Grade.

Sequential Extraction Method. A six-step sequential extraction scheme has been chosen to investigate the binding mechanisms of mercury in fly ash. A summary of the sequential extraction process is found in **Table 1**. A pure water extractant was implemented in the first step for the purpose of removing the most labile trace elements (outer-sphere complexes). A $MgCl_2$ solution was initially chosen for the ion-exchangeable extractant. The ion-exchangeable extractant is designed to mobilize metals adsorbed to the surface via weak electrostatic interactions (also outer-sphere complexes). A solution of 2,3-meso-dimercaptosuccinic acid (DMSA) was chosen as the chelating ligand used to extract surface bound mercury. A weak acid extractant of 0.11 M of acetic acid (pH = 2.8) was used to target mercury that precipitated or co-precipitated with carbonate minerals. Hydroxylamine hydrochloride in nitric acid medium was used as a reducing solution to target mercury bound

Table 1. Sequential Extraction Scheme used in this Study

Operationally-defined phase	Reagent	Operating Conditions
Water Soluble	X ml of Milli-Q Water	4 hr at 20 °C
Exchangeable	X ml of $MgCl_2$ 1 mol/L	4 hr at 20 °C
Surface Bound	X ml of DMSA 0.01 mol/L	4 hr at 20 °C
Acid Soluble	X ml of HOAc 0.11 mol/L	4 hr at 20 °C
Reducible	X ml of NH_2OH-HCl 0.1 mol/L	4 hr at 20 °C
Residual	10 ml of 2:1 HCl:HNO_3 (v/v)	24 hr at 150 °C

Mass of solid = 0.1 g
For extractant to solid ratio of 500 ml/g, X = 50 ml
For extractant to solid ratio of 10 ml/g, X = 1 ml

to iron oxides. The final extraction step consisted of a strong acid at high temperatures and pressures to dissolve the residual material.

Analytical Methods and Techniques. Inductively coupled plasma atomic emission spectroscopy (ICP-AES) and mass spectroscopy (ICP-MS) were used to measure concentrations of metal elements in aqueous solutions, which were then used to calculate the amount of particular metals released from fly ash by each sequential extraction step. The metals investigated consisted of the major elements of fly ash and selected trace elements. The major elements make up most of the crystalline structure of fly ash, while the trace elements only make up a small fraction of the total mass of fly ash.

Combining the sequential extraction processes with other speciation and characterization techniques can confirm or disprove the validity of the sequential extraction process. Characterization techniques including X-ray powder diffraction (XRD), BET-N_2 adsorption for surface area analysis, scanning electron microscopy / energy dispersive spectroscopy (SEM/EDS), transmission electron microscopy (TEM), and Fourier transformed infrared spectroscopy (FTIR) can provide useful information on the matrix mineralogy.[14] These techniques provides a better understanding of the sequential extraction process and confirm indirect speciation measurements from sequential extraction with direct spectroscopic techniques. Fly ash and fly ash subjected to sequential extraction steps have been characterized in this study by XRD, BET, and SEM/EDS.

Results and Discussion

The characterization of fly ash provides a starting point in the evaluation of both the sequential extraction process and the binding mechanisms of mercury. Complete digestions of fly ash from both Ameren's Meramec power plant and EERC's pilot plant were performed to determine the major elemental composition using ICP (**Figure 1**). The compositions are very similar to other coal combustion fly ashes, as the majority of the fly ash consists of silicon, calcium, aluminum, and iron.
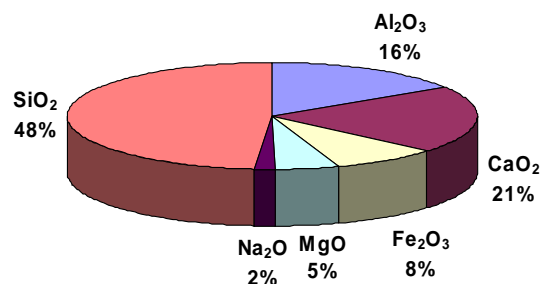

Figure 1. Major element composition of Ameren UE's Meramec Unit 1 Fly Ash.

The surface areas of both Ameren UE's and EERC's fly ashes were measured using BET-N_2 adsorption. The surface area of Ameren UE's fly ash was 2.0 m^2/g and 1.3 m^2/g for EERC's fly ash. Assuming completely spherical mono-disperse particles and a density of 2.65 g/cm^3, both fly ashes were determined to have average particle diameters smaller then 50 μm (7.8 μm and 12.5 μm, for Ameren UE and EERC fly ash respectively). The general particle diameter size was confirmed by SEM imaging, but there is a large range of particle diameter sizes. The particle size of fly ash from the Ameren UE varied more and was not as spherical as EERC's fly ash.

Ameren UE's fly ash (**Figure 2**) had more jagged edges and corners on the surface of the particles than did EERC's fly ash.
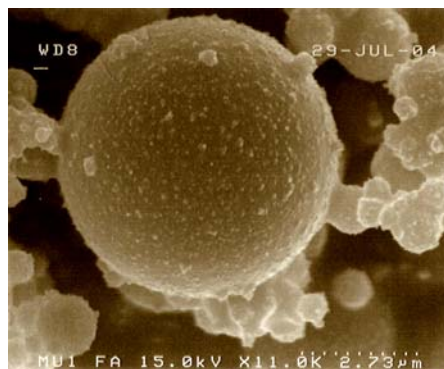

Figure 2. SEM Image of Ameren UE's Meramec Unit 1 Fly Ash

The major element concentrations were measured using ICP after each step in the sequential extraction of Meramec Unit 1 fly ash. Major elements removed during the sequential extraction process are depicted in **Figure 3**. The sequential extraction process shows that major elements are not very labile and that the majority are removed during the final step for residual material. Silicon appears to be the exception to this rule. After the digestive step with concentrated acid, solid still remains, and silicon is assumed to remain in this solid. Iron is the only element removed in the hydroxylamine step, but only 1% of the total amount of iron is extracted in this step. Future work will use a sodium dithionite solution which has more iron-reducing potential. In later sequential extraction experiments the $MgCl_2$ solution was removed from the process for several reasons. First, chloride is an excellent complexing ion for mercury, and $MgCl_2$ may remove mercury by complexation with Cl$^-$ as opposed to ion-exchange with Mg^{2+}. Another reason for the omission of $MgCl_2$ is that it interferes with the measurement of magnesium (a major element of fly ash). Future work will use ammonium nitrate solution for the ion-exchangeable extractant.
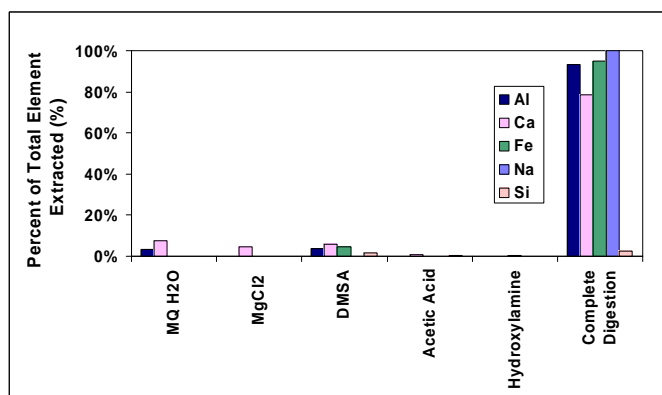

Figure 3. Sequential Extraction Results for Major Elements in Ameren UE's Meramec Unit 1 Fly Ash.

In the sequential extraction of trace elements in Meramec Unit 1 fly ash (**Figure 4**), most of the trace elements were not detectable until the final extraction step. Mercury (Hg) was not detectable in any sequential extraction steps until the final step. Some copper (Cu) and cobalt (Co) are extracted in the weak acid step, but the majorities are recovered in the final step. Chromium is interesting in that measurable amounts were found in the water and the DMSA extracts.

The chromium species found in the water soluble fraction is probably in the +6 oxidation state, since Cr(VI) is much more soluble in water than is Cr(III).
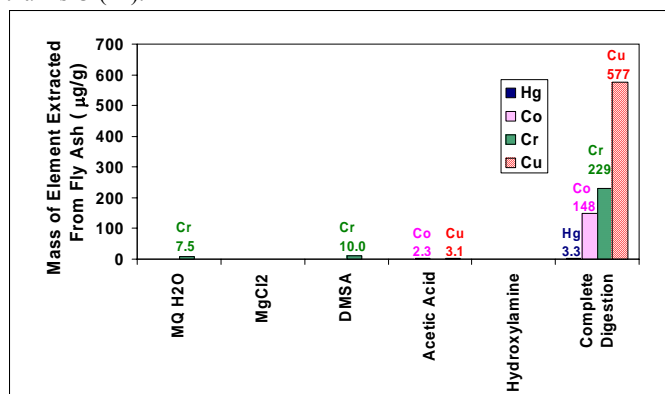

Figure 4. Sequential Extraction Results for Trace Elements in Ameren UE's Meramec Unit 1 fly ash.

The sequential extraction process was applied to lab-synthesized materials: mercury adsorbed onto goethite and mercury co-precipitated with goethite (**Figure 5**). There is a distinction between mercury adsorbed onto goethite and mercury co-precipitated with goethite. Mercury adsorbed onto goethite should have mercury only on the surface of goethite, while mercury co-precipitated with goethite will have mercury both on the surface and within the lattice structure of goethite. Ideally, the sequential extraction of both materials will indicate that the two binding mechanisms are removed in separate steps. Mercury adsorbed onto the surface of goethite was removed in the water soluble step for both materials. The mercury found in the water soluble phase is either from the desorption of mercury from the surface or residual remaining from the preparation of the solid. However, mercury was removed in the reducible phase (hydroxylamine) in only the case with co-precipitated mercury. Therefore, all mercury removed in the water soluble phase is mercury adsorbed onto the surface of the goethite while mercury removed at any other step is found in the inner lattice of goethite.
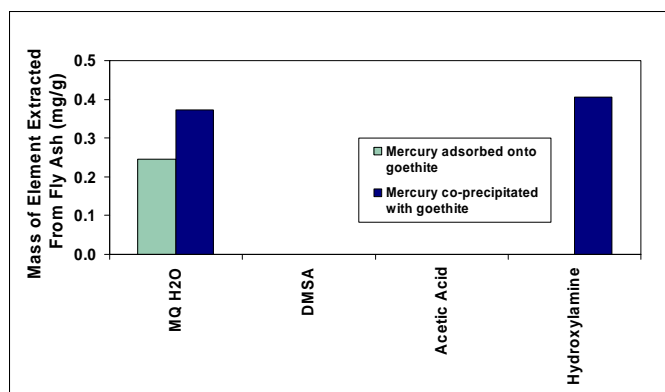

Figure 5. Sequential Extraction Results for Mercury Associated With Goethite.

Conclusions

This sequential extraction provides insight to the phases with which mercury is associated within fly ash. Any mercury captured in a commercial power plant's fly ash was found only in the inner lattice structure. Since no mercury control method was implemented in the combustion process, it is expected that very little mercury would end up in the fly ash. In the future, this sequential extraction

process will be performed on fly ash from a laboratory-scale combustor that utilizes a TiO_2 sorbent to capture gaseous mercury. The sequential extraction process will determine if mercury recovery in fly ash is enhanced by the addition of TiO_2, and will also determine the mobility of mercury captured in fly ash. The sequential extraction process will be modified to include another ion-exchangeable solution without chloride and a stronger reducing extractant to extract more iron oxides. The implementation of CV-ICP-AES (cold vapor inductively coupled plasma atomic emission spectroscopy) will improve mercury detection and be used to analyze samples from the sequential extraction process. Finally, the sequential extraction process itself will be evaluated for effectiveness and selectivity by applying the process to additional materials with known mercury capture or binding methods.

References
(1) Sjostrom, S.; Ebner, T.; Ley, T.; Slye, R.; Richardson, C.; Machalek, T.; Richardson, M.; Chang, R., Assessing sorbents for mercury control in coal-combustion flue gas. *Journal of the Air & Waste Management Association* **2002,** 52, (8), 902-911.
(2) Brown, T. D.; Smith, D. N.; Hargis, R. A.; O'Dowd, W. J., Mercury measurement and its control: What we know, have learned, and need to further investigate. *Journal of the Air & Waste Management Association* **1999,** 49, (6), 628-640.
(3) Rodriguez, S.; Almquist, C.; Lee, T. G.; Furuuchi, M.; Hedrick, E.; Biswas, P., A mechanistic model for mercury capture with in situ-generated titania particles: Role of water vapor. *Journal of the Air & Waste Management Association* **2004,** 54, (2), 149-156.
(4) Granite, E. J.; Pennline, H. W.; Hargis, R. A., Novel sorbents for mercury removal from flue gas. *Industrial & Engineering Chemistry Research* **2000,** 39, (4), 1020-1029.
(5) Biswas, P.; Wu, C. Y., Control of toxic metal emissions from combustors using sorbents: A review. *Journal of the Air & Waste Management Association* **1998,** 48, (2), 113-127.
(6) Wu, C. Y.; Lee, T. G.; Tyree, G.; Arar, E.; Biswas, P., Capture of mercury in combustion systems by in situ-generated titania particles with UV irradiation. *Environmental Engineering Science* **1998,** 15, (2), 137-148.
(7) Zevenbergen, C.; Bradley, J. P.; Van Reeuwijk, L. P.; Shyam, A. K.; Hjelmar, O.; Comans, R. N. J., Clay formation and metal fixation during weathering of coal fly ash. *Environmental Science & Technology* **1999,** 33, (19), 3405-3409.
(8) Wang, J.; Takaya, A.; Tomita, A., Leaching of ashes and chars for examining transformations of trace elements during coal combustion and pyrolysis. *Fuel* **2004,** 83, (6), 651-660.
(9) Filgueiras, A. V.; Lavilla, I.; Bendicho, C., Chemical sequential extraction for metal partitioning in environmental solid samples. *Journal of Environmental Monitoring* **2002,** 4, (6), 823-857.
(10) Tessier, A.; Campbell, P. G. C.; Bisson, M., Sequential Extraction Procedure for the Speciation of Particulate Trace Metals. *Analytical Chemistry* **1979,** 51, (7), 844-851.
(11) Xu, Y. F.; Marcantonio, F., Speciation of strontium in particulates and sediments from the Mississippi River mixing zone. *Geochimica Et Cosmochimica Acta* **2004,** 68, (12), 2649-2657.
(12) Kim, C. S.; Rytuba, J. J.; Brown, G. E., EXAFS study of mercury(II) sorption to Fe- and Al-(hydr)oxides I. Effects of pH. *Journal of Colloid and Interface Science* **2004,** 271, (1), 1-15.
(13) Schwertmann, U.; Cornell, R. M., *Iron oxides in the laboratory : preparation and characterization*. 2nd completely rev. and extended ed.; Wiley-VCH: Weinheim ; New York, 2000; 'Vol.' p xviii, 188.
(14) Kim, C. S.; Bloom, N. S.; Rytuba, J. J.; Brown, G. E., Mercury speciation by X-ray absorption fine structure spectroscopy and sequential chemical extractions: A comparison of speciation methods. *Environmental Science & Technology* **2003,** 37, (22), 5102-5108.

MODELING MERCURY BEHAVIOR IN PRACTICAL COMBUSTION SYSTEMS

Constance Senior, Brooke Sadler, Adel Sarofim

Reaction Engineering International
77 W. 200 S., Suite 210
Salt Lake City, UT 84101 USA

Introduction

Coal-fired power plants are major point sources of mercury discharges into the atmosphere. After considerable study of mercury emissions and their impact on the environment, US EPA made a determination to regulate mercury emissions from coal-fired electric utility boilers. Regulation of mercury emissions may necessitate additional air pollution control devices being installed at utility power plants. Before regulations are imposed, it is important to understand the behavior of mercury in existing devices.

Bench-, pilot-, and full-scale research have lead to the development of theoretical models[1-6] that attempt to explain the speciation and gas-solid partitioning of Hg in coal-combustion flue gases. The primary gas-phase Hg^0 oxidation product is believed to be $HgCl_2$, the specie favored by equilibrium conditions. The gas-phase transformation pathway involves the oxidation of Hg^0 by atomic Cl. The concentration of Cl, in turn, depends on a complex series of gas-phase reactions involving oxygen, water vapor, hydrocarbons, chlorine compounds, and sulfur compounds. A number of critical reactions limit the concentration of Cl and the subsequent conversion of Hg^0 to HgCl and then to $HgCl_2$. The cooling rate in the flue gas has been shown to strongly influence homogeneous oxidation of Hg^0.[4] High flue gas cooling rates between the air heater inlet and air pollution control device inlet limit reaction rates associated with homogeneous oxidation reactions. The effects of cooling rates on heterogeneous reactions are unknown.

Both gaseous Hg^0 and Hg^{2+} have been shown to interact with fly ash[7] and activated carbon sorbents[6] under flue gas conditions. $HgCl_2$ (thought to be the predominant Hg^{2+} species in coal combustion flue gas) adsorbs on fly ash and on activated carbon. Elemental mercury is adsorbed, but can also be oxidized by these solids to form gaseous Hg^{2+}. Acid gases (HCl, SO_2, NO_2) have been shown to affect the adsorption of Hg^0 on activated carbon.

Olson and co-workers have proposed a mechanism for adsorption of both elemental mercury and $HgCl_2$ on carbon sites that takes into account competition for active sites by SO_2 and NO_2.[6] A model that incorporates the proposed mechanism would require the incorporation of adsorption and desorption kinetics for the relevant acid gases as well as for mercury species. To date, the relevant validation data are not available to test a more detailed model. In a "first-generation" heterogeneous speciation mechanism proposed by Niksa,[5] HCl is adsorbed onto the unburned carbon (UBC) in fly ash, forming chlorinated surface active sites that react with Hg^0 to form HgCl, which is assumed to desorbs and subsequently react in the gas to form $HgCl_2$. Adsorbed HCl can also react to form gaseous Cl_2. This model has been validated against pilot-scale coal combustion data.

In this work, a detailed homogeneous model is validated against particle-free, laboratory data on speciation of mercury in combustion exhaust gas. A global heterogeneous oxidation model for carbon in fly ash is developed. The combined homogeneous-heterogeneous model for mercury oxidation is validated against pilot-scale coal combustion data.

Homogeneous Model

Helble and co-workers[2] have studied the post-flame homogeneous reactions of mercury and have developed a detailed chemical kinetic mechanism to describe these reactions. The mechanism includes sub-models for Hg chemistry, Cl chemistry, NO_x chemistry (including NO-Cl) and SO_x chemistry. In this work, we have used this homogeneous mechanism with a chemical kinetics solver that integrates the concentrations of all species in the system along a given time-temperature profile.

The homogeneous model has been validated against two sets of laboratory data.[1,2] Both sets of laboratory data employed natural gas or methane flames to which various other gases were added.

In the work of Sliger et al.,[1] mercury nitrate solution was added to the flame, while HCl was added post-flame at a temperature of 1200 K. The gases were cooled and the concentration of elemental mercury was measured using an on-line analyzer. The HCl concentration was varied and the amount of oxidation of mercury (at the sampling point) was derived from the measured Hg^0 concentration. In **Figure 1**, mercury oxidation is shown as a function of initial HCl concentration; measurements are compared with model results and show good agreement.
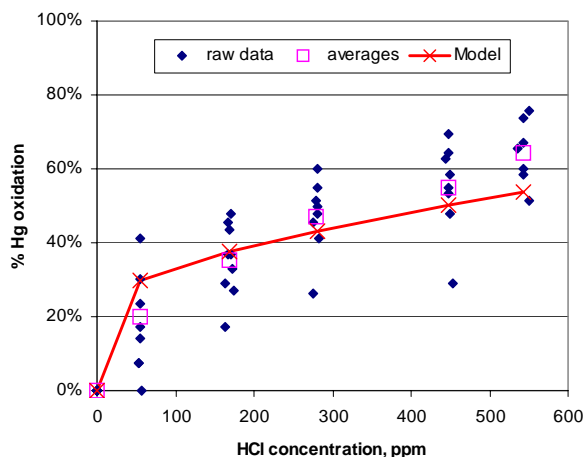

Figure 1. Mercury oxidation as a function of concentration of HCl added postcombustion, comparison of homogeneous model with data.[1]

In the work of Helble and co-workers[2] flue gas was generated from a methane flame. Gaseous mercury was added to a mixing chamber post-flame at 1353 K along with oxidants (Cl_2 or HCl) and other acid gases (SO_2, NO). The gases were then cooled, extracted and fed into a continuous mercury analyzer. **Figure 2** compares the model values of mercury oxidation with the experimentally observed values for injection of Cl_2 or HCl.

The homogeneous model agrees well with laboratory data from two different experimental set-ups, which provides confidence that the homogeneous mercury model can be used for predicting the effects of quench rate and flue gas composition on mercury oxidation.
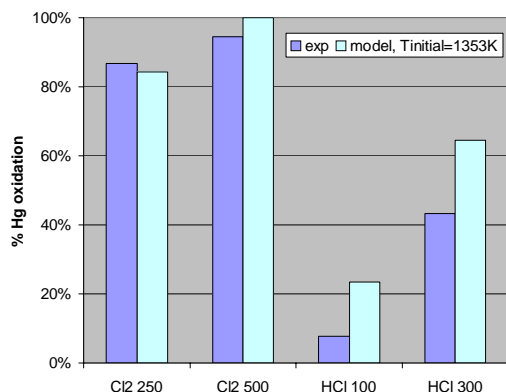
Figure 2. Mercury oxidation as a function of concentration of Cl_2 (250 or 500 ppm) or HCl (100 or 300 ppm) added post-combustion, comparison of model with data.[2]

Heterogeneous Model

The heterogeneous oxidation of mercury could be modeled using a detailed Langmuir-Hinshelwood model that takes into account the observed interaction among mercury and acid gases on carbon surfaces or a global model. Because detailed data on the adsorption of all the pertinent acid gases on carbon surfaces were not available, a global model for mercury oxidation was developed. The global model is based on the following stoichiometric reaction.

$$Hg\ (g) + 2HCl\ (g) + 1/2\ O_2\ (g) \Leftrightarrow HgCl_2\ (g) + H_2O\ (g) \qquad (1)$$
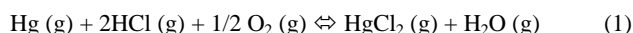
The rate of $HgCl_2$ formation based on these reactions is given in Equation 2.

$$\frac{d[yHgCl_2]}{dt} = k_f \cdot [Hg][HCl] - k_r \cdot \frac{[HgCl_2][H_2O]}{[HCl][O_2]^{1/2}} \qquad (2)$$

The forward and reverse rate constants, k_f and k_r, are related by gas phase equilibrium as described by Equation 3.

$$\frac{k_f}{k_r} = K_c = \frac{[HgCl_2][H_2O]}{[Hg][HCl]^2[O_2]^{1/2}} = K_p \cdot (R \cdot T)^{3/2} \qquad (3)$$

where K_p is given by Equation 4.

$$\log_{10} K_p = \frac{13820}{T} - 8.7235 \qquad (4)$$

For the initial model development, the forward rate constant, k_f, was assumed to be directly proportional to the coal ash content. The forward rate constant was determined by fitting full-scale data from coal-fired power plants,[8] assuming the energy of activation was –19 kJ/mole and adjusting the pre-exponential factor. The full-scale data came from the EPA Information Collection Request (ICR), in which mercury speciation was measured upstream of particulate control devices at a number of coal-fired power plants. Unfortunately, there were no ash analysis data reported in the ICR database. The average ash content for the ICR data used for preliminary model validation was 8.3% and this was used to estimate the pre-exponential factor.

Equation 5 describes the forward rate constant.

$$k_f = 1.75x10^{14} \cdot \frac{\%Ash\_in\_coal}{8.3} \cdot \exp\left(\frac{-E_a}{R \cdot T}\right) \qquad (5)$$

Homogeneous rates for species $HgCl_2$, Hg, HCl, O_2, and H_2O, are augmented by the heterogeneous rate for $HgCl_2$, and the stoichiometric relationship among species. **Figure 3** shows the performance of the combined homogeneous and heterogeneous models for the ICR data. Calculations were done using a Pittsburgh coal with a stoichiometric ratio of 1.23. A typical time-temperature history was assumed for all boilers. **Table 1** shows the coal ultimate analysis.
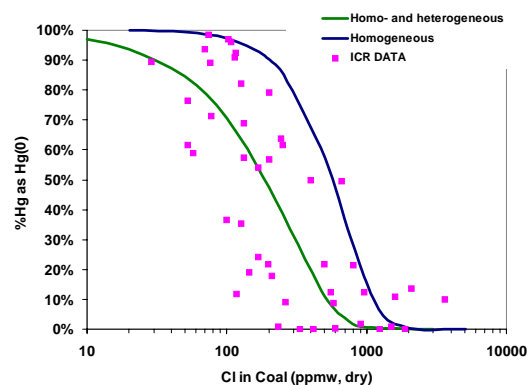

Figure 3. Preliminary homogeneous and heterogeneous mercury modeling results using compared with the fraction of elemental mercury at the inlet to cold-side particulate control devices from ICR data.

The initial heterogeneous model computed heterogeneous mercury oxidation based on the amount of fly ash present. It did not account for variation in the UBC content and fly ash surface area of different ash types. A better approach would account for fly ash surface area per volume of flue gas in the rate constant equation.

The surface area per volume of flue gas is calculated using Equation 6.

$$SA = K(1/T)f_{ash}f_{UBC}M_{ash}S_{rank} \qquad (6)$$

where K is a constant determined by fitting data, f_{ash} is the ash content of the coal, f_{UBC} is the fraction of unburned carbon in the ash, Mash is the ash loading in g ash/Nm^3, 1/T is a temperature correction to convert M_{ash} from Nm^3 to m^3, and S_{rank} is the surface area in m^2 per gram of carbon. The value of S_{rank} varies with the rank of the coal.

Table 1. Pittsburgh Coal Data.

Coal Ultimate Analysis	
(As Received)	
Carbon	76.72%
Hydrogen	4.80%
Oxygen	6.91%
Nitrogen	1.48%
Sulfur	1.64%
Ash	7.01%
Moisture	1.44%
Coal Chlorine (ppmw)	2235
Coal Mercury (ppmw)	0.1

The surface area of fly ash is dominated by that of unburned carbon. Furthermore, the surface area of unburned carbon depends on the coal rank.[9] Based on data in the literature,[9] a carbon surface area of 77 m^2/g of carbon will be assumed for bituminous coals. The global rate will, of course, produce more accurate results if the surface area of the fly ash derived from the

combustion system has been measured.

Therefore, the pre-exponential factor in Eq. (6) is replaced by the following:

$$k_{fo} = C\left(\text{Ash loading, g/m}^3\right) \bullet \left(\text{Surface area, m}^2 / g\right) \quad (7)$$

$$= C'\left[\frac{f_{ash} f_{UBC} M_{ash} S_{Rank}}{T}\right]$$

where $M_{ash} = g / Nm^3$, assuming $f_{ash} = 0.1$

$S_{Rank} = m^2$ per g of carbon

Southern Research Institute (SRI) has published data for mercury speciation in a 1 MW pilot scale coal-fired utility in which two bituminous coals were burned. [10] **Table 2** gives the details of the two coals, Blacksville and Galatia.

Table 2. SRI Coal Ultimate Analysis.[10]

	Blacksville	**Galatia**
C	77.24%	72.94%
H	4.67%	4.58%
O	5.83%	7.80%
N	1.85%	1.68%
S	0.87%	1.31%
Ash	8.05%	6.59%
Moisture	1.49%	5.10%
Cl	0.084%	0.44%
Hg, µg/g	0.078	0.107

The overall temperature profiles for these experiments are plotted in **Figure 4**. These profiles are based on those found in Appendix G of SRI's Biennial Report.[10] The profiles in the Biennial Report began at 1000 °C. A section (taken from SRI's standard temperature profile) was added to the beginning of the profile to model upstream locations in the SRI furnace in order to match the times with the temperatures found in the experimental results in **Table 4**. It is important to note that although the times and temperatures of the profiles match the experimental results, the quench rates do not match those reported in the experimental conditions in **Table 3**. Low quench rates listed in **Table 3** are about

Table 3. Experimental Conditions for SRI Tests.[10]

	run 1	**run 2**	**run 3**	**run 4**	**run 5**
Quench Rate, F/s	922	938	1139	1157	899
Coal	Galatia	Blacksville	Blacksville	Blacksville	Blacksville
%UBC	0.34	0.57	0.35	7.32	7.71
%LOI	1.7	1.9	1.9	9.8	9.8
%FEO	5	5	5	2.5	2.5
%OFA	0	0	0	15	15
SR	1.33	1.33	1.33	1.14	1.14
NO, ppm	620	564	581	218	228

900 °F/s, however, the temperature profiles for these cases have a quench rate of 630 °F/s. Likewise, the high quench rates in **Table 3** are about 1150 °F/s, while the temperature profiles have quench rates of about 750 °F/s.

Table 4. SRI Experimental Results.[10]

	Time, s	T, °F	Hg(0) % at baghouse inlet
run 1	6.4	547	81
	8.18	325	54
run 2	6.7	535	66
	8.27	325	64
run 3	6.75	431	76
	8.4	318	74
run 4	6.98	351	83
	8.6	288	61
run 5	6.8	550	55
	8.3	328	42

Sample locations are indicated in **Figure 4**. The first sample point was located at the end of the quench section. Temperatures at this point ranged from 351 to 550 °F. The second sample point was downstream from the quench section. Experimental and modeling results are shown in **Figure 5**. The experimental data show a higher slope between the two sample points for the high LOI cases, as opposed to the low LOI cases, which demonstrates the effect of unburned carbon on mercury oxidation. The experimental data show an effect of cooling rate; the mercury oxidation decreases when the cooling rate is increased. The modeling shows no change in oxidation when the cooling rate is changed for either low or high LOI cases. For the low LOI cases with Blacksville coal, mercury oxidation is under-predicted. The model results for the rate of oxidation (slope on the plot) between the two points in each case agree with those of the experimental data in **Figures 5**. Better agreement in the absolute value of the mercury speciation might be obtained if the measured surface area of the fly ash were used.
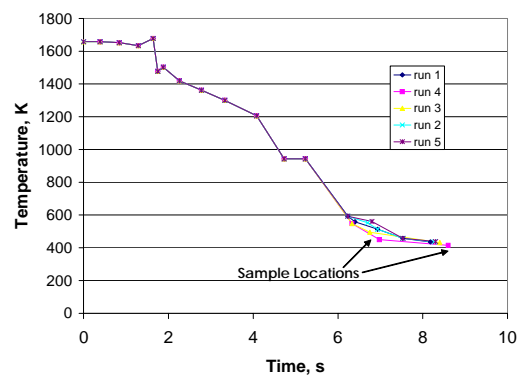

Figure 4. Temperature profiles for SRI mercury experiments.[10]

Conclusions

REI has assembled a model to simulate the gas phase and heterogeneous oxidation of mercury in coal-fired boilers. Only limited data are available for heterogeneous mercury reactions; thus a global model heterogeneous oxidation was created. The homogeneous model agrees well with laboratory data from two different experimental set-ups, which provides confidence that the mercury model can be used for predicting the effects of quench rate

and flue gas composition on mercury oxidation. Model predictions for the rate of oxidation between the two sample points in each case agree with the experimental data. The increase in oxidation in high LOI cases over low LOI cases shows the effect of heterogeneous oxidation from UBC in the ash. More accurate temperature profiles and measured fly ash surface area for the experiments may improve the model results employing the global heterogeneous model. Further refinement of the heterogeneous model is planned, which will incorporate the effects of competition among acid gas species for sites on the carbon surface.

References

(1) Sliger, R.N., Kramlich, J.C., Marinov, N.M. "Development of an Elementary Homogeneous Mercury Oxidation Mechanism." Presented at the 93rd Annual Meeting of Air & Waste Management Association, Salt Lake City, UT, June 18-22, 2000.

(2) Qiu, J., Sterling, R.O., Helble, J.J. "Development of an Improved Model for Determining the Effects of SO_2 on Homogeneous Mercury Oxidation." Presented at the 28th International Technical Conference on Coal Utilization & Fuel Systems, Clearwater, FL, March 10-13, 2003.

(3) Niksa, S., Helble, J.J., Fujiwara, N. "Kinetic Modeling of Homogeneous Mercury Oxidation: the Importance of NO and H_2O in Predicting Oxidation in Coal-derived Systems," *Environmental Science and Technology*, **2001**, *35*, 370.

(4) Senior, C.L., Chen, Z. Sarofim, A.F. "Mercury Oxidation in Coal-Fired Utility Boilers: Validation of Gas-Phase Kinetic Models." Presented at the 95th Annual Meeting of Air & Waste Management Association, Baltimore, MD, June 23-27, 2002.

(5) Niksa, S., Fujiwara, N., Fujita, Y., Tomura, K., Moritomi, H., Tuji, T., Takasu, S. "A Mechanism for Mercury Oxidation in Coal-Derived Exhausts." *Journal of Air & Waste Management Association*, **2002**, *52*, 894.

(6) Olson, E.S., Laumb, J.D., Benson, S.A., Dunham, G.E., Sharma, B.K., Mibeck, B.A., Miller, S.J., Holmes, M.J., Pavlish, J.H. "An Improved Model for Flue Gas-Mercury Interactions on Activated Carbons." In Proceedings of the Mega Symposium and Air & Waste Management Association's Specialty Conference, Washington, DC, May 19-22, 2003.

(7) Dunham, G. E., DeWall, R. A., Senior, C.L. "Fixed-Bed Studies of the Interactions between Mercury and Coal Combustion Fly Ash." *Fuel Processing Technology*, **2003**, *82*, 197-213.

(8) Afonso, R.F., Senior, C.L. "Assessment of Mercury Emissions from Full Scale Power Plants." Presented at the EPRI-EPA-DOE-AWMA Mega Symposium and Mercury Conference, Chicago, IL, August 21-23, 2001.

(9) Küalots, I., Hurt, R. , Suuberg, E. "Size distribution of unburned carbon in coal fly ash and its implications." *Fuel*, **2004**, 83, 223.

(10) Southern Research Institute (SRI), "Understanding Mercury Chemistry in Coal-Fired Boilers," Biennial Report, December 15, 2003.
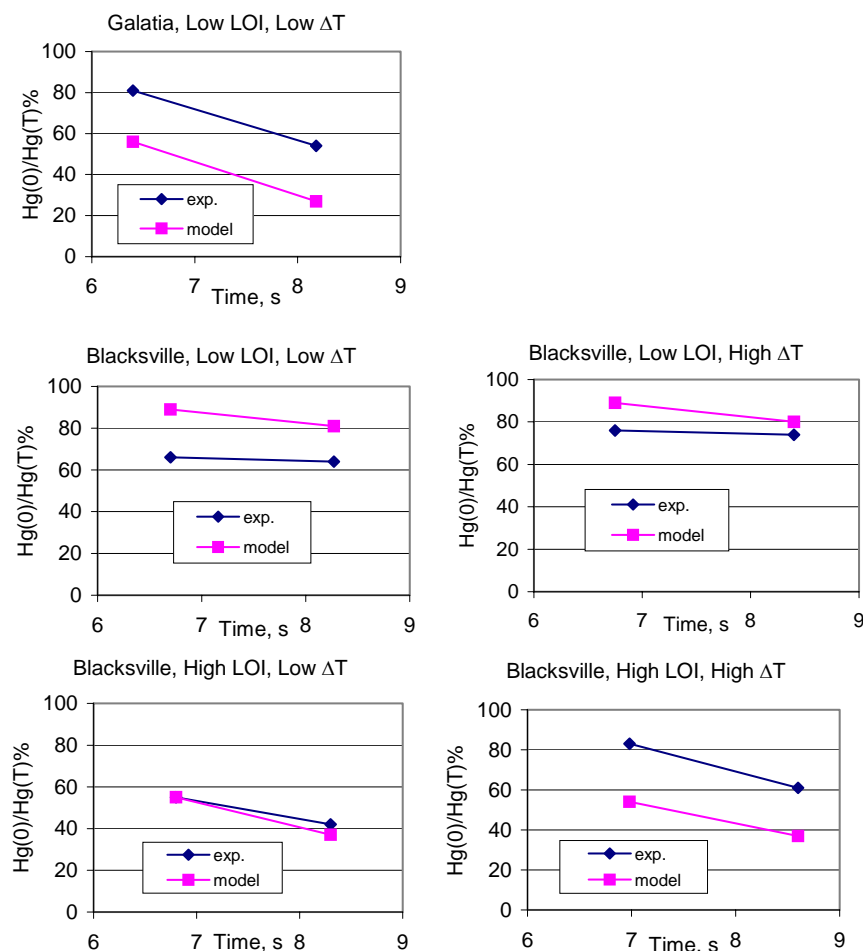
Figure 5. Homogeneous and Heterogeneous modeling results for SRI data with C' = 1×10^{14}.

MODELING SORBENT INJECTION FOR MERCURY REMOVAL IN COAL FIRED POWER PLANTS – ROLE OF SORBENT PARTICLE SIZE DISTRIBUTION AND PRESSURE DROP ACROSS THE BAGHOUSE FILTER

Joseph R.V. Flora[1], Richard A. Hargis[2], William J. O'Dowd[2] and Radisav D. Vidic[3]

[1] Department of Civil and Environmental Engineering, University of South Carolina, Columbia, SC 29208
[2] National Energy Technology Laboratory, U.S. Department of Energy, P.O. Box, 10940, Pittsburgh, PA 15236
[3] Department of Civil and Environmental Engineering, University of Pittsburgh, Pittsburgh, PA 15261

Introduction

Models of mercury removal during activated carbon injection upstream of a baghouse were developed to help in understanding the fundamental process parameters that impact removal efficiency [1-4]. Flora et al developed a two stage model based on pore diffusion [1,2]. The first stage accounted for in-flight mercury removal while the second stage accounted for mercury removal in a growing bed. The key mass balance expressions for the first and second stages can be written as,

$$\frac{dC_b}{dT_d} = -\lambda_2 \frac{dQ_{ave,p}}{dT_d} - \lambda_3 \frac{dC_{ave,p}}{dT_d} \qquad (1)$$

$$\frac{\partial C_b}{\partial \tau} + E \left(\begin{array}{l} \lambda_1 \left(\dfrac{\partial Q_{ave,p}}{\partial \tau} - \dfrac{\eta B_g}{X_0 + B_g \tau} \dfrac{\partial Q_{ave,p}}{\partial \eta} \right) + \\[2ex] \dfrac{\partial C_{ave,p}}{\partial \tau} - \dfrac{\eta B_g}{X_0 + B_g \tau} \dfrac{\partial C_{ave,p}}{\partial \eta} \end{array} \right) =$$
$$\frac{1+\eta B_g}{X_0 + B_g \tau} \frac{\partial C_b}{\partial \eta} + \frac{1}{Pe} \left(\frac{1}{X_0 + B_g \tau} \right)^2 \frac{\partial^2 C_b}{\partial \eta^2} \qquad (2)$$

where C_b is the concentration in the bulk normalized to the influent concentration; T_d is the dimensionless time in the duct; $Q_{ave,p}$ is the average mass of adsorbate per mass of adsorbent normalized to the mass of adsorbate per mass of adsorbent in equilibrium with the influent concentration; $C_{ave,p}$ is the average concentration in the adsorbate pore normalized to the influent concentration; C_b is the concentration in the adsorbate pores normalized to the influent concentration; λ_1, λ_2, and λ_3, are dimensionless parameters; τ is the dimensionless time in the growing bed; E is the composite porosity; η is the dimensionless axial distance along the growing bed; B_g is the dimensionless bed growth rate; X_0 is the initial thickness of the filter; and Pe is the Peclet number.

In their study, the model was applied to a 500-lb/hr pulverized coal-fired pilot-scale combustion system burning Evergreen coal with the injection of Darco FGD activated carbon for mercury control. The isotherm parameters were extracted as a function of temperature. The model showed that removal in the ductwork is minimal, and the additional carbon detention time from the entrapment of the carbon particles in the fabric filter enhances the mercury removal from the gas phase. A sensitivity analysis on the model showed higher C/Hg ratio, lower operating temperature and longer cleaning cycle of the baghouse filter should be utilized to achieve higher mercury removal in this system, and that that mercury removal is dependent on the isotherm parameters, the carbon pore radius and tortuosity, the carbon to mercury ratio, and the carbon particle radius.

Two of the assumptions in the model include a uniform particle size distribution and a constant velocity through the sorbent bed growing on the baghouse filter. However, significant in-duct mercury removal was observed that could not be accounted for by varying the adsorption capacity and transport parameters. Since mercury removal is a strong function of the particle radius, particularly for the short detention times in the duct, the influence of a particle size distribution on the in-duct mercury removal was investigated. Furthermore, in pulse-jet fabric filters, a fraction of the filter is periodically cleaned to relieve the pressure drop across the baghouse. The cleaned section of the filter would have less hydraulic resistance, resulting in a larger fraction of the flow diverted to this section and a dynamic redistribution of the flow as the cake grows on filter bed. The effect of the dynamic re-distribution of flow on mercury removal is investigated.

Model Development

When integrating the role of a discrete particle size distribution for in-duct mercury removal, the same primary equations are applied to each particle in the first stage model. However, a dimensionless time cannot be used because T_d is a function of the radius. Thus, integration is performed in real time. Thus, the mass balances in the particle and in the duct are written as

$$\lambda_1 t_{f,i} \frac{\partial Q_{p,i}}{\partial t} + t_{f,i} \frac{\partial C_{p,i}}{\partial t} = \frac{1}{R^2} \frac{\partial}{\partial R} R^2 \frac{\partial C_{p,i}}{\partial R} \qquad (3)$$

$$\frac{dC_b}{dt} = -\sum_{i=1}^{npsd} \left(\lambda_{2,i} \frac{dQ_{ave,p,i}}{dt} + \lambda_{3,i} \frac{dC_{ave,p,i}}{dt} \right) \qquad (4)$$

where

$$t_{f,i} = \frac{r_{p,i}}{D_p} \qquad (5)$$

and i refers to a particle with radius $r_{p,I}$; R is the radial distance normalized to the particle radius, r_p ; and D_p is the mercury pore diffusion coefficient. Several key radii-dependent dimensionless parameters are defined in terms of each particle size.

To account for the role of a pressure drop in a growing bed, the baghouse was divided into n equal fractions with each fraction of the filter cleaned periodically. Darcy's law was used to describe the pressure drop across the filter, resulting in,

$$Q = \sum_{i=1}^{n} Q_i = \frac{kgh_L}{\nu} \sum_{i=1}^{n} \frac{A_i}{(L_i + kR_f)} \qquad (6)$$

where Q is the gas flow rate; k is the filter bed permeability; g is the acceleration due to gravity; h_L is the headloss across the filter; A is the area of the filter bed; L_i is the depth of the growing bed across the filter; and R_f is the equivalent filter bed resistance of the fabric filter. The rate of growth of the bed is recalculated based on this flow redistribution and is incorporated into the second stage model.

Partial differential equations were converted to ordinary differential equations using orthogonal collation, with the resulting system of equations solved using DDASSL [5]. Parameter estimation was performed by minimizing the sum of the square of the differences between the experimental data and model predictions within a simulated annealing algorithm [6].

Results and Discussion

Using the base case parameters described in [1], the model predicts in-duct removal efficiencies less than 10% for a wide range of operating conditions using a particle radius of 15 μm. However, after upgrades to the pilot system were performed to measure mercury concentrations prior to the baghouse, in-duct removal efficiencies of up to 89% was observed for various conditions for a

system burning a different coal. An in-depth analysis revealed that the particle size distribution of Darco FGD was important. The particle size distribution was characterized using an Elzone particle size analyzer. The value of the volume distribution arithmetic mean radius was 6.5 μm, which is less than the 15 μm originally used in the calculations. Using an average radius of 6.5 μm in the model for a single particle size, the mercury removal efficiency was calculated to be 8.8%. However, when incorporating the entire particle size distribution, the removal efficiency is 40.3%, indicating that the simple use of an average particle size may be inappropriate.
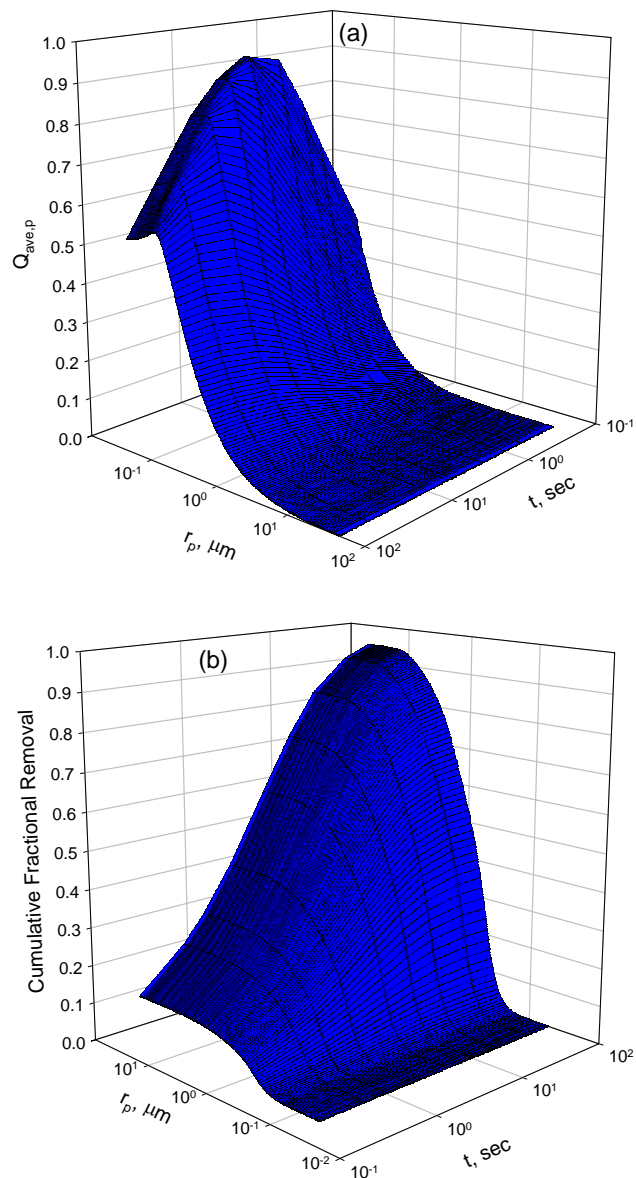
Figure 1. Evolution of (a) adsorbed fraction, (b) cumulative fractional removal, for the base case scenario described in [1] using the Darco FGD particle size distribution

The role of each particle size in the removal of Hg over a period of 100 seconds is shown in Figure 1. Smaller particle sizes remove adsorbate faster and reach high values of $Q_{ave,p}$ (see Figure 1a) at earlier times. As adsorption proceeds, $Q_{ave,p}$ increase for the larger particle sizes and reduces the bulk Hg concentration, resulting in the smaller particles having adsorbed Hg that is in excess of the

equilibrium with the bulk gas and a decrease in $Q_{ave,p}$. Figure 1b shows that the overall removal of Hg increases with time, but with particle sizes ranging from 0.1 to 10.0 μm accounting for most of the removal, as seen by the largest increase slopes. For a detention time of 2 sec, 95 % of the removal is due to particles with a radius less than 5.1 μm, with 62% due to particles less 1 μm.

Figure 2 shows a representative average fit to the pressure drop data for the pilot system burning Evergreen coal. Values of the filter resistance (R_f=6.1×10^8 m^{-1}) and permeability (k=4.4×10^{-13} m^2) were extracted from the pressure drop data. Accounting for the pressure drop results in lower model predictions for the removal efficiency. However, the magnitude of this impact is small compared to the potential impact caused by uncertainties in the isotherm and mass transfer parameters.
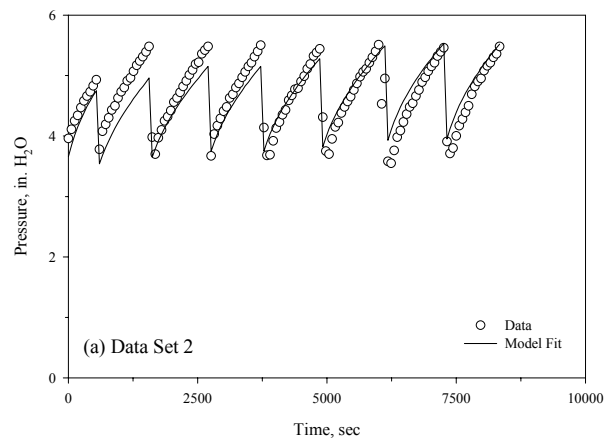

Figure 2. Model fits for the pressure change in a baghouse filter for a representative data set.

Conclusions

The model shows that a single average particle size cannot be used to appropriately model in-duct Hg removal, and generalizations as to the removal mechanisms in the duct should take into account the size distribution of the sorbent particles. The pressure drop impacts flow redistribution across the fabric filter, but does not significantly affect predictions of mercury removal.

References
(1) Flora, J.R.V.; Hargis, R.A.; O'Dowd, W.J.; Pennline, H.W.; Vidic, R.D. *J. Air & Waste Manage. Assoc.*, **2003**, 53, 478-488.
(2) Flora, J.R.V.; Hargis, R.A.; O'Dowd, W.J.; Pennline, H.W.; Vidic, R.D. *J. Air & Waste Manage. Assoc.*, **2003**, 53, 489-496.
(3) Scala, F. *Environmental Science and Technology*, **2001**, 35, 4373-4378.
(4) Serre, S.D.; Silcox, G.D. *Ind. Eng. Chem. Res.*, **2000**, 39, 1723-1730.
(5) Brenan, K.E.; Campbell, S.L.; Petzold, L.R. *Numerical Solution of Initial-Value Problems in Differential-Algebraic Equations*, North-Holland, New York, **1989**.
(6) Goffe, W.L.; Ferrier, G.D.; Rogers, J. *J. of Econometrics*, **1994**, 60(1/2), 65-100.